Title
Structural Characterization, Manipulation, and Properties of Graphene Membranes

Author
Kim, Kwanpyo

Publication Date
2012

Peer reviewed|Thesis/dissertation

Structural Characterization, Manipulation, and Properties of Graphene Membranes

by

Kwanpyo Kim

A dissertation submitted in partial satisfaction of the
requirements for the degree of
Doctor of Philosophy
in
Physics
in the
Grauduate Division
of the
University of California, Berkeley

Committee in charge:

Professor A. Zettl, Chair
Professor John Clarke
Professor Luke P. Lee

Fall 2012

Structural Characterization, Manipulation, and Properties of Graphene Membranes

Abstract

Structural Characterization, Manipulation, and Properties of Graphene Membranes

by

Kwanpyo Kim

Doctor of Philosophy in Physics

University of California, Berkeley

Professor A. Zettl, Chair

Graphene, an ideal two-dimensional membrane, has interesting electronic, optical, mechanical, and thermal properties originating from its unique one-atom-thick honeycomb-lattice structure. Reliable synthesis processes for large-area high-quality graphene have recently been developed, which opens up the capacity for many interesting applications. However, various synthesis-related structural inhomogeneities are still present in large-area graphene and have important implications on graphene's various properties.

Various transmission electron microscopy (TEM) techniques are employed to study suspended graphene membranes at micrometer and atomic scales. Atomic-resolution TEM and electron diffraction analysis are utilized to perform structural investigations of graphene. Notably, various one-dimensional defective structures including grain boundaries and folds in graphene are studied.

On the other hand, the structural manipulation of graphene provides another way to tailor the graphene's properties. Various structural engineering approaches are pursued including fold control, artificial stacking, tearing, Joule heating, and nanomanipulation. The modification of related properties is investigated with electrical measurements, Raman spectroscopy, electron microscopy, and theoretical calculations.

List of Publications

Parts of this work were published in

Kwanpyo Kim, Zonghoon Lee, William Regan, C. Kisielowski, M. F. Crommie, and A. Zettl, Grain Boundary Mapping in Polycrystalline Graphene. *ACS Nano* **5**, 2142-2146 (2011).

Kwanpyo Kim, Zonghoon Lee, Brad D. Malone, Kevin T. Chan, Benjamín Alemán, William Regan, Will Gannett, M. F. Crommie, Marvin L. Cohen, and A. Zettl, Multiply Folded Graphene. *Phys. Rev. B* **83**, 245433 (2011).

Kwanpyo Kim, Vasilii I. Artyukhov, William Regan, Yuanyue Liu, M. F. Crommie, Boris I. Yakobson, and A. Zettl, Ripping Graphene: Preferred Directions. *Nano Lett*. **12**, 293-297 (2012).

Kwanpyo Kim, William Regan, Baisong Geng, Benjamín Alemán, B. M. Kessler, Feng Wang, M. F. Crommie, and A. Zettl, High-Temperature Stability of Suspended Single-Layer Graphene. *Phys. Status Solidi RRL* **4**, 302-304 (2010).

Kwanpyo Kim, Sinisa Coh, Liang Z. Tan, William Regan, Jong Min Yuk, Eric Chatterjee, M. F. Crommie, Marvin L. Cohen, S. G. Louie, and A. Zettl, Raman Spectroscopy Study of Rotated Double-Layer Graphene: Misorientation-Angle Dependence of Electronic Structure. *Phys. Rev. Lett.* **108**, 246103 (2012).

Kwanpyo Kim, Allen Sussman, and A. Zettl, Graphene Nanoribbons Obtained by Electrically Unwrapping Carbon Nanotubes. *ACS Nano* **4**, 1362-1366 (2010).

Contents

List of Figures

Acknowledgment

Many teachers, colleagues, and friends have contributed to the production of this dissertation. First of all, I owe my deepest gratitude to my academic advisor, Professor Alex Zettl, whose encouragement, guidance, and support from the initial to the final research stage enabled me to develop some understanding of the subject. I was very privileged to work in a creative working environment provided by his research group. I also owe much of my gratitude to Prof. John Clarke, who served as a dissertation committee member and the chair of my qualifying exam. Prof. Luke Lee also deserves my deepest gratitude for being a dissertation committee member as well as providing valuable advice and insightful counsel.

I was privileged to have a chance to work with many great collaborators. I would like to thank Prof. Marvin Cohen, Prof. Steven Louie, Prof. Mike Crommie, and Prof. Boris Yakobson for their invaluable guidance. I also had a great pleasure working with Prof. Zonghoon Lee, Dr. Christian Kisielowski, Dr. Sinisa Coh, Liang Tan, Dr. Kevin Chan, Dr. Brad Malone, Dr. Vasilii Artyukhov, Yuanyue Liu, Prof. Sungwoo Nam, and Dr. Inhee Choi. I have learned a lot from all of you.

This dissertation would not be possible without significant contributions from many colleagues and friends. Former Zettl group members, Kenny Jensen, Brian Kessler, Caglar Girit, and Benji Aleman have help me tremendously at the initial stage of my graduate study. Will Regan, Will Gannett, Jong Min Yuk, Jungwon Park, Allen Sussman, Kris Erickson, Nasim Alem, Anna Zaniewski, Maria Schriver, Michael Rousseas, Mehdi Jamei and Jianhao Chen, have provided me valuable assistance. I also wish the new generation of students and postdocs, Aidin, Ashley, Seita, and many more to enjoy their time in Zettl group. Gee Gee and Ann were always available if I need any help from them.

I also would like to express my gratitude to Samsung Scholarship for supporting my graduate study. Fellow Korean physics students and postdocs, Se-Bum Paik, David Cho, Cheol-Hwan Park, Jongwon Cho, Jun Woo Choi, Yoon Pyo Hong, Eunhwa Jeong, YoungWoo Son, HoonKyung Lee, Hae Ja Lee, Sang Ryul Park, Jaeho Sung, Sangkook Choi, Geena Kim, You Kyung Noh, Gil-Young Cho, and Jong-Hwan Kim have also helped me throughout my stay at Berkeley. My former roommate, Taesung Kim, deserves my deepest gratitude.

Last but not least, I would like to thank my family. My parents, Cheol-Ho Kim and Young-Ja Ko were always supportive throughout my life. I also would like to thank my sister and my grandparents. My wife, Jieheerah, has been a continued source of joy throughout my graduate student life. To them I dedicate my dissertation.

Chapter 1
Introduction

In nanoscale materials, the atomic structure has a critical influence on the material's physical properties. When the dimension of a material is reduced to the nano-scale realm, the properties of the material can be significantly modified from those of the bulk counter-part, due to quantum effects and increased surface-to-volume ratio. Moreover, with a reduced system size, the response of material properties due to a structural modification becomes more prominent. Characterization and atomic scale control of the structure of a material are, therefore, of fundamental importance in this respect.

This 'nano' perspective can be well supported by one exemplar material, graphene. Graphene, a one-atom-thick membrane of sp^2-bonded carbon atoms (Figure 1.1), is the building block of graphite, in which graphene layers are stacked together by Van der Waals interaction. Various properties of graphene are quite different from those of its bulk counterpart, graphite. In particular, the exotic electronic properties of this atomic layer have attracted enormous research efforts in academia and industries since 2004 [1].

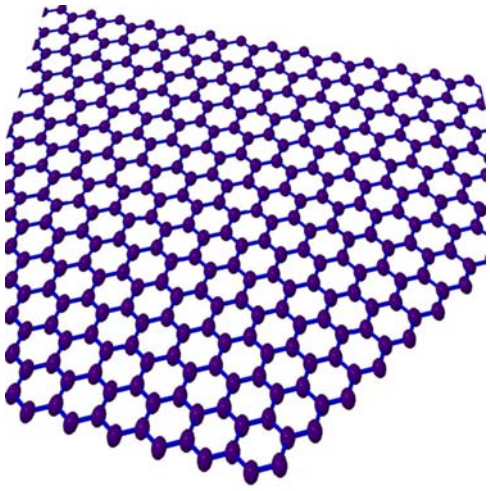

Figure 1.1 The schematic drawing of graphene. The carbon atoms are arranged in the honeycomb structure.

Theoretical study of graphene began over 50 years ago with tight-binding calculations [2]. Even though there had been a couple of experimental isolations of graphene membranes, it was not until 2004 that the isolation of graphene using mechanical exfoliation was achieved. After this material was transferred to a silicon oxide/silicon substrate and experimental demonstration of its field effect electronic properties was published, graphene research

attracted widespread attention and research efforts [1]. In this chapter, I will briefly discuss the various fundamental properties of graphene.

1.1 Electronic properties of graphene

Graphene has unusual electronic bandstructures and associated electronic properties. In the graphene honeycomb lattice, each carbon atom is bonded to its three nearest neighbors by strong sp^2 or σ bonds (Figure 1.1). The low-energy electronic bandstructure of graphene is determined by the remaining p_z orbital (or π bond). One of the most important features is that graphene has a linear dispersion relation around the Fermi energy level, E_F [3, 4]. The graphene is semi-metallic with zero bandgap. In contrast, a typical semiconductor material exhibits a parabolic dispersion relation, in which the charge carriers move with some effective mass under electric and magnetic fields. Due to its linear bandstructure, graphene display a charge transport behavior of massless Dirac fermions. The massless charge transport behavior is also manifested as a half-integer quantum Hall effect (QHE) in graphene [3, 4].

The low-energy electronic behavior of graphene can be effectively described by the Hamiltonian $H = v_F \vec{\sigma} \cdot \vec{p}$, where v_F is the Fermi velocity ($v_F \sim c/300$), $\vec{\sigma}$ are Pauli spin matrices acting on the graphene's sublattice degree of freedom, and $\vec{p} = \hbar \vec{k}$ is the momentum vector measured from the K point with the reduced Plank constant, $\hbar$. The sublattice degree of freedom $\vec{\sigma}$ is also referred to as pseudospin in the literature. In graphene, the backscattering of charge carriers is suppressed due to the pseudospin; the backscattering involves reversing both of the momentum and pseudospin of the charge carrier, which is forbidden for long-wavelength disorder [5]. The suppressed backscattering leads to the high electronic mobility of graphene. Especially, the ultrahigh electron mobility up to ~ 200,000 $cm^2V^{-1}s^{-1}$ has been demonstrated for suspended graphene samples at room temperature [6], which is higher than any other known material.

There are many good review papers on the graphene electronics including A. H. Castro Neto *et al*. [5].

1.2 Optical properties of graphene

Due to its unusual bandstructure, the graphene also has very interesting optical properties. Graphene can strongly interact with light, which enables observation of monolayer graphene under an optical microscope [7]. One of the most interesting features is that the absorption coefficient across the infrared and visible range is nearly constant as πα=2.3 %, where α is the fine-structure constant [8].

Since the Fermi level of graphene can be effectively tuned with electrostatic gating, the optical absorption also can be tuned. The single-layer and AB-stacked bilayer have shown that the infrared absorption can be tuned with electrostatic gating effects [9]. Combined with the electrostatic tuning capability, graphene was demonstrated as a high-frequency optical modulator [10]. A review paper by A. C. Ferrari *et al.* [11] explains well the optical properties of graphene and its potential applications in optoelectronics.

1.3 Mechanical properties of graphene

Graphene is the strongest material ever studied, due to its robust lattice of sp^2-bonding. Using nano-indentation experiments with atomic force microscopy (AFM), researchers have found that single-crystal graphene has an ultrahigh Young's modulus of

around 1 TPa and mechanical strength of more than 100 GPa [12]. Graphene is a promising candidate for strengthening components in composite materials and for other nanomechanical systems applications [13-16]. On the other hand, graphene is easy to bend in the out-of-plane direction. In reality, graphene samples exhibit many different distortions, such as ripples [17] and folds [18]. This aspect is advantageous for applications in flexible transparent electrodes and devices [19].

1.4 Thermal properties of graphene

Graphene's thermal properties are also extraordinary. Suspended graphene has extremely high in-plane thermal conductivity, up to 5000 W/mK at room temperature [20]. This value is around 10 times higher than that of copper. This finding suggests graphene's high potential for use in microelectronics and for thermal management.

Heat conduction in carbon materials is usually dominated by phonons [21]. As the number of graphene layers increases, cross-plane coupling of the low-energy phonons becomes dominant and significantly changes the phonon scattering processes. As a result, graphene's in-plane thermal conductivity decreases and reaches the value of graphite, 2000 W/mK at around four layers [21, 22].

Graphene also has a negative thermal expansion coefficient, measured to be $\sim -6\times10^{-6}$/K [23], which is five to ten times larger than that of graphite. The large negative thermal expansion coefficient is related to out-of-plane phonons and is a direct consequence of the two-dimensionality of graphene. A review paper by A. A. Balandin [21] explains well the thermal properties of graphene and its potential applications including thermal management.

Chapter 2
Synthesis of large-scale monolayer graphene

Most of the earlier studies have employed mechanically exfoliated graphene from graphite for fundamental research of graphene [1]. Exfoliated samples have great structural homogeneity with small defects, which are suitable for the measurement of intrinsic properties of single-crystal graphene samples. Optical microscopy has been utilized to check the layer thickness of graphene flakes after the exfoliation process [7]. However, graphene flakes obtained from the exfoliation process usually have a limited size, less than hundreds of micrometers (Figure 2.1). As a result, exfoliation of graphite is obviously not a scalable process, precluding wide applications of graphene. In this regard, large-area high-quality graphene synthesis has recently become one of the most challenging issues in graphene's research community.

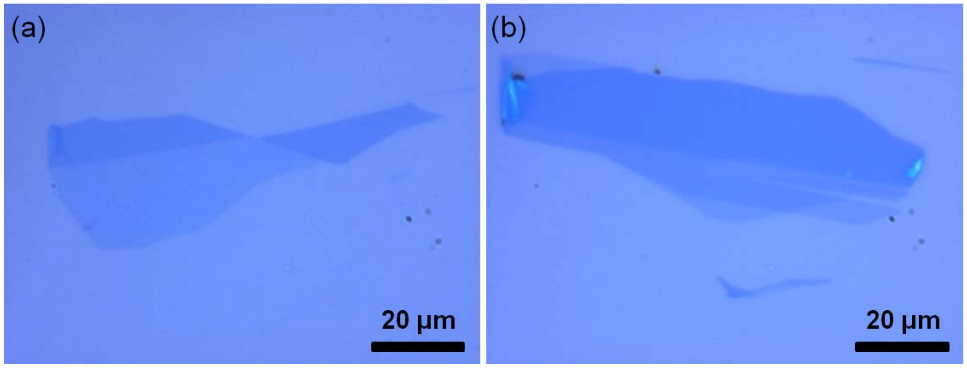

Figure 2.1 Optical images of exfoliated few-layer graphene samples. The micromechanical exfoliation process (Scotch tape method) is utilized for sample fabrication. The exfoliated sample size is usually less than a hundred of micrometers. Contrast in an optical micrograph can be used to distinguish a single-layer region.

In this chapter, I explain available large-scale graphene synthesis techniques, such as chemical vapor deposition (CVD) methods, chemically exfoliated graphene through graphene oxide (GO), and silicon sublimation from silicon carbide substrate. A related fabrication process of suspended graphene samples for transmission electron microscopy (TEM) characterizations and artificially-stacked graphene layers will also be discussed.

2.1. Epitaxial growth of graphene on metal surfaces

2.1.1. Historical background

Chemical vapor deposition (CVD) synthesis of graphene on metal surfaces has

recently emerged as one of the most popular and promising techniques for large-scale graphene synthesis. Large-area graphene can be formed on a catalytic metal surface when the catalytic metal is exposed to high temperatures. One of the related earlier studies goes back to 1968 [24]. When platinum crystal was heated under ultra-high vacuum, the authors observed from Pt surface a ring-like pattern using low energy electron diffraction (LEED) [24]. This ring-pattern was later assigned to thin layers of carbon, graphene-like structure [25]. After these studies, there were numerous observations of epitaxial graphene growth on metal surfaces [26, 27]. Even though these earlier studies have shown that the graphene-like structure can be formed at high-temperature, these studies had limited impact. One thing to note is that these graphene layers were still located on metal substrates and an isolated form of graphene either on an insulating substrate or as suspended was not obtained through a graphene transfer process. There are many recent review articles on the historical account of graphene synthesis, such as D. R. Dreyer *et al*. [28].

2.1.2. CVD on Ni substrate

Nickel has been one of the popular metal substrate for graphene growth [19, 26, 27, 29, 30]. Recently, Q. Yu *et al*. demonstrated that thin graphene-like layers can be synthesized on Ni using methane gas as a carbon source [29]. Utilized synthesis temperatures were around 900 ^{o}C. Carbon dissolved in Ni segregates and precipitates on the Ni surface as the Ni substrate cools down. This was the one of the first studies which demonstrates a graphene transfer process onto an insulator substrate as well as graphene synthesis on metal substrates. This study also demonstrated that the graphene can be high-quality even after the transfer process. Another finding of the study includes that the cooling rate is one of the critical factors for obtaining high-quality graphene. After this study, there were numerous studies on graphene synthesis on Ni [19, 30]. Especially, A. Reina *et al*. [30] and K. S. Kim *et al*. [19] have demonstrated a pattern growth of graphene and its applications for flexible devices.

There are, however, some limitations of CVD growth on Ni. The biggest challenge is to obtain a uniform thickness of the graphene film. Since Ni has high carbon solubility, the graphene synthesized on Ni tends to be multi-layered and the thickness is not uniform on a large scale (tens of micrometers). This is in a strong contrast with graphene synthesized on Cu, which will be discussed in the following section.

2.1.3. CVD on Cu substrate

Among many metal substrates, the most promising catalyst for graphene synthesis is copper. X. Li et *al*. reported the high-quality monolayer graphene synthesis on copper foil in 2009 [31]. They used CH_4 as a carbon source together with H_2 at low pressures (~ 500 mTorr) [31]. The study also showed that the graphene synthesized on Cu can be exclusively monolayer (> 95 % of sample area) [31]. The author successfully demonstrated that synthesized graphene can be transferred to insulating substrates after copper etching and used for field effect transistor fabrications. After these findings, the scale-up versions of graphene synthesis, with roll-to-roll process of 30-in Cu foils, were demonstrated [32, 33]. Later, it was shown that the low carbon solubility in copper is the key factor for monolayer graphene growth [34].

Due to its uniform thickness and high-quality, the graphene synthesis on Cu foils has been utilized by many research groups. Most of graphene samples that I discuss in my

dissertation were also obtained with a similar method. 25 μm thick copper foil (99.8 % Alfa Aesar, Ward Hill, MA) were used and temperature range from 980 ^{o}C to 1040 ^{o}C were investigated for graphene synthesis (Figure 2.2). The high-quality monolayer graphene can be obtained, consistent with the previous study [31]. The graphene synthesis is quite robust to different synthesis conditions (temperature and gas concentrations).

After the graphene synthesis, optical microscopy and scanning electron microscopy (SEM) can be utilized to check graphene. Figure 2.3 shows the optical images and SEM micrographs of graphene on copper foil with sub-monolayer coverage. With 2 minute graphene synthesis, ~ 70 % of copper foil was covered with graphene. From these images, we can also estimate the density of graphene nucleation, which is a critical factor for the control of graphene grain size.

With a longer growth time, continuous graphene films can be obtained. Usually, 15 ~ 20 minute growth was used for graphene synthesis. The copper surface appears to be bright brown after graphene covering under the optical microscope (Fig. 2.4a-b). SEM images clearly show that the average grain size of copper is around hundred micrometers with high-temperature annealing treatment (Figure 2.4c and 2.4d).

While most of CVD graphene synthesis methods utilized methane as a carbon source, there are also various demonstrations of CVD graphene growth on copper from other carbon sources. Notably, Z. Sun *et al*. has reported the high-quality graphene synthesized from poly methyl-methacrylate (PMMA) coated copper foil without any other carbon sources [35]. Recently, the better control of CVD graphene such as grain size, uniform thickness for bi-layer and triple-layer growth, and stacking relation is currently under investigation.

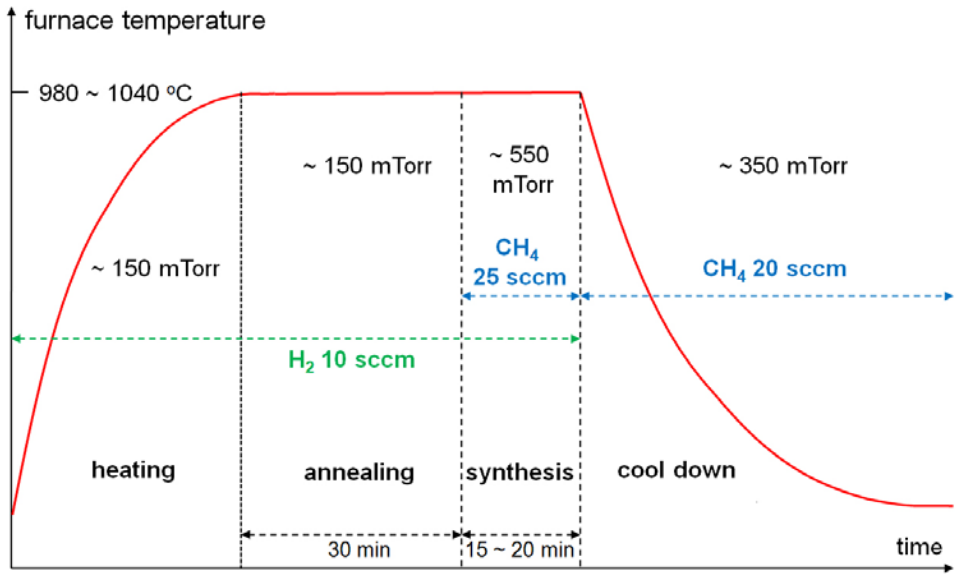

Figure 2.2 Graphene CVD synthesis process. Hydrogen and methane are used for the graphene growth. 30 minute annealing is utilized before the graphene synthesis to increase the crystallinity of copper foil.

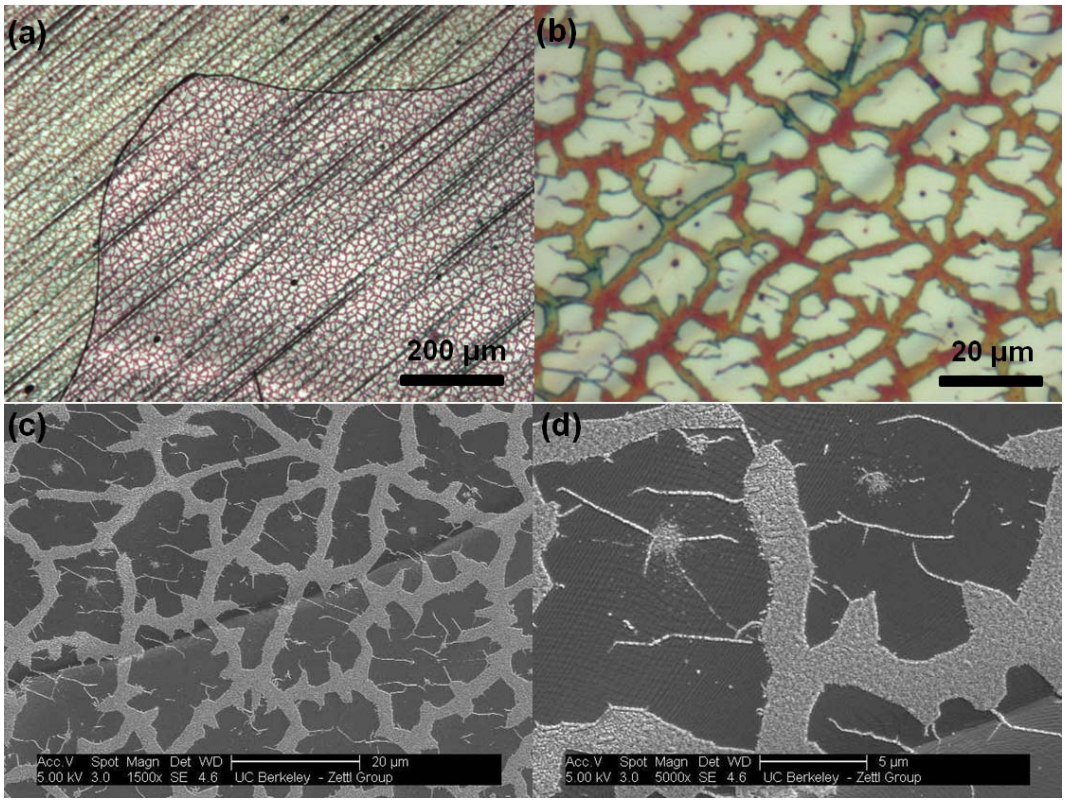

Figure 2.3 Sub-monolayer growth of CVD graphene on Cu foil. The sub-monolayer graphene was synthesized by 2 minute CVD growth. (a-b) Optical images of CVD graphene. Bright regions are covered with graphene. After the growth, the sample was heated at 200 ^{o}C in air for 30 minutes for an easy visualization of graphene-grown regions. (c-d) SEM images of Cu foil partially covered by graphene.

2.1.4. CVD on other metal substrates

Other metals utilized for graphene synthesis includes Ru [36], Pt [37], and Ir [38]. Even though high quality graphene samples can be obtained on these substrate, the transfer and isolation procedures are somewhat problematic due to strong interaction between these metals and graphene or difficulty of etching metal substrates. These substrates are more expensive compared to copper foil, which hinders their wide usage in graphene synthesis.

2.2 Graphene synthesis on SiC substrates

Single-crystal SiC substrate can be used for epitaxial growth of graphene [39, 40]. At elevated temperatures, Si starts to evaporate from the surface, leaving carbon atoms behind. These carbon atoms can be crystallized into high-quality graphene. Graphene obtained on SiC has different thicknesses depending on the C- or Si-terminated SiC surfaces. Generally, the graphene films are multi-layered and it is quite difficult to obtain monolayer graphene.

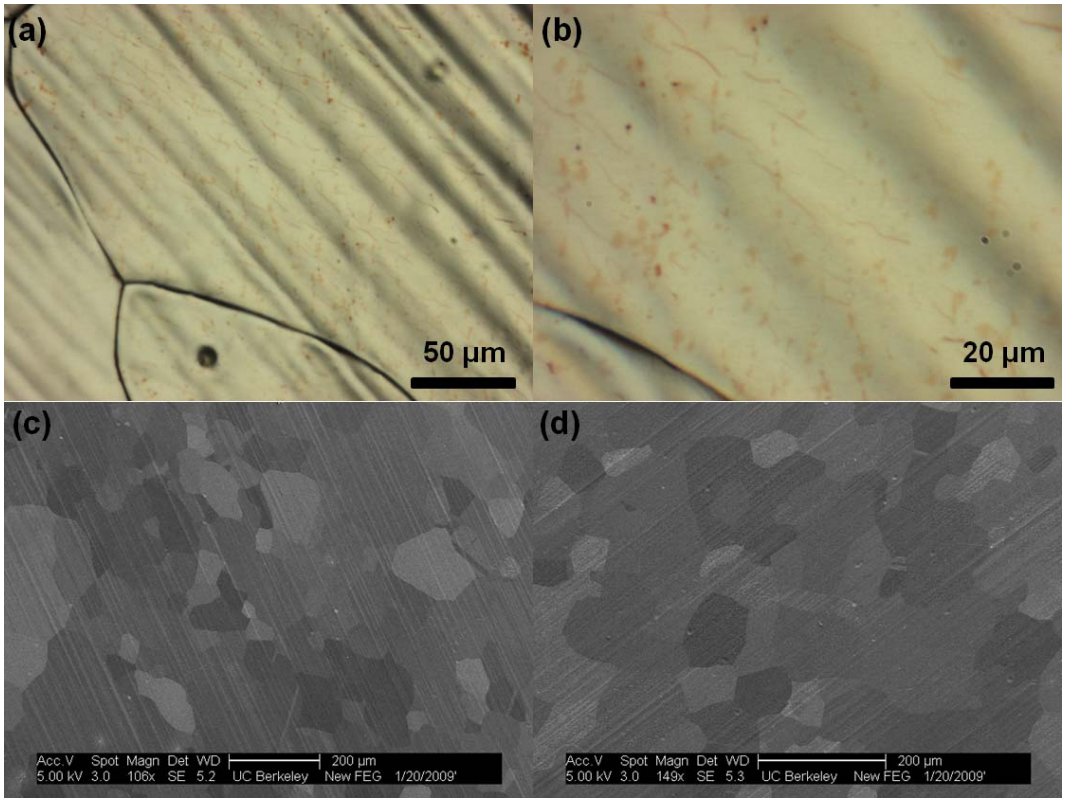

Figure 2.4 CVD graphene on Cu foil. (a-b) Optical images of CVD graphene on Cu foil. (c-d) SEM images of CVD graphene on Cu foil. The different contrast originates from different copper grains.

2.3 Graphene from graphene oxide (GO)

Graphene can also be obtained through graphene oxide (GO). Graphite can be oxidized in the presence of strong acids and oxidants [41]. GO sheets are hydrophilic and can be effectively dispersed in liquid and exfoliated by sonication. Even though the oxidation process aids the exfoliation of graphite in large quantities, the properties of exfoliated GO is very different from pristine graphene. There were many studies to reduce GO to obtain a better quality of graphene from GO. However, the reducing process cannot restore GO into pristine graphene and the quality of reduced GO (rGO) still does not reach that of graphene synthesized from CVD process [42].

2.4 Transfer of graphene into other substrates and fabrication of suspended graphene membrane

After the CVD synthesis, the graphene is located on metallic substrates. It is desirable to obtain graphene either on an insulating substrate or as suspended for the studies of graphene's intrinsic properties. In this section, I will briefly discuss the graphene transfer process and fabrication of suspended graphene samples for transmission electron microscopy (TEM) investigation.

Most available graphene transfer processes involve wet etching of copper foil [19, 30, 31]. Many different copper etchants can be used, such as iron chloride ($FeCl_3$) and sodium

persulfate. The Zettl lab usually uses $Na_2S_2O_8$ with the concentration of 0.1 g/mL for copper etching. $(NH_4)_2S_2O_8$ is also available as a copper etchant. Iron chloride ($FeCl_3$) was initially used for copper etchant but this leaves a higher coverage of residues, such as nanoparticles, on the graphene surface.

A mechanical support for graphene is necessary during the copper etching. PMMA is a popular support for graphene transfer [19, 30, 31]. Generally, PMMA is spincoated on graphene and cured at ~ 185 ^{o}C for 30 minutes. After copper etching, freestanding PMMA-coated graphene can be isolated and transferred onto any target substrates. PMMA is removed in an acetone bath. Figure 2.5 shows optical images of graphene transferred to a silicon oxide/silicon substrate with this method.

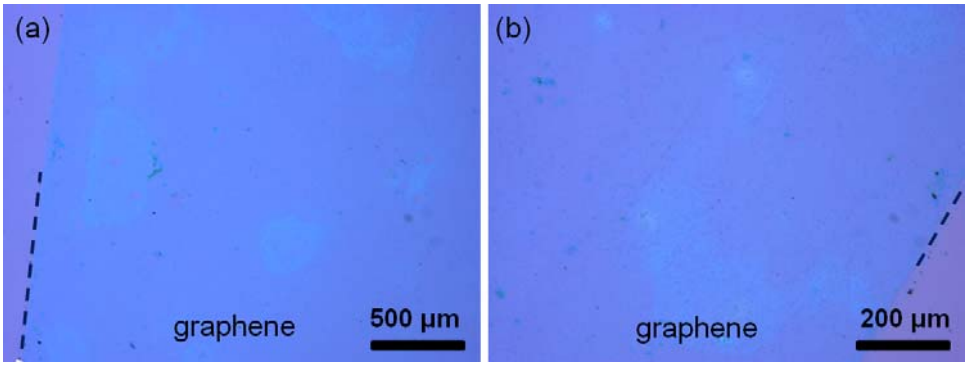

Figure 2.5 Optical images of CVD graphene transferred to SiO_2/Si substrate. The large-area graphene can be transferred to any arbitrary substrate. (a) The graphene appears to be bright blue under the optical microscope. The edge of the transferred graphene film is shown as a dashed line at the left side of the image. Graphene was transferred with PMMA method. (b) Another image of transferred graphene. The edge of the transferred graphene film is shown at the right-bottom side.

Even though the PMMA-utilized transfer method is quite useful, there are some limitations. Most notably, polymer residues from PMMA cannot be fully removed from graphene surface. The polymer residues can have significant implications for graphene's various properties including electronic and mechanical properties. Especially, for an atomic scale study of graphene, obtaining clean graphene surface is essential. A hydrogen annealing process has been utilized to clean the graphene surface [43].

The fabrication of suspended graphene membrane is required for TEM investigation. The above PMMA transfer method can be utilized for TEM sample fabrication. The desirable transfer method would not involve the usage of PMMA to have a clean graphene surface. In the Zettl lab, a clean direct graphene transfer method was developed [44]. Figure 2.6 shows the schematic process for graphene transfer. After the CVD synthesis on Cu foil, we etch the bottom graphene by reactive ion etching with oxygen. We place a commercial Quantifoil TEM grid on graphene and drop a small droplet of isopropyl alcohol. Quantifoil TEM grids can be purchased from many vendors such as SPI Supplies (http://www.2spi.com/catalog/). Different types of Quantifoil TEM grids with 1.2 μm, 2 μm, and 7 μm holes are available. The drying process of isopropyl alcohol gives a good adhesion between graphene and a carbon film in TEM grid. After the adhesion, we gently put the sample in a copper etchant.

While etching the copper foil, TEM grids float on the etchant surface. Finally, a TEM grid sample is transferred to a water bath, recovered with a glass slide, and naturally dried.

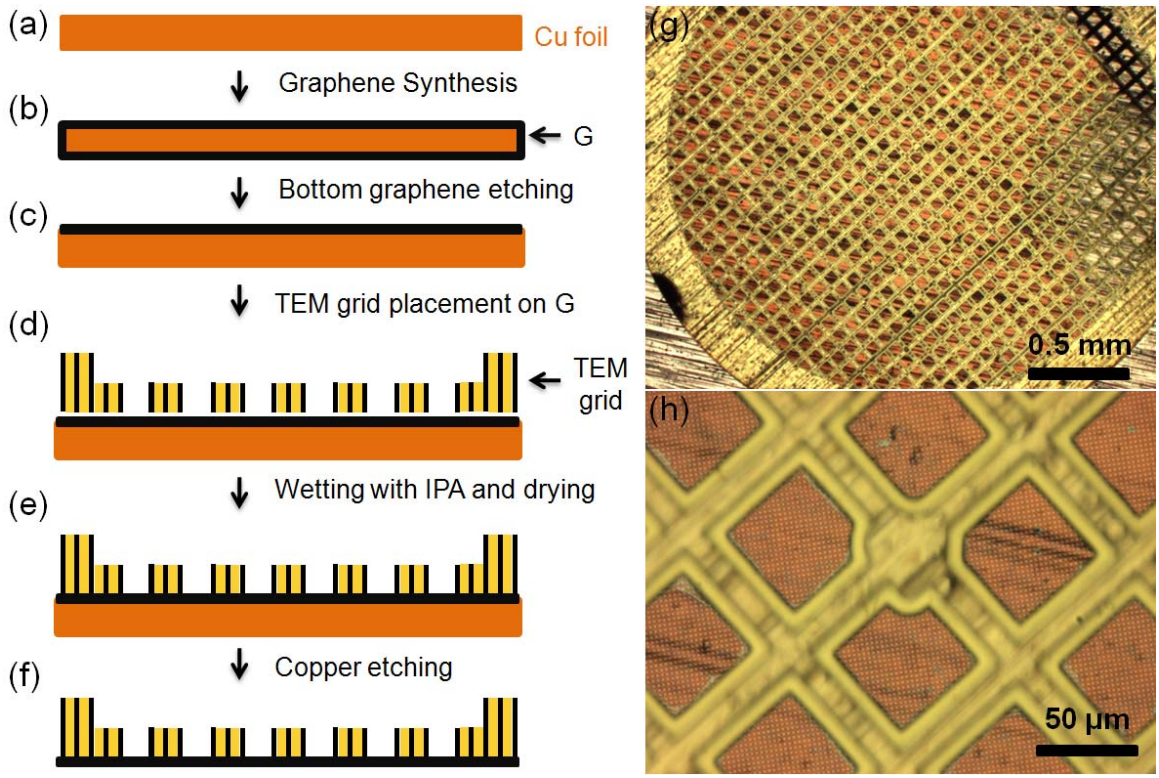

Figure 2.6 Preparation of graphene TEM grid. (a) On copper foil, (b) we perform chemical vapor deposition growth of graphene. (c) We etch the bottom graphene with reactive ion etching. (d) We place a commercial Quantifoil TEM grid on graphene. (e) Wetting and drying of isopropyl alcohol gives a good adhesion between graphene and grid. (f) We etch out the underlying copper. (g) Optical image of a holey carbon TEM grid on copper foil after the adhesion process. (f) Zoomed-in optical image of a TEM grid on graphene on Cu foil. (g) Optical image of TEM grid sitting on graphene on copper foil. The image is corresponding to the process step e. (h) Zoom-in optical image around the central region of the TEM grid.

SEM can be utilized to quickly check the coverage of graphene on Quantifoil TEM grids. Even though there are some limitations for checking the quality of graphene due to its limited spatial resolution, SEM clearly shows the contrast for suspended graphene membrane. Figures 2.7a-d show SEM images of Quantifoil TEM grid where CVD graphene is transferred onto with the transfer process as described above. The torn area in graphene appears as dark in SEM images. For a Quantifoil TEM grid with circular holes with 1.2 µm diameter, the direct transfer method can yield a perfect suspended graphene with up to ~ 90 %. For 2 µm holes, the yield can be up to ~ 80 % and the usual graphene yield with square holes of 7 µm goes down to 20 %.

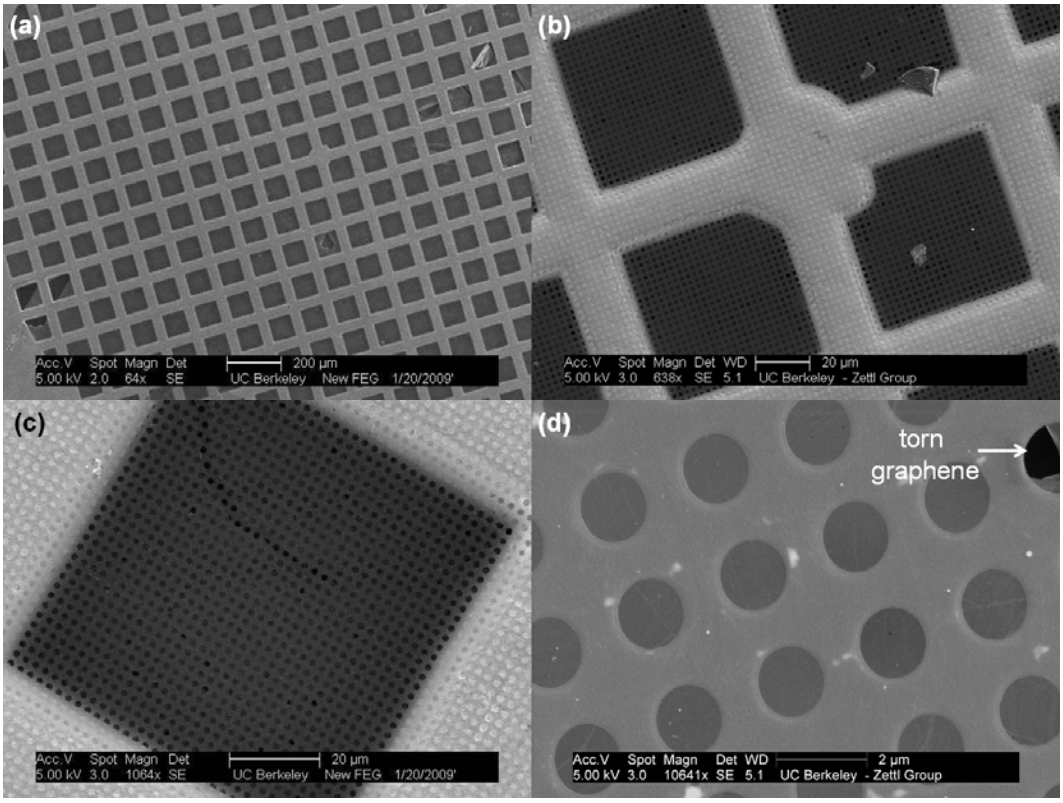

Figure 2.7 SEM images of graphene transferred to a Quantifoil holey-carbon TEM grid. (a) Overview SEM image of a holey carbon TEM grid. (b) Zoomed-in SEM micrograph of a TEM grid. The carbon film has an array of holes. (c) SEM image. Torn graphene area is shown in dark line. (d) Zoom-in SEM micrograph showing suspended graphene over an array of holes with 1.2 µm diameter. Right side of the image shows the region with torn graphene.

2.5 Artificial stacking for fabrication of multi-layer graphene and graphene sandwich structures

Using a monolayer graphene as the building block, we can fabricate *n*-layer graphene by sequential stacking. This process allows us to precisely control the thickness and study thickness-dependent properties of graphene [32, 45]. It also opens up interesting applications of graphene such as transparent conducting electrodes [32], as the monolayer graphene usually does not produce high enough conductivity. This sequential stacking process can also be utilized to obtain randomly rotated double-layer graphene [46]. The rotational-angle-dependent electronic and related other properties will be discussed later in Chapter 8.

Prior to the transfer of each new graphene layer, the external species of materials can be deposited between graphene layers, to obtain graphene veil and sandwich structures [45]. External species can tune graphene's electronic, chemical, and mechanical properties [45]. Another interesting aspect is the capturing of liquid-phase samples between graphene layers [45, 47]. Figure 2.8 briefly explains the process of graphene liquid cell fabrication. Using the graphene liquid cell, the first-time atomic resolution monitoring of nanoparticle nucleation and dynamics has been demonstrated [47].

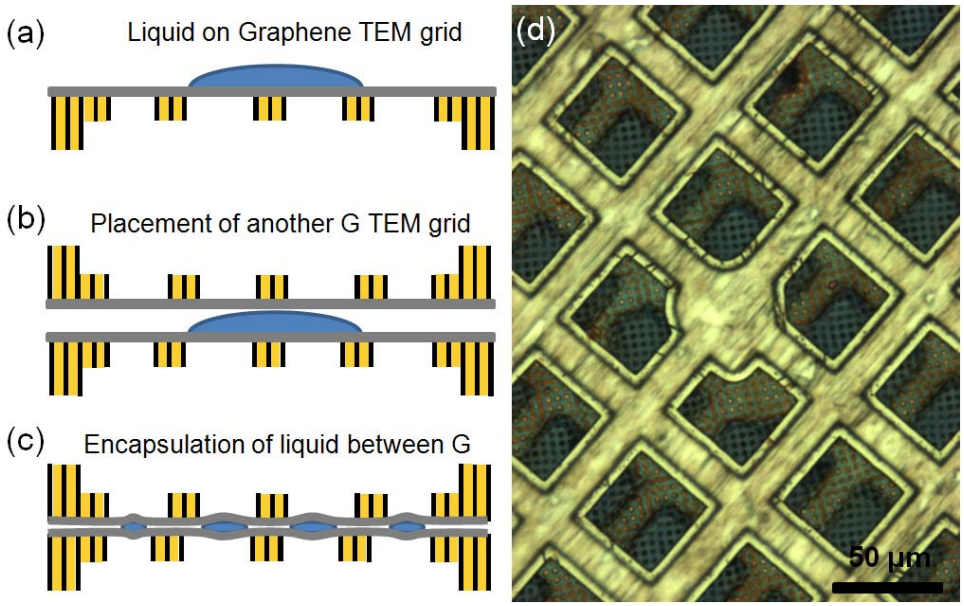

Figure 2.8 Schematic of double-layer graphene preparation. (a) We place small droplet of liquid on graphene TEM grid. (b) We cover liquid with another graphene TEM grid. (c) The liquid is squashed down and makes sub-micrometer-sized droplets of liquid encapsulated between graphene layers. (d) Optical image of a two-overlapped graphene sample.

Chapter 3
Transmission electron microscopy: Atomic-scale characterizations

3.1 Introduction to transmission electron microscopy (TEM)

Transmission electron microscopy (TEM) is a valuable tool for micro and atomic structural characterizations of various materials. Electron microscopes enable us to observe objects which are not accessible by conventional optical microscopes. The resolution of optical microscopes is limited by the wavelength of the visible light, ~ 400 nm. Instead of optical light, a TEM utilizes high-energy electrons for imaging and spectroscopic measurements. Incident high-energy electrons, usually around 100 keV, interact with a given specimen and undergo elastic and inelastic scatterings. Since high-energy electrons of 100 keV have very small wavelengths (< 0.1 Å), the spatial resolution of TEMs is dramatically improved compared to optical microscopes. Forward-scattered or transmitted electrons go through a series of electromagnetic lenses and are captured with imaging acquisition systems, such as a charge-coupled device (CCD).

Since transmitted electrons are utilized for imaging and spectroscopy, samples are required to be electron-transparent at certain degrees. For many metal and semiconductor materials, the thickness of a sample should be less than ~ 100 nm. Nano-scale materials, including carbon nanotubes and graphene, readily have proper thickness for TEM investigations.

As the energy of the imaging electrons increases, one expects to obtain better spatial resolutions due to electron's smaller wavelengths. At higher imaging voltages, however, the e-beam-associated damage also increases. This becomes especially problematic, for low-Z materials, including graphene and carbon nanotubes. Therefore, the low acceleration voltages (< 100 kV) are desirable since this can minimize knock-on damages to a specimen. A conventional TEM, without an aberration corrector, has a resolution of ~ 2.5 Å operated at 100 kV. Many good textbooks are available for general introduction to TEM [48, 49].

In this chapter, I will describe the basic principles and capabilities of TEM. This includes high resolution TEM imaging, diffraction acquisition, and bright-field and dark-field imaging. The recent development of spherical-aberration corrected TEM is an exciting advancement for TEM and scanning TEM (STEM) [50, 51]. I will also discuss the spherical-aberration-corrected TEM, especially image-corrected TEM, and its application for graphene research in this chapter.

Various TEMs have been utilized for my study, which include JEOL 2010 at Zettl research lab, Libra 200MC and TEAM 0.5 microscopes at National Center for Electron Microscopy. Regular high-resolution TEM imaging has been performed with JEOL 2010. Diffraction acquisitions have been performed in JEOL 2010 and Libra 200MC microscopes. Scanning TEM and nano-beam diffraction acquisition have been performed in Libra 200. Finally, atomic resolution imaging has been performed in TEAM 0.5 microscope. JEOL 2010

was mainly operated at 100 kV. Libra 200 and TEAM 0.5 were mostly operated at 200 and 80 kV, respectively.

3.2.1 TEM components and basic principles

Figure 3.1 describes a schematic of basic TEM components and an electron ray diagram for real-space imaging mode. Throughout this chapter, I will only describe the basic aspects of TEM since a more detailed discussion is available in many textbooks [48, 49].

A reliable source of electrons is required for TEM. A lanthanum hexaboride (LaB_6) crystal is used for an electron source in JEOL 2010 at Zettl lab while a field emission gun is used for Libra 200MC and TEAM 0.5 microscopes. Field-emission sources provide a more monochromatic electron beam, which is suitable for high-resolution imaging and spectroscopy. In the TEM imaging mode, the broad beam of electrons is illuminated on a specimen as shown in Fig. 3.1. The electron beam interacts with a specimen and only the forward-scattered electron beam undergoes the TEM lens system. The red and green lines represent the electron beam scattered with reciprocal lattice vectors $\vec{g}$ and $-\vec{g}$.

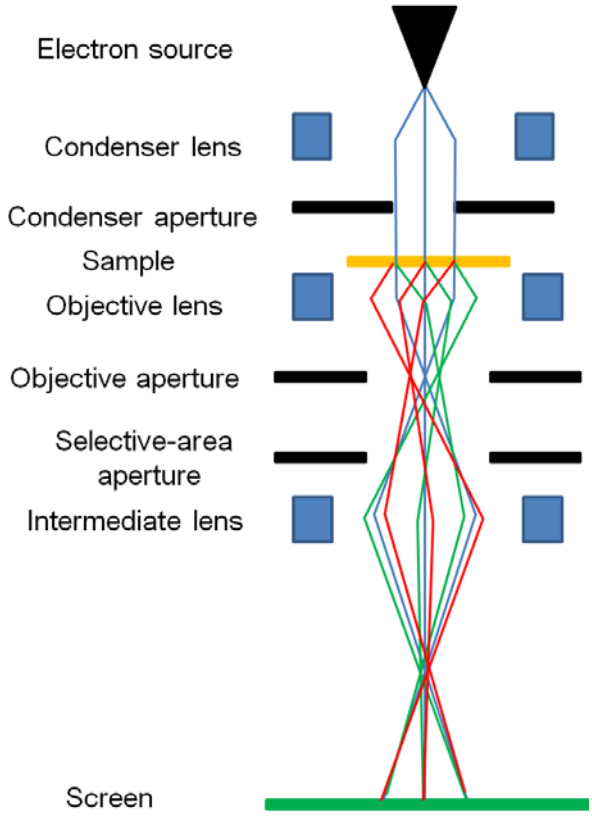

Figure 3.1 Schematic of TEM components and electron beam ray diagram for real-space imaging mode. For TEM imaging mode, broad electron beam is illuminated on a specimen. The electron beam undergoes scattering from a specimen. The red and green lines represent the electron beam scattered with reciprocal lattice vector $\vec{g}$ and $-\vec{g}$.

Most of the available lenses in TEMs are electromagnetic. The magnification or focusing strengths can be controlled by the current through a coil around a soft-iron core. This current control can alter the strength of the magnetic field inside the lenses. The condenser lenses, objective lenses, and intermediate lenses are incorporated in TEMs. However, electromagnetic lenses still suffer from severe spherical and chromatic aberrations. This is the reason that lens aberrations, not the wavelength of the electrons, determine the resolution of the TEM. A detailed discussion can be found in the **Section 3.3 Phase contrast high-resolution imaging**.

3.2.2 Diffraction mode

In the diffraction mode, the broad electron beam is illuminated onto a specimen. Figure 3.2 shows the electron beam ray diagram for diffraction acquisition mode. With a different lens configuration, electron beams with different scattering vectors are focused on different spots on the screen. Usually, a selective-area aperture is utilized in the diffraction mode to reduce the intensity of the center direct beam and obtain information with better spatial resolution. In the image screen, one encounters a diffraction pattern (DP), which is usually composed of focused beam spots and/or ring patterns. A DP contains the structural information of a specimen, including specimen lattice structure and the relative orientation of the lattice to the electron source.

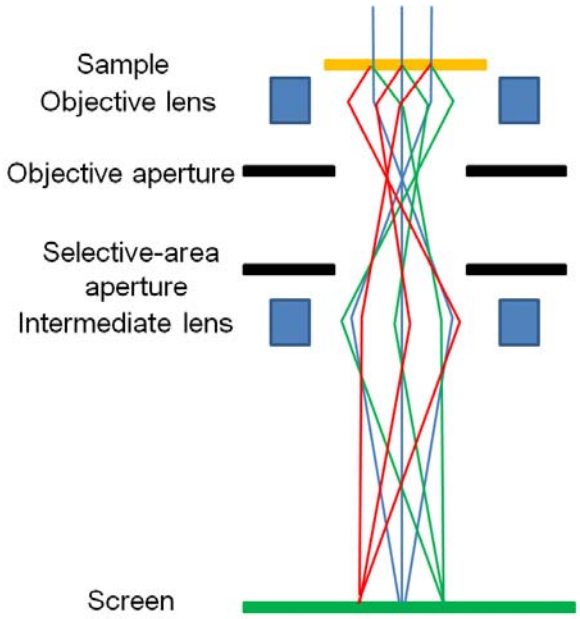

Figure 3.2 The electron beam ray diagram for diffraction acquisition mode. Electron beams with different scattering vectors are focused on distinct spots on the screen.

3.2.3 Bright-field (BF) and dark field (DF) imaging

In bright-field (BF) and dark-field (DF) imaging, an objective aperture is used to select different regions of the specimen to contribute to the diffraction patterns. A selective area DP will have a central bright spot which contains the direct electron beams (shown as blue lines in Fig. 3.2). Other diffraction spots with electrons of different scattering vectors will also be present (shown as red and green lines in Fig. 3.2). For BF imaging, an objective aperture is inserted to transmit only the center direct diffraction spot for imaging. With the objective aperture inserted, one can go back to imaging mode. Only the specimen regions which contribute to the direct diffraction spot will be selectively brightened up (Fig. 3.3a). For DF imaging, a similar procedure can be adapted except that an objective aperture will allow the transmission of electron beam with a certain scattering vector (Fig. 3.3b). The DF imaging can be used for direct graphene grain and grain boundary mapping (see Chapter 4).

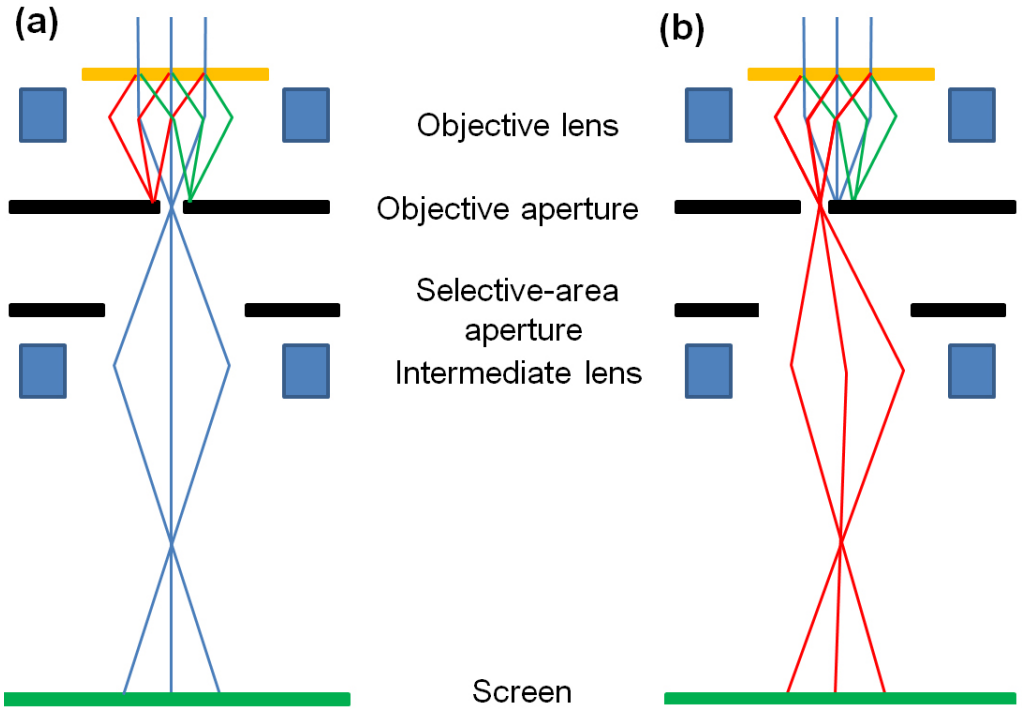

Figure 3.3 Bright field (BF) and Dark field (DF) imaging set-up. (a) Electron-beam ray diagram for BF imaging mode. An objective aperture is inserted and the center diffraction spot is only transmitted for imaging. (b) Electron beam ray diagram for DF imaging mode. An objective aperture allows the transmission of electron beam with a certain scattering vector.

3.2.4 Scanning transmission electron microscopy (STEM)

In STEM, the specimen is illuminated with a focused electron beam. The electron beam is scanned over a sample in a raster and the signal is collected in a serial acquisition mode. Different detector settings can be used for signal acquisition. Bright-field (BF) STEM collects transmitted electrons with direct electron beam (Figure 3.4). Annular dark-field (ADF) detector collects electrons which are scattered to high angle. High-angle annular dark-

field (HAADF) STEM collects electrons with even higher scattering angles. For a thin sample of constant thickness, a HAADF signal is originated from Rutherford scattering, which is proportional to about $Z^{1.7}$, where Z is the atomic number of the atom [52]. This is the reason why the HAADF STEM is usually referred to as Z-contrast imaging. In the suspended graphene sample, the HAADF signal is proportional to the number of graphene layers (see **Section 3.6.2 HAADF STEM imaging of graphene**).

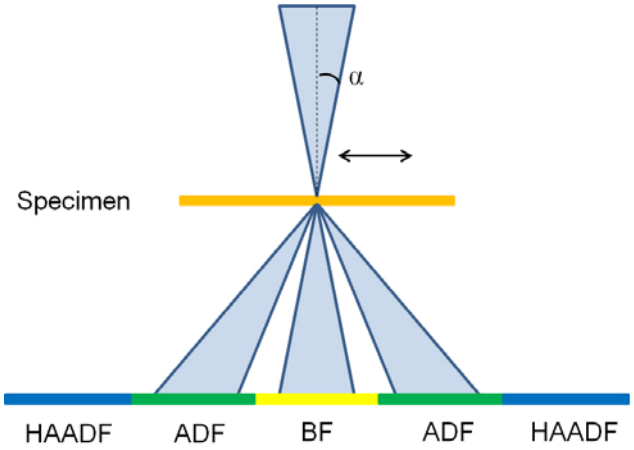

Figure 3.4 Scanning TEM set-up. Electron beam is focused to a small spot and scanned through a specimen. Diffraction detectors can be used for analysis.

3.3 Phase contrast high-resolution imaging

There are many available contrast mechanisms for high-resolution TEM imaging. Among them, phase contrast imaging utilizes the electron wave's phase shift due to interactions with specimen and is suitable for imaging the arrangement of the atoms in the specimen. The incident electron wave undergoes a phase modulation upon transmitting a thin specimen. The phase modulation, $e^{-i\phi(x,y)}$, is determined by the phase shifts, $\phi(x,y)$, which is proportional to the projected electrostatic crystal potential $V_t(x,y)$ with the following relation,

$$\phi(x,y)=\frac{\pi}{\lambda U}\int_0^t V_c(\vec{r})dz=\frac{\pi}{\lambda U}\int_0^t V_c(x,y,z)dz=\frac{\pi}{\lambda U}V_t(x,y) \qquad (3.1)$$

where λ is the wavelength of the electron, U is the acceleration voltage of the microscope, $V_c(\vec{r})$ is the electrostatic crystal potential, and t is the specimen thickness. For a very thin specimen, we can assume that a phase shift is small ($\phi(x,y)<<1$). With this weak phase object approximation (see e.g. Williams and Carter [48]), the exit-wave, $\psi_{exit}(x,y)$, from a thin specimen is given by the incident wave $\psi_{in}(x,y)=1$ multiply by the phase modulation,

$$\psi_{exit}(x,y)=\psi_{in}(x,y)e^{-i\phi(x,y)}=1-i\phi(x,y) \qquad (3.2)$$

The wave function in the frequency domain (also at the back focal plane), $\psi_{exit}(\vec{q})$, is the

Fourier transform of the exit-wave, $\psi_{exit}(x,y)$.

$$\psi_{exit}(\vec{q}) = F[\psi_{exit}(x,y)] \tag{3.3}$$

where $\vec{q}$ is a two-dimensional vector of the spatial frequency spectrum.

For a microscope, $T(\vec{q}) = \mathrm{Re}[T(x,y)] + i\,\mathrm{Im}[T(x,y)]$, a two-dimensional complex transfer function, which is dependent on the imaging conditions and other microscope parameters, describes the characteristics of TEM imaging. After undergoing the TEM imaging process, the wavefunction is distorted by the transfer function $T(\vec{q})$, such that $\psi(\vec{q}) = \psi_{exit}(\vec{q})T(\vec{q})$. This can be rewritten in the real-space as

$$\psi(x,y) = \psi_{exit}(x,y) \otimes T(x,y) \tag{3.4}$$

where the symbol $\otimes$ denotes the convolution of two functions. With the Eq. (3.2) and Eq. (3.4), we obtain

$$\begin{aligned} \psi(x,y) &= (1 - i\phi(x,y)) \otimes T(x,y) \\ &= 1 + \phi(x,y) \otimes \mathrm{Im}[T(x,y)] - i\phi(x,y) \otimes \mathrm{Re}[T(x,y)] \end{aligned} \tag{3.5}$$

The image intensity at the TEM imaging plane have the following relation.

$$I(x,y) = \left|\psi(x,y)\right|^2 = 1 + 2\phi(x,y) \otimes \mathrm{Im}[T(x,y)] + \mathrm{O}(\phi^2) \tag{3.6}$$

From Eq. (3.6), we can understand that the imaginary part of the transfer function *T* will determine the intensity modulation in a TEM image.

For a direct translation of structural information of specimen to a TEM imaging, $T(\vec{q})$ should be optimized. Generally, optimizing $T(\vec{q})$ means constructing a broad band-pass, where the phase shift is maintained to have similar values for a certain frequency domain. For example, $T(\vec{q})$ is dependent on the lens aberration $\chi(\vec{q})$ by the following relation.

$$T(\vec{q}) \propto \exp\left(-\frac{2\pi i}{\lambda}\chi(\vec{q})\right) \tag{3.7}$$

For a conventional electron microscope, the third-order spherical aberration C_3 is the geometrical limiting factor for the image resolution and $\chi(\vec{q})$ is determined by the defocus value C_1 and the third-order spherical aberration C_3 by

$$\chi(\vec{q}) = \chi(q) = \frac{1}{2}q^2\lambda^2 C_1 + \frac{1}{4}q^4\lambda^4 C_3 \tag{3.8}$$

From Eq. (3.7) and (3.8), the imaginary part of the transfer function becomes

$$\mathrm{Im}[T(\vec{q})] \propto \exp\left(-\frac{2\pi i}{\lambda}\chi(\vec{q})\right) = \sin\left(-\frac{2\pi i}{\lambda}\left(\frac{1}{2}q^2\lambda^2 C_1 + \frac{1}{4}q^4\lambda^4 C_3\right)\right) \tag{3.9}$$

The equation (3.9) is an oscillating function with respect to *q* and has many zeros (or crossovers). Scherzer found a way to optimize the transfer function by balancing the effect of the third-order spherical aberration by a negative defocus value C_1 [53]. At this particular defocus value (Scherzer focus C_{sch}), the transfer function will have the nearly constant value out to the first crossover.

$$C_{Sch} = -\sqrt{\frac{4}{3}\lambda C_3} \tag{3.10}$$

At Scherzer defocus value, we find that the first crossover at

$$q_{Sch} = 1.51(C_3\lambda^3)^{-\frac{1}{4}} \tag{3.11}$$

The *point resolution* of a microscope is defined as the reciprocal of q_{Sch} as

$$\rho_r = 1/q_{Sch} = 0.66(C_3\lambda^3)^{\frac{1}{4}} \tag{3.12}$$

and reflects the highest spatial resolution for phase contrast imaging, where the direct structural interpretation is possible.

3.4.1 Spherical aberration corrector

The positive spherical-aberration value of C_3 is associated with the lens system with rotational symmetry along the electron beam axis. In principle, by breaking the rotational symmetry of the lens, the spherical aberration C_3 can be minimized and even canceled, leading to the better spatial resolution of a microscope. Two types of multi-pole lenses are currently used for the C_3 correction. These are based on either hexapoles or the combination of quadrupole and octupole elements [54].

The spherical aberration correction can be applied to image-correction (TEM imaging mode) or probe-correction (STEM mode). Aberration corrector lenses are placed behind the objective lens for image-correction while the corrector lenses are located before the objective lens for probe-correction [54]. A microscope with both correctors is called a double-corrected microscope.

For the image-corrector, the hexapole-based system is the currently dominant design. From the extended hexapole magnetic field, a negative third-order spherical aberration C_3 can be introduced [54]. However, the main effect of hexapole-lens is the introduction of three-fold astigmatism A_2. By utilizing *two* extended hexapole elements with inverted electron-beam paths, A_2 can be canceled out while the negative C_3 adds up [54]. The overall negative C_3 from the image-corrector can effectively cancel out the positive value of C_3 from the lens system. C_3 can be further tuned to have an overall negative value.

For an aberration-corrected microscope with the hexapole design, the residual aberrations are of fifth order. The fifth-order spherical aberration C_5 and the six-fold astigmatism A_5 are the limiting factors for determination of the geometrical resolution [54]. Similar to the Scherzer focus, there are conditions that allow for optimizing the phase contrast transfer function of a microscope whose C_3 is adjustable. One recent optimization method and parameters are describe by M. Lentzen [55],

$$\begin{aligned} C_{1,Lentzen} &= \frac{2}{\lambda q_{\max}^2} + \frac{2}{15} C_5 \lambda^4 q_{\max}^4 \\ C_{3,Lentzen} &= -\frac{10}{3\lambda^3 q_{\max}^4} - \frac{8}{9} C_5 \lambda^2 q_{\max}^2 \end{aligned} \tag{3.13}$$

where $q_{\max}$ is the maximum spatial frequency that contributes to the image formation.

3.4.2 TEAM 0.5 at NCEM

TEAM 0.5, located at National Center for Electron Microscopy (NCEM) of Lawrence Berkeley National Laboratory, was used for atomic-resolution imaging for my study. The information on NCEM and TEAM 0.5 can be found at http://ncem.lbl.gov/ and http://ncem.lbl.gov/team/TEAMpage/TEAMpage.html, respectively. NCEM is a user facility and one needs to have an accepted research proposal for the access of microscopes at NCEM, including TEAM 0.5. TEAM 0.5 is equipped with image C_3 corrector and monochromator.

3.4.3 Aberration assessment and correction processes

At TEAM 0.5 microscope, the semi-automatic software is used for aberration assessment and aberration correction (Fig. 3.5 and 3.6). The software utilizes diffractograms computed from images of an amorphous specimen, usually thin amorphous carbon. The obtained diffractogram reflects the transfer function of a TEM. Diffractogram tableau, sometime also called as Zemlin-tableau [56], is acquired as the electron beam is tilted at a series of different tilting angles.

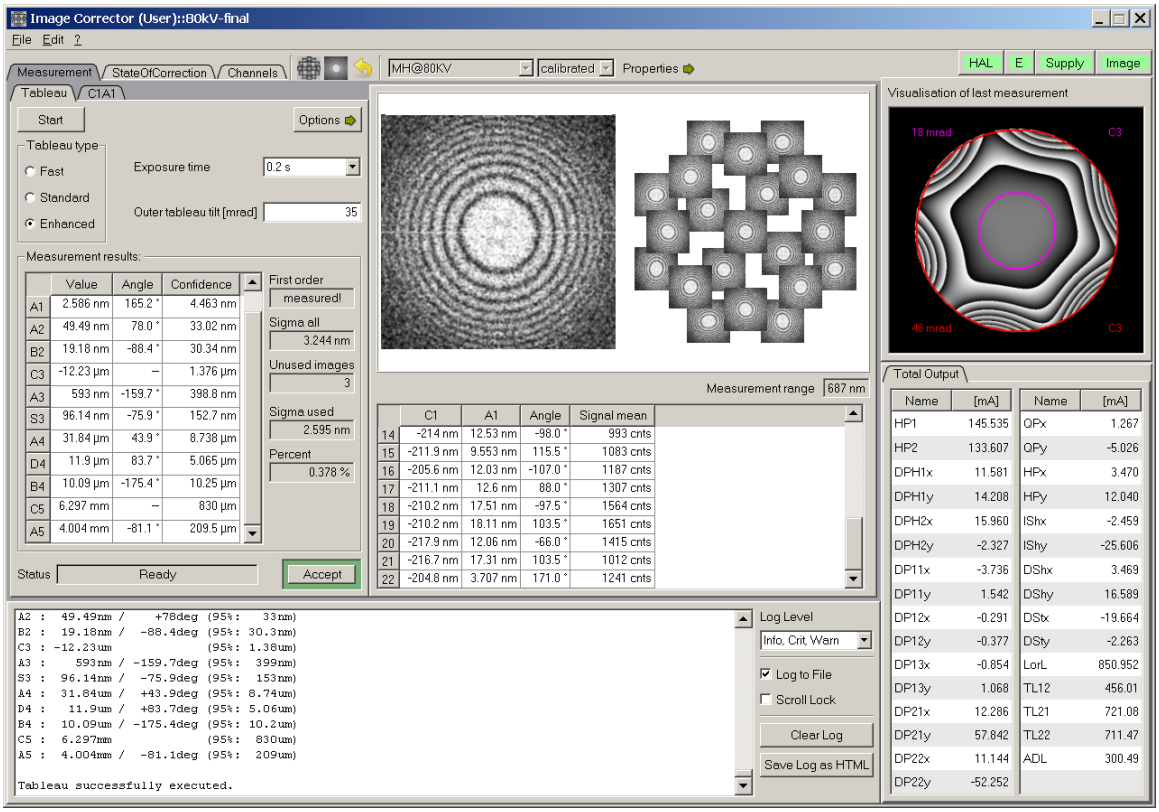

Figure 3.5 Front panel of image-aberration corrector software at TEAM 0.5. The semi-automatic software is available for aberration assessment and aberration correction. With an obtained diffractogram tableau, a list of aberration is calculated. Microscope lens configuration is adjusted to compensate the previously obtained aberrations. An acquisition of a new diffractogram and aberration assessment is followed. This process is repeated until the optimized aberration values are reached.

(a)

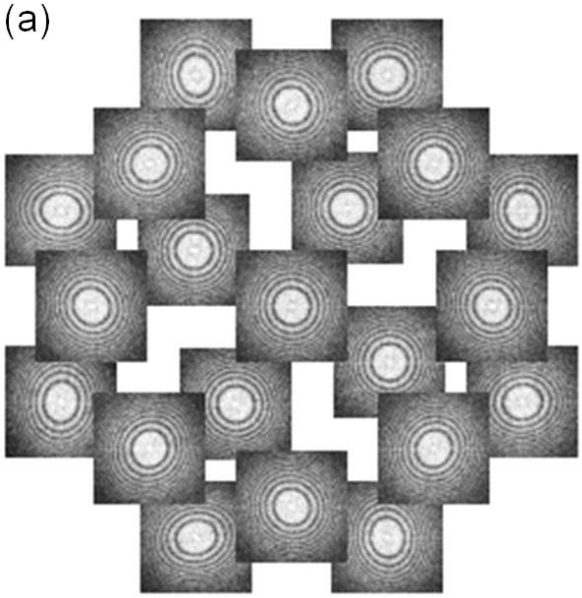

(b)

Measurement results:

	Value	Angle	Confidence
A1	2.586 nm	165.2 °	4.463 nm
A2	49.49 nm	78.0 °	33.02 nm
B2	19.18 nm	-88.4 °	30.34 nm
C3	-12.23 µm	–	1.376 µm
A3	593 nm	-159.7 °	398.8 nm
S3	96.14 nm	-75.9 °	152.7 nm
A4	31.84 µm	43.9 °	8.738 µm
D4	11.9 µm	83.7 °	5.065 µm
B4	10.09 µm	-175.4 °	10.25 µm
C5	6.297 mm	–	830 µm
A5	4.004 mm	-81.1 °	209.5 µm

Figure 3.6 Diffractogram tableau and extracted aberration values. (a) Diffractogram tableau of the TEAM 0.5 operated at 80 kV. Maximum 35 mrad tilting was used for tableau acquisition. (b) Extracted aberration values from the tableau measurement. For example, C_3 (~ -12.2 µm) and C_5 (~ 6.3 mm) are the third-order and fifth-order spherical aberration values.

First-order aberration, two-fold astigmatism, can be determined without the electron beam tilting. On the other hand, high-order aberration parameters are only discernible when the electron beam is tilted (Fig. 3.7). Figure 3.7 shows diffractogram tableau characteristics for the axial aberrations up to third order. One can easily observe the different aberration effects to the diffractogram tableau.

With an obtained diffractogram tableau, a list of aberration can be calculated (Fig. 3.5 and 3.6). Then the lens configurations of the microscope are adjusted to compensate the previously-obtained aberrations. The acquisition of a new diffractogram tableau and the calculation of aberrations are followed. This process is repeated until the optimized aberration values are reached. For my study with TEAM 0.5, the C_3 is set around – 15 µm, which is closed to the optimized value by Lentzen [55].

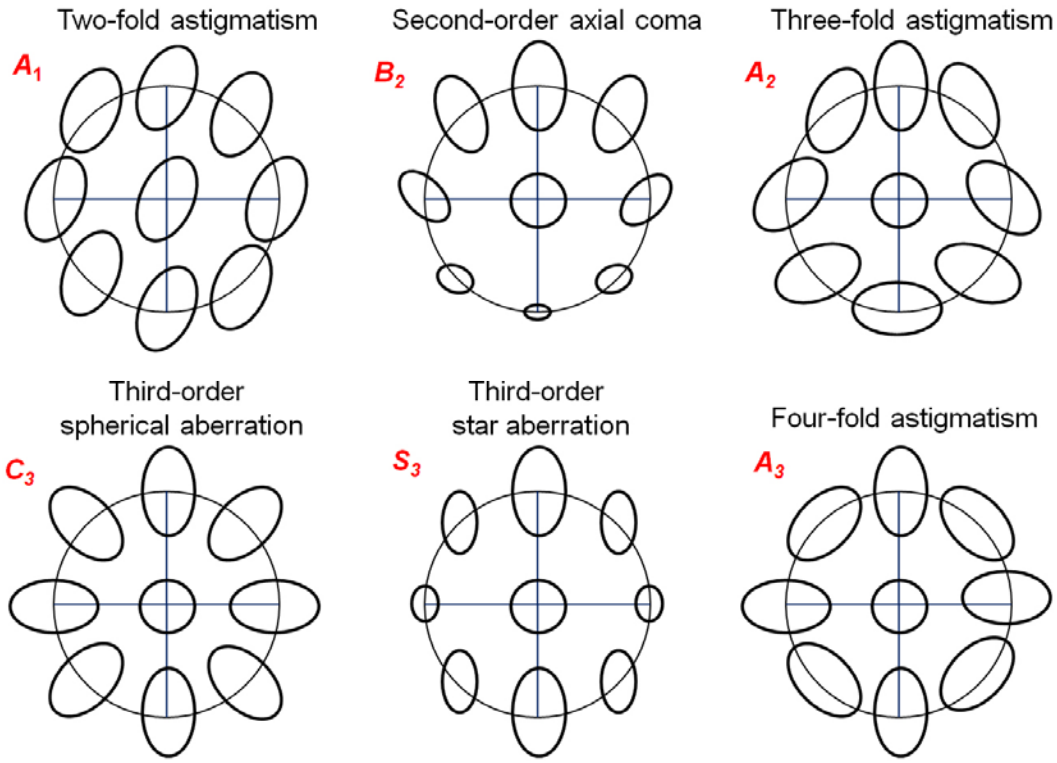

Figure 3.7 Diffractogram tableau characteristics for the axial aberrations up to third order. First-order aberration (two-fold astigmatism) shows the elliptical distortion even without the electron beam tilting. From second-order aberrations, the distortion is discernible only with tilting. As the second-order aberrations, there are second-order axial coma and three-fold astigmatism.

3.5 Electron diffraction analysis of graphene

In this section, I will briefly discuss the basic TEM characterization of graphene, focusing on graphene's diffraction analysis. Figure 3.8 shows the graphene's lattice structure. Graphene has a hexagonal lattice structure with primitive translation vectors, $\vec{a}_1$ and $\vec{a}_2$ ($|\vec{a}_1| = |\vec{a}_2| = 2.46\,\text{Å}$). The third translation vector ($\vec{c} = \vec{a}_3$), which direction is normal to the graphene membrane, can be added to construct a three-dimensional lattice for multilayer graphene or graphite. The distance between the first neighboring carbon-carbon atoms is 1.42 Å. Therefore, to directly resolve the graphene lattice structure with single-atom resolution, the spatial resolution of the microscope should be better than 1.42 Å.

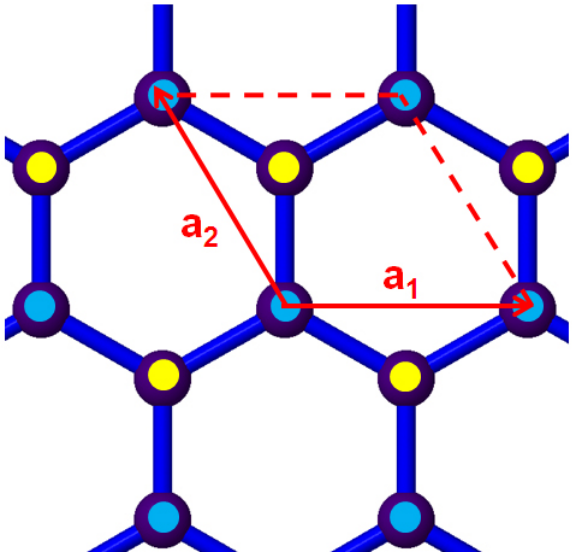

Figure 3.8 The atomic structure of graphene lattice. Graphene has a hexagonal lattice with two sublattice atoms (shown in yellow and bright blue). Inter-atomic distance is 1.42 Å and lattice parameter is $|a| = 2.46$ Å.

In single-layer graphene, there are two sublattice atoms, atom A (shown with yellow circles) and atom B (shown with blue circles). The associated atomic basis for atom A and atom B can be written as $\vec{r}_1 = (0,0,0)$ and $\vec{r}_2 = (1/3, 2/3, 0)$ in the graphene lattice $\vec{R} = (\vec{a}_1, \vec{a}_2, \vec{a}_3)$. The reciprocal lattice vectors $\vec{g}_j$ $(j = 1,2,3)$ of the graphene lattice satisfy the relations [57],

$$\vec{a}_i \cdot \vec{g}_j = \delta_{ij} \tag{3.14}$$

where the δ_{ij} is the Kronecker delta function.

The diffracted electron wavefunction with a wavevector $\Delta\vec{k}$ can be written as

$$\begin{aligned} \Psi(\Delta\vec{k}) &\propto \sum_{\vec{R}_i}^{Lattice} \sum_{\vec{r}_i}^{Basis} f_{at}(R_i + r_i) e^{-2\pi i \Delta\vec{k}\cdot(\vec{R}_i + \vec{r}_i)} \\ &= \sum_{\vec{R}_i}^{Lattice} e^{-2\pi i \Delta\vec{k}\cdot\vec{R}_i} \sum_{\vec{r}_i}^{Basis} f_{at}(r_i) e^{-2\pi i \Delta\vec{k}\cdot\vec{r}_i} \end{aligned} \tag{3.15}$$

where f_{at} is the atomic form function which depends on the atomic number Z and the incident electron energy. The electron wavefunction (Eq. 3.15) is non-zero only if $\Delta\vec{k} = \vec{g} = m\vec{g}_1 + n\vec{g}_2 + h\vec{g}_3$, where m and n are integer. By replacing $\Delta\vec{k}$ with $\vec{g}$, the wavefunction becomes

$$\begin{aligned}\Psi(\Delta\vec{k}) &\propto N f_g \sum_{\vec{r}_i}^{Basis} e^{-2\pi i \vec{g}\cdot\vec{r}_i} \\ &= N f_{g(m,n)}(1+e^{-2\pi i(m/3+2n/3)}) \\ &\equiv N \cdot S(m,n,h)\end{aligned} \tag{3.16}$$

where N is the number of unit cells in graphene lattice and S is the structural factor of graphene lattice. The diffraction pattern will represent the reciprocal lattice of the graphene, which also shows the hexagonal symmetry. The diffraction spot intensity is proportional to the square of the wavefunction $I^2 = \left|\Psi(\Delta\vec{k})\right|^2$ or the square of structural factor ($I^2 \propto \left|S(m,n,h)\right|^2$). Therefore, the intensity ratio between different diffraction spots can be calculated by the associated structural factors.

When the incident electron beam is perpendicular to the graphene membrane (normal incident), the first-order and second-order diffraction spots are observed at $\vec{g}_{100} = \vec{g}_1$ ($\left|\vec{g}_{100}\right| = 1/2.13$ (1/Å)) and $\vec{g}_{110} = \vec{g}_1 + \vec{g}_2$ ($\left|\vec{g}_{110}\right| = 1/2.13$ (1/Å)). The intensity ratio between the first-order and second-order diffraction spots has been used to assess the number of graphene layers in Bernal-stacked samples [17, 58] and can be calculated as following.

$$\frac{I_{110}}{I_{100}} = \frac{\left|S(1,1,0)\right|^2}{\left|S(1,0,0)\right|^2} = \left|\frac{f_{g(1,1)}}{f_{g(1,0)}}\frac{2}{1+e^{-2\pi/3}}\right|^2 \tag{3.17}$$

The atomic form factor is the function of a parameter, $s \equiv \sin\theta/\lambda$, which can be defined as

$$s \equiv \sin\theta/\lambda = 1/2d = g/2 \tag{3.18}$$

where d is the associated spacing of atomic planes for diffraction. The numerical values of the atomic form factors f_g for electrons can be found in the Appendix A.5 of the reference [49].

With these form factor values, we find that $I_{110}/I_{100} \sim 1$. Indeed, the selective area diffraction of single-layer graphene confirms this intensity ratio (Fig. 3.9). With the AB-stacked (Bernal stacking) bilayer graphene, the same procedure of the calculation gives us the intensity ratio about 4, which was also previously confirmed [17, 58].

Please note that a different indexing (Miller-Bravais indices) can be used for hexagonal structure such as graphene. Instead of using three indices, Miller-Bravais indices are represented with four indices and show the symmetry of the hexagonal structure in a better way.

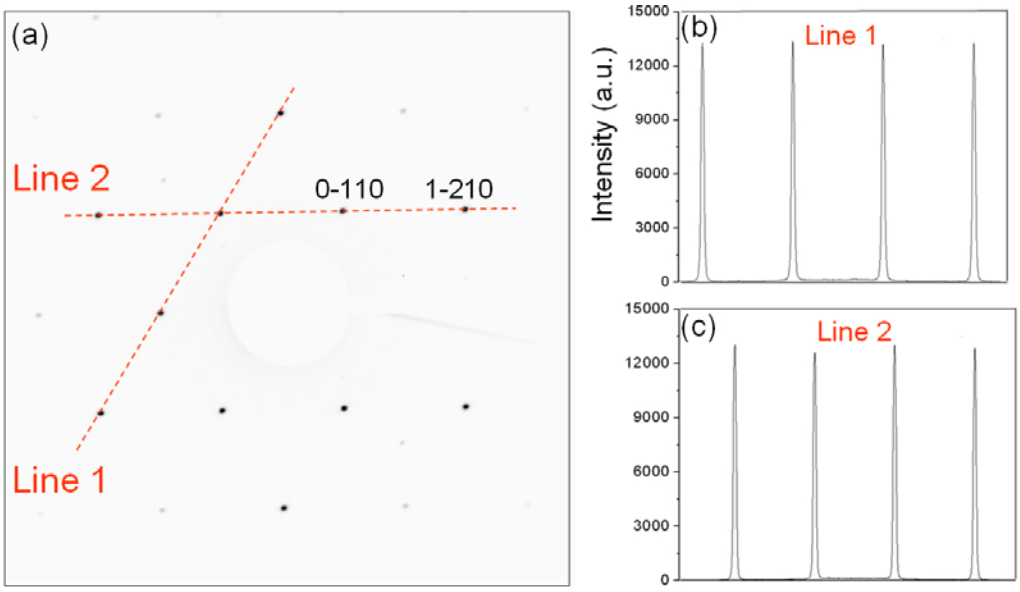

Figure 3.9 Diffraction pattern evidence of single-layer graphene. (a) The diffraction shows the hexagonal spot patterns. (b-c) Line intensity profiles show 1:1 intensity ratio between (0-110) and (1-210) spots, which indicates that the graphene is single-layer. The diffraction pattern was acquired using a nano parallel electron beam of 830 nm diameter in STEM mode of Libra MC 200.

3.6.1 Atomic-resolution TEM imaging of CVD graphene

Using TEAM 0.5 microscope, we can obtain atomic-resolution image of CVD graphene. Figure 3.10 is an atomic resolution TEM image of monolayer region in CVD graphene. TEAM image was acquired at 80 kV with a monochromator. The imaging conditions with C_3 of -15 µm and 10 nm focus (C_1) values produce a bright atom contrast. Clear hexagonal structures are observed in the image.

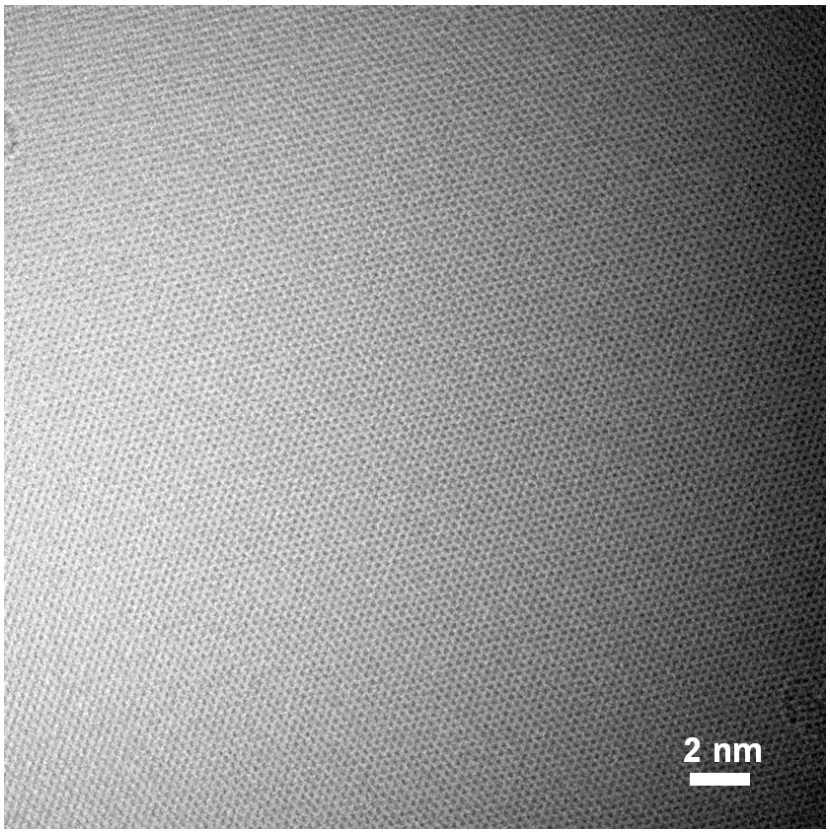

Figure 3.10 Single-shot atomic resolution TEM image of large-area monolayer graphene grown by CVD synthesis on copper foil. The image shows a pristine region of single-grain monolayer graphene. We find that the graphene is mostly single-layer (> 90 % of sample area) and of high quality as shown in this image. The TEM image was acquired using an aberration-corrected TEM at 80 keV equipped with a monochromator (TEAM 0.5).

3.6.2 HAADF STEM imaging of graphene

HAADF STEM imaging is a good way to visualize the suspended graphene. STEM imaging can be utilized to show that CVD graphene of large area can be perfectly transferred to commercial TEM grids, similar to SEM. Especially, the intensity of HAADF image can be used for identification of number of layers in graphene (Figure 3.11 and 3.12). Around the multilayer regions, the intensity increases stepwise and we can assign the number of graphene layers accordingly. In usually CVD synthesis conditions, non-single-layer region is less than 10 % of the sample area (Figure 3.11).

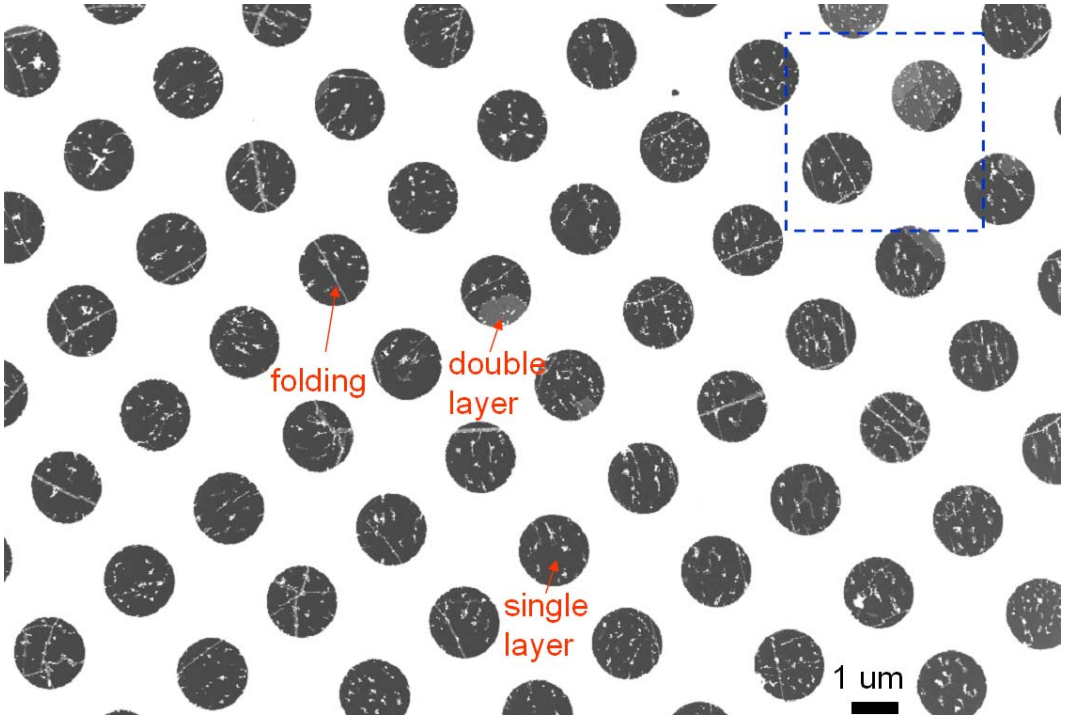

Figure 3.11 HAADF Scanning TEM (STEM) image of suspended graphene sample. The image shows the graphene transferred onto a commercial TEM grid (Quantifoil holey carbon). Graphene of large area (greater than 20 um × 20 um) can be perfectly transferred to commercial TEM grids with our direct transfer method. We also observe that there are line features (local foldings) and double- or triple-layer graphene regions in some portions of the sample. The non-single-layer regions comprise less than 10 % of the sample area. The amorphous carbon grid support has a higher intensity than the graphene because of higher scattering resulting from a thicker carbon layer. The blue dashed rectangle is the field of view for the zoomed-in image in Figure 3.11a. Some residual particles appear bright on the graphene membrane.

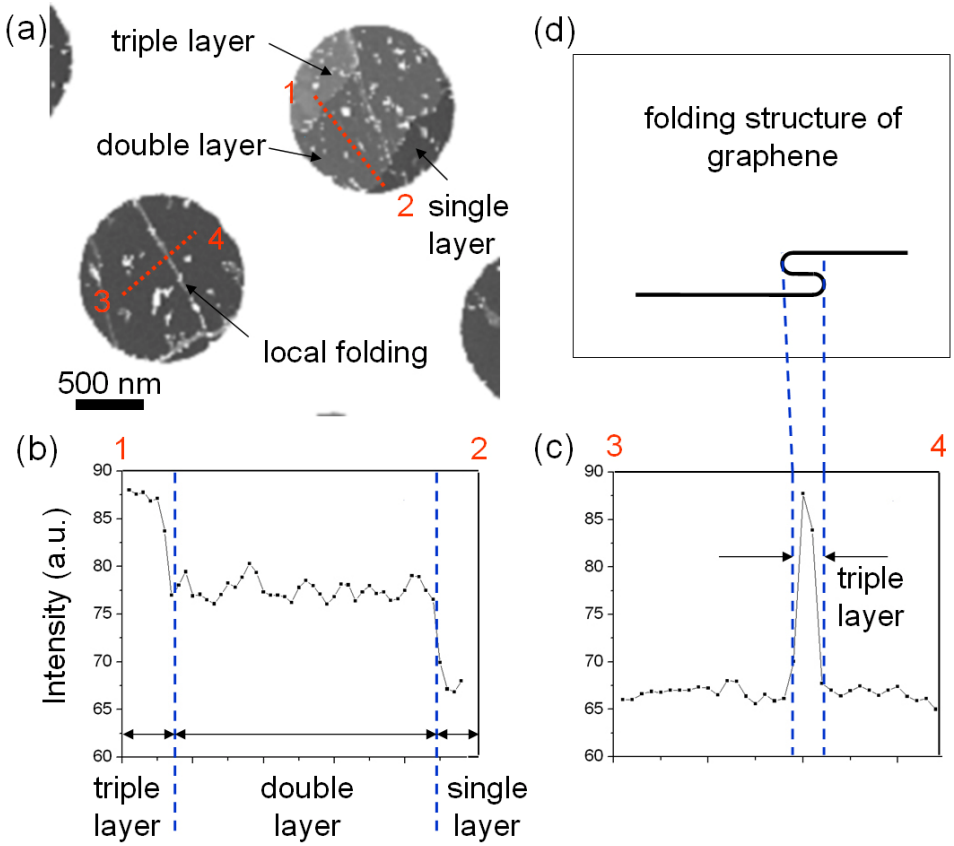

Figure 3.12 Number of layer identification in graphene through STEM intensity analysis. (a) Zoom-in of graphene STEM image from Figure 3.10. Some regions and line features have distinguishable contrast from single-layer graphene. (b) Intensity profile along the line 1-2 in Figure a. The intensity increases stepwise as the number of graphene layers increases. We can assign the number of graphene layers from one to three. (c) Intensity profile along line 3-4 in Figure a. In the line feature, the intensity shows what we estimate for triple-layers. (d) Proposed folding structure from figure c. The folding of monolayer graphene locally produces triple-layer graphene.

3.7 Microscopy and analysis software

There is lots of software available for all the fundamental aspects of microscopy including atomic resolution imaging and diffraction simulation. Some of my graphene studies have utilized a microscopy software, MacTempas and CrystalKit, which is a Macintosh-based image analysis program. The related software information can be found at http://www.totalresolution.com/index.html.

Chapter 4
Grain and grain boundary mapping in polycrystalline CVD graphene

Large-area synthesis of high-quality but *polycrystalline* graphene has been recently advanced as a scalable route to applications including electronic devices [19, 30-32, 40]. The presence of grain boundaries (GBs) may have detrimental effects on some electronic, thermal, and mechanical properties of graphene, including reduced electronic mobility [19, 30-32], lower thermal conductivity [59], and reduced ultimate mechanical strength [60], yet on the other hand GBs might be beneficially exploited *via* controlled GB engineering [61]. The study of graphene grains and their boundary is therefore critical for a complete understanding of this interesting material and for enabling diverse applications.

Since graphene is a two-dimensional one-atom-thick carbon membrane, the GB in graphene is a one-dimensional entity. This is in contrast to regular three-dimensional materials for which the GB is a two-dimensional surface. The GB of graphite has been investigated using scanning tunneling microscopy (STM) for over twenty years [62-65], and more recently STM and other surface studies of grains and boundaries have been performed on epitaxially-grown graphene on single crystal substrates [36, 38, 66-69]. Unfortunately, such surface probe techniques are either extremely time-consuming and not appropriate for large-area characterization [38, 62-69] or lack suitable spatial resolution in the case of low energy electron diffraction and microscopy [36, 38]. Moreover, true atomic-resolution imaging at the GB of graphene unperturbed by the substrate structure has not been achieved, hindering fundamental understanding of the electronic and mechanical properties of polycrystalline graphene structures.

TEM, a direct and relatively fast imaging tool ideally suited for suspended atomically-thin membranes, has been successfully applied to study adsorbates on graphene using modest-resolution machines [70] and, using aberration-corrected instrumentation, to the local atomic structure of graphene itself [71-73]. In this chapter, I will show that scanning electron diffraction in STEM mode (SED-STEM) makes possible fast and direct identification of GBs. We also demonstrate that dark field (DF) TEM imaging techniques allow facile GB imaging for high-angle tilt GBs in graphene. GB mapping is systematically carried out on large-area graphene samples *via* these complementary techniques. The study of the detailed atomic structure at a GB in suspended graphene uses aberration-corrected ultra-high resolution TEM, which shows the theoretically-predicted alternating pentagon-heptagon structure along high angle GBs.

Grains and GBs are identified using SED-STEM, which involves scanning a nano parallel electron beam (NPEB) across a suspended graphene membrane in the diffraction mode of STEM. A related diffraction acquisition method with scanning micron-size beam has been previously used for domain mapping of polycrystalline films [74]. When the electron beam laterally traverses a tilt GB, gradual transitions are observed from one hexagonal-set

diffraction to a relatively-rotated set (Figure 4.1); each set results from an individual grain of single-layer graphene. Experimentally obtained graphene diffraction patterns at a transition are shown in Figs. 4.1b-d. Diffraction patterns are acquired with a NPEB of 45 nm diameter in Libra 200MC at NCEM. The hexagonal diffraction pattern (A spots) in Figure 4.1b transitions to a relatively-rotated hexagonal pattern (B spots) in Fig. 4.1d. There are intermediate locations in which both hexagonal patterns appear together in a single diffraction graph, as shown in Figure 4.1c. This occurs when the electron beam simultaneously probes both grains at the interface. Across the transition, the intensity profiles of diffraction A spots show an expected diminishing trend, and those of B spots show an expected intensifying trend, as the area of the associated grain (or number of carbon atoms in its associated graphene grain lattice) under the electron beam illumination respectively decreases or increases, as shown in Fig. 4.1e and 4.1f.

Intensity variations of A spots, B spots, and their sum across the transition are shown in Fig. 4.1f. Importantly, the intensity sum of A and B spots is nearly constant over the transition. This is compelling evidence that the transition is due to a tilt GB, and not another microstructures such as foldings or overlapping of two misoriented graphene sheets. Compared to single layer graphene, such overlapping microstructures have multi-layer regions and would therefore increase the effective area of crystalline graphene under electron illumination, which would lead to an increase of the intensity sum at a transition, contrary to observations.

The graphene grain's lateral isolation in the sample plane also enables us to perform dark field (DF) TEM imaging for facile GB identification in the case of highly-rotated ($> \sim 10$ degree) tilt GBs. Fig. 4.2a shows a bright field (BF) TEM image of graphene (prepared on a commercial Quantifoil holey carbon grid) where a diffraction transition occurs. There are no special features which appear to be GBs in the BF image. Fig. 4.2b shows a diffraction pattern with two sets of hexagonal patterns at the transition, which are relatively rotated by 25.6 degrees. We selectively obtain the bright contrast enhancement in one grain by transmitting only a single diffraction spot (marked with dotted circles c or d) with a small objective aperture. Fig. 4.2c clearly reveals that the left side is brighter than the right side of the DF image, which is divided by a sharp line feature. The illumination change to the other transmitted diffraction spot produces a DF image with the inverted contrast in the graphene area (Fig. 4.2d), while the line feature does not change. There is no overlap between the two bright regions in the two DF images, Figs. 4.2c and 4.2d. This demonstrates that the line feature thus identified is a GB, not a local overlapping of two distinct graphene structures. We note that the GB is generally straight but changes its direction locally along the boundary in this magnification range.

We have used both SED-STEM and DF-TEM to map out graphene grains and their boundaries over a scale large enough to encompass multiple grains. In a pre-collected SED-STEM image, we mark and compile the locations where diffraction patterns make transitions for tracing a grain map. The DF technique can confirm this mapping process at high-angle GBs. Fig. 4.3a shows a graphene GB map overlaid on the corresponding STEM image. The annotated angles inside the grains are the relative angles of the grain's hexagonal diffraction pattern measured against a reference grain (overlaid in red) at the central region. We determine a graphene grain size in the range of $3 \sim 10$ μm using our synthesis conditions. One should caution that identified grain boundaries in this study are restricted to the cases of tilt

grain boundaries. Even though non-tilted grain boundaries can exist in graphene [68], SED-STEM and DF-TEM methods are only applicable for visualizing tilt grain boundaries in graphene. Aberration-corrected TEMs, which will be discussed later in this article, can be utilized to image non-tilted grain boundaries.

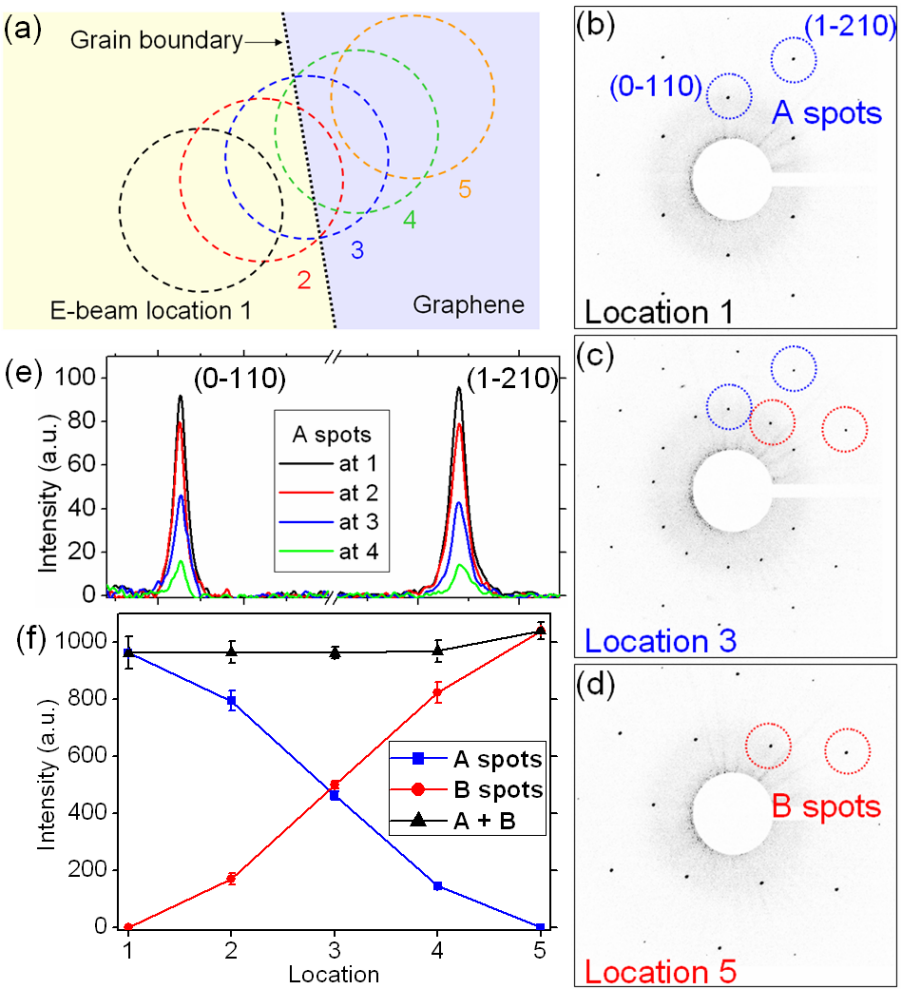

Figure 4.1 Grain boundary (GB) identification through diffraction series on a graphene sheet. (a) Schematic of GB identification through a series of diffraction pattern acquisitions. The dotted straight line is a tilt GB of graphene dividing the left and right side of the graphene membrane. A series of diffraction acquisitions across a GB will produce a transition from one set of hexagonal diffraction patterns to a relatively-rotated set. (b-d) Experimentally obtained diffraction patterns at a transition. Diffraction patterns are acquired with a nano parallel electron beam of 45 nm diameter. (b) Diffraction pattern showing a set of hexagonal pattern from single-layer graphene. (c) Diffraction pattern showing two sets of the hexagonal pattern, which are relatively rotated by 26.0 degrees. (d) Diffraction pattern with a different hexagonal pattern after the completion of a transition. (e) The intensity profiles of diffraction A spots across the transition. The left and right peaks are the intensity profiles for (0-110) and (1-210) spots. (f) Intensity variations of A spots, B spots, and their sum across the transition.

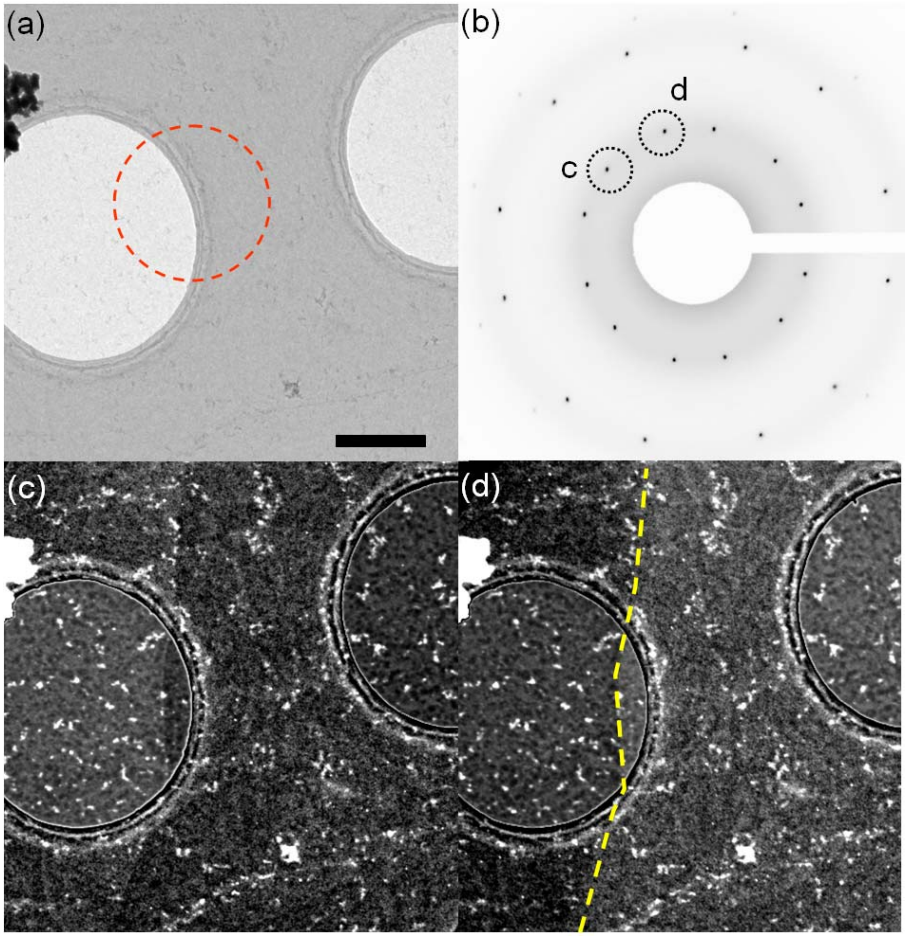

Figure 4.2 Imaging of a graphene GB *via* TEM dark field imaging. (a) TEM bright field image of graphene on a commercial TEM grid (Quantifoil holey carbon) at a diffraction transition. The red dashed circle is the field of view for the diffraction pattern acquisition for Fig. b. The scale bar is 500 nm. (b) Diffraction pattern with two sets of the hexagonal pattern, showing a 25.6 degree misorientation. Diffraction spots circled by dashed line c and d are transmitted for dark field imaging, respectively, for the figure c and d. Amorphous carbon of the TEM grid contributes the halo pattern to the diffraction pattern. (c) Dark field (DF) TEM image of the same area from (0-110) diffraction spot. The left side is brighter than the right side of the image, separated by a line (the GB). (d) DF TEM image with (0-110) spot d from the other set of hexagonal diffraction spots shows the inverted contrast in the graphene area. For Fig. c and d, the brightness is adjusted separately between inside and outside of the amorphous carbon holes. The yellow dashed line is a guide to the eye for the graphene GB.

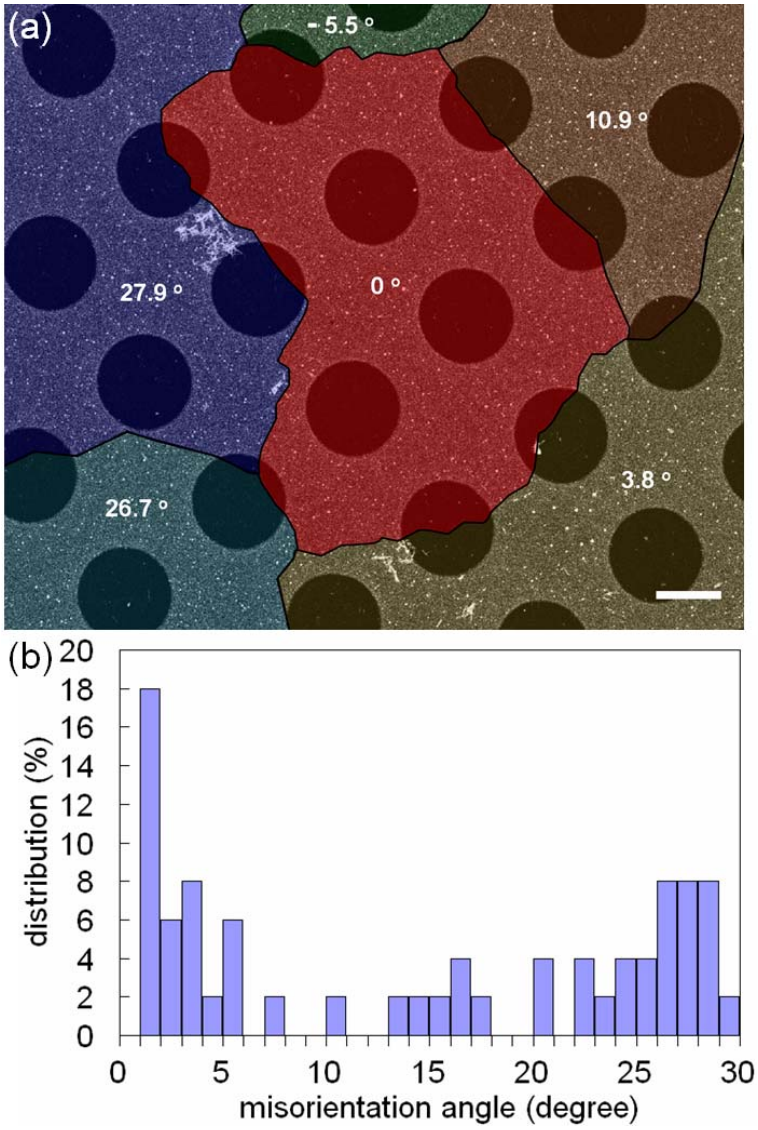

Figure 4.3 Graphene GB mapping. (a) GB map with an overlaid background of the graphene STEM image. The annotated angles inside each grain are the relative angles of hexagonal diffraction pattern measured against the grain at the center. The grain mapping was performed mainly using a nano parallel electron beam of size ~ 45 nm in STEM mode. The scale bar is 1 um. (b) Distribution of misorientation angles between adjacent grains. 50 misorientation angles are measured from rotational angles between two sets of hexagonal diffraction patterns. There are more populations around 0 and 30 degrees than middle-range angles.

Macroscopic mapping of graphene GBs additionally allows us to systematically investigate the relative misorientation angles between adjacent grains (Figure 4.3b). A misorientation angle can be defined to be smaller than 30 degrees in our study due to the hexagonal symmetry. It is found that significant portions of misorientations are located around 0 degrees (low-angle tilt GB) and 30 degrees (high-angle). The reported grain size of

the polycrystalline copper used for our graphene synthesis is approximately 100 μm [31], which is much bigger than the graphene grain size we have found here. Hence numerous graphene GB formations occur within a single copper grain. The high percentage of 0 and 30 degree misorientations implies that there are interactions from the copper substrate causing the preferential lattice alignment of graphene during the graphene synthesis. A related study correlating preferential growth directions of graphene with the crystalline direction of the underlying Cu(111) substrate has been recently reported [69]. Further systematic study of graphene synthesis on single-crystal and polycrystalline copper will help in understanding graphene growth and subtrate alignment.

Aberration-corrected TEMs have been used to image atomic defects on carbon nanotubes and graphene including vacancies and topological defects [71-73]. Recently, there has been a report of GB-like structures in few-layer graphene, but the atomic structure could not be clearly resolved due to multi-layer interference [75]. Copper-catalyzed CVD graphene is ideal for atomic resolution GB imaging as it is mainly single-layer and offers large sample areas with multiple GBs. We have investigated suspended CVD-grown graphene in the TEAM 0.5 aberration-corrected microscope. We start by scanning a graphene sample while monitoring its diffraction pattern. When the diffraction pattern shows a transition of the diffraction angle, we stop moving the sample stage and perform atomic resolution imaging at the transition region.

Fig. 4.4 confirms that tilt GBs are the origin of the diffraction transitions we have observed. Fig. 4.4a shows an atomic resolution image of a high-angle tilt GB of single-layer graphene, which is acquired using image Cs aberration-correction with a monochromated beam at 80 kV. The left and right parts of the image are two different grains, which are relatively tilted by 26.6 degrees. The inset shows the Fourier transform of the image and reveals the two sets of hexagonal patterns from two individual grains. After removing one hexagonal pattern set and performing inverse Fourier transforms, we easily distinguish the distinct graphene grains (Figs. 4.4b-c). In Fig. 4.4b, the contrast of the right side of the image completely disappears, indicating the graphene has no defects inside the grain.

The zoomed-in image of Fig. 4.4d reveals the detailed atomic structure of a high-angle GB of graphene. Pentagons, hexagons, and heptagons, defined by individual carbon atom positions, are overlaid with red, black, and blue polygons, respectively. It is clear that this high-angle GB consists of an array of alternating pentagons and heptagons without other defect structures such as vacancies, similar to theoretical predictions of graphene high-angle GBs [60, 76, 77]. The pentagon-heptagon GB is fairly stable under the electron beam, proving its mechanical integrity. The GB exhibits a mixture of different types of dislocations with Burgers vectors of (1,0) and (1,1) [60, 76, 77]. The GB also shows local bending at the atomic scale; the majorities of GB segments are found to deviate from the symmetric bisecting line, a result not accounted for in simple theoretical models [60, 76, 77]. Of course, details of the GB structure may be sensitive to graphene synthesis conditions. Figure 4.5 shows additional atomic resolution TEM images of another high-angle tilt grain boundary of graphene. The tilted grains at the left and right sides are relatively rotated by 28 degrees.

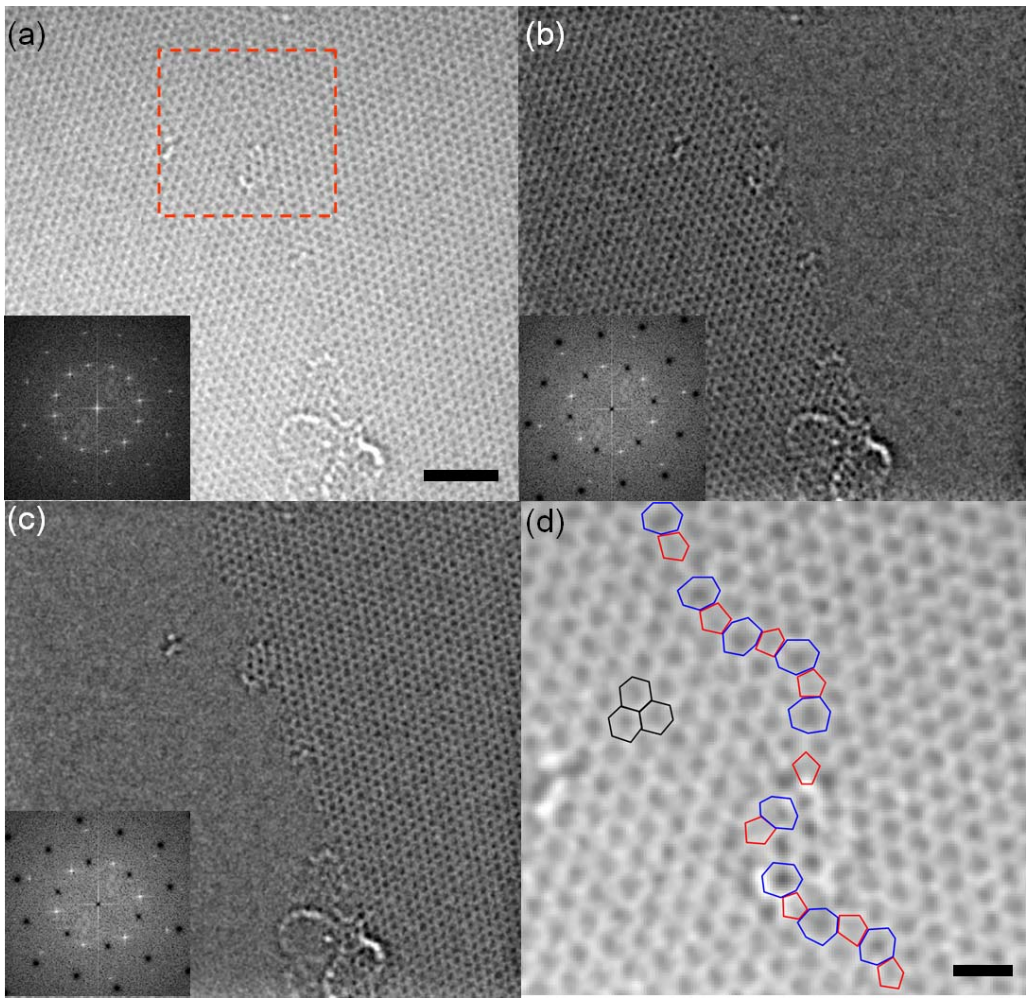

Figure 4.4 Atomic resolution images of a high-angle tilt GB of graphene. (a) Atomic resolution image of graphene GB. The left and right parts of the image are different tilt grains, which are relatively tilted by 26.6 degrees. The red dashed rectangle is the field of view for Fig. d. The inset shows the Fourier transform of the image. It shows the two sets of hexagonal patterns from two grains. The scale bar is 2 nm. (b) Atomic resolution image of the same region after removing one set of hexagonal patterns from the fast Fourier transform. The contrast of the right side of the image completely disappears indicating the graphene has no defects inside the right side grain. (c) Atomic resolution image after removing another set of hexagonal patterns from the fast Fourier transform. The left side of the image disappears. (d) The zoom-in image of the high-angle tilt GB of graphene. The pentagon, hexagon, and heptagon are overlaid with red, black, and blue polygons, respectively. The GB shows an array of alternating pentagon and heptagon structures. The scale bar is 0.5 nm.

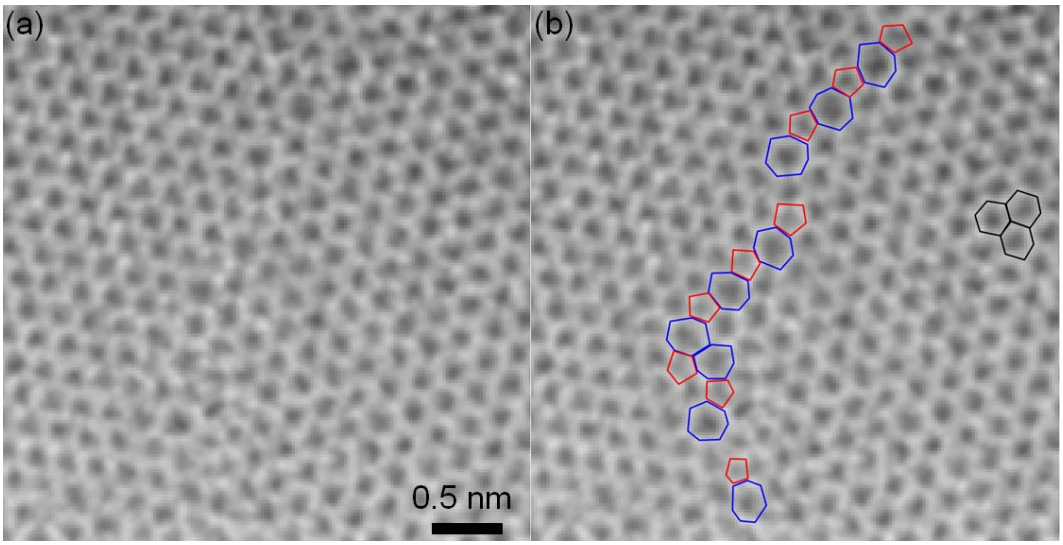

Figure 4.5 Additional atomic resolution TEM images of a high-angle tilt grain boundary of graphene. The tilted grains at the left and right sides are relatively rotated by 28 degrees. (a) Original TEM image. (b) TEM image with atomic configurations (overlaid polygons). The pentagon, hexagon, and heptagon are overlaid with red, black, and blue polygons, respectively.

In conclusion, we present a study of tilt GBs of large-area monolayer polycrystalline graphene using complementary TEM techniques. Conventional-resolution TEM yields structural identification of grains and their boundaries in suspended graphene samples if SED-STEM or DF-TEM modes are employed. The presented methods can readily be used to assess the quality of polycrystalline graphene samples and aid in engineering GBs to exploit their peculiar electronic properties [61]. Moreover, we present the atomic resolution imaging of high-angle tilt GBs in graphene membranes. Our findings will likely benefit future theoretical and experimental studies on thin membrane grains and GBs, including boundary diffusion, electronic structure modification, and possible enhanced chemical reactivity at the boundary.

Chapter 5
Multiply folded graphene: Grafold

Folding a structure changes its form and functionality. From paper origami to the coiling of proteins, folding can transform relatively simple structures into complex shapes with new and distinct physical qualities [78-80]. Graphene has a high in-plane Young's modulus [12] but is easily warped in the out-of-plane direction, similar to a sheet of paper. Although folding induces strain energy at the curved folding edge, it can lower the total energy of the system through plane-plane interactions after folding [81].

The folding may also induce new and distinct properties in graphene. For example, recent theoretical studies suggest that folded graphene can exhibit interesting electronic properties under magnetic fields [82, 83], such as interferometric effects due to the interplay between the gauge fields created by the fold and the external fields. Folds in the top layers of graphite [84, 85] and edge-folds in suspended graphene [17, 86-89] have been previously observed. Most of these studies have focused on the single fold structure; however, graphene folding structures can be more complex and intriguing.

In this chapter, multiply folded structures in graphene are introduced, which we term grafold. Multiply folded structures, such as monolayer / triple-layer / monolayer graphene junctions, are observed in suspended and supported graphene samples and verified by various characterization techniques including transmission electron microscopy (TEM). Using pseudopotential-density functional theory calculations, we show that double-folding alters the electronic band structure of graphene. By introducing anisotropic surface curvature during the graphene synthesis or transfer processes, we also demonstrate ways to control the orientation and placement of graphene folding formations. In principle, single or periodic grafold hems, pleats, creases, ripples, and ruffles can be tailored from graphene. Furthermore, we show that grafolds can serve as a localized intercalation platform via C_{60} intercalation into an edge fold. Intercalation or functionalization of the chemically reactive folds will further expand grafold's mechanical, chemical, optical, and electronic diversity.

The folding of graphene is not as simple as the folding of a sheet of paper, a macroscopically isotropic material without preference for folding axes. In graphene folding one must define the direction and location of folding lines in a way that accounts for the hexagonal lattice symmetry and registry (or lack thereof) between adjacent layers in the fold. As shown in Figure 5.1a, the direction of folding lines (dotted blue lines), θ, can be defined relative to the $\vec{a}_1 - \vec{a}_2$ direction (dotted red lines), where $\vec{a}_1$ and $\vec{a}_2$ are conventional translational unit vectors in the graphene lattice. Unless θ satisfies the equation, $\theta / 30^o = l$ where l is an integer, folding will introduce a relative rotation between the resulting stacked graphene layers. Depending on the direction or location of folding line formations, certain directions of folding may be more energetically favorable than others [84, 89].

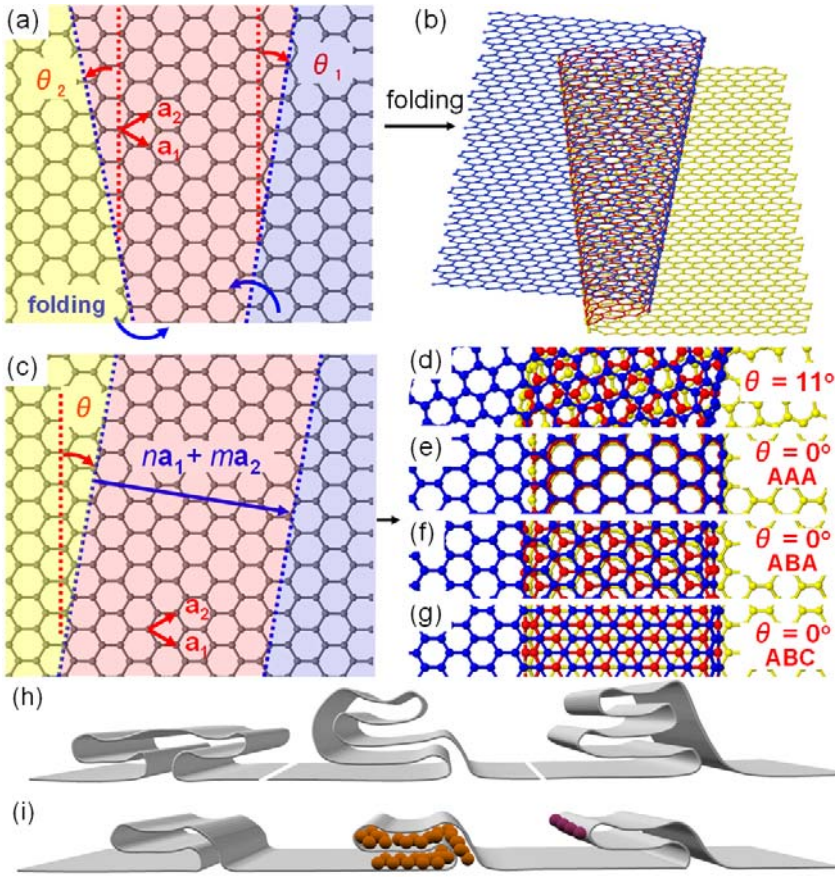

Figure 5.1 Various multiple folding structures of graphene. (a) Planar figure of graphene before double-folding. The dotted blue lines are folding lines, whose directions are measured relative to the direction of the $\vec{a}_1 - \vec{a}_2$ vector in the graphene lattice. (b) Double-folding of single layer graphene produces local triple-layer graphene. Upper, middle, and bottom graphene layers are shown in blue, red, and yellow, respectively. (c) A planar view of graphene before parallel double-folding (pleat folding). The translational vector between the two folding lines can be indexed as $n\vec{a}_1 + m\vec{a}_2$. (d) Top view of a folding structure with $\theta = 11^o$. Top and bottom graphene layers have the same rotational direction. (e-g) Top views of folding structures with $\theta = 0^o$, where foldings occur along the zigzag lattice direction of graphene. The layer stacking can vary depending on where the folding lines occur. (e) AAA stacking of the folding structure with $n = m = 4$ and 1/2. (f) ABA stacking with $n = m = 4$ and 1/2. (g) ABC stacking with $n = m = 4$ and 2/3. (h) Various complex folding structures with quadruple-foldings, including a box-pleat (left). (i) Periodic double folding superstructure. Folds can be used as a local intercalation platform, and highly curved edges can be functionalized with foreign materials.

By repeating a simple folding operation in close proximity to the first fold, one can produce a variety of locally distressed and topologically altered regions, such as a monolayer / triple-layer / monolayer graphene junction. Fig. 5.1a shows a planar view of graphene before double folding, where the two blue dotted lines are the symmetry axes of the fold. An example of one possible structure is shown in Fig. 1b, where the two folding lines have different directions ($\theta_1 \neq \theta_2$). As the two folding lines are not parallel, they will eventually

converge. Borrowing the language of the textile industry, we term this folding structure a tapered tuck [90].

When the double folding lines are parallel ($\theta_1 = \theta_2$), the width of the trilayer region is uniform along the fold and given by $w = a\sqrt{n^2 + nm + m^2}$, where $\vec{w} = n\vec{a}_1 + m\vec{a}_2$ is the translational vector between the two folding lines (Fig. 5.1c). (Note that *n* and *m* need not be integers.) We refer to this parallel double folding structure as regular pleat folding, again referencing the analogous structure in fabrics [90]. In pleat folding, the top (blue) and bottom (yellow) graphene layers have the same crystalline direction, but the middle graphene layer (red) is rotated relatively to the top and bottom layers when $\theta / 30^o \neq l$ (an integer). Fig. 1d shows the top-view of a pleat folding structure where $\theta = 11^o$. Alternatively, pleat folding formations along the zigzag or armchair directions of the graphene lattice ($\theta / 30^o = l$) can produce triple graphene layers in the folding structures with no relative rotation. However, even without relative rotation, there are several distinct stacking configurations possible, determined by the precise positions of folding line formations. Figs. 1e-g show AAA, ABA, and ABC stacking when $\theta = 0^o$.

Using a pleat folding as a building block, we can construct many complex folding structures in graphene. Some possible folding structures with quadruple foldings are shown in Fig. 5.1h. We can also envision a superlattice of pleat foldings in graphene as illustrated in Fig. 5.1h and 5.1i. This novel superlattice may exhibit unique electronic and optical properties distinct from planar single or multi-layer graphene with homogeneous layers, as discussed in more detail below. Moreover, the nature of the non-homogeneous layer number and highly curved folding edges in grafold can be further manipulated. The localized triple layer regions can serve as an ideal localized intercalation platform for encapsulating foreign atoms and molecules. This is a new system which cannot be realized with standard graphite intercalation approaches [91]. Further, highly curved folding edges should exhibit enhanced chemical reactivity from the flat graphene regions [92] and can be used for one-dimensional functionalization of graphene. Local grafold intercalation and edge functionalization are shown in Fig. 5.1i.

5.1 Basic characterizations of graphene folds

We now turn to the experimental observation of grafold. Fig. 5.2a shows a TEM image of graphene transferred onto a Quantifoil holey carbon TEM grid. In the middle of the suspended graphene region there appear long vertical parallel lines. Such ribbon-shaped features are frequently seen in our CVD-grown samples. We find that the usual widths of these features range from a few nanometers to several hundred nanometers, with lengths often extending tens of microns. Folded edge lines in the proposed folding structures in Figure 5.1 will produce line contrasts in TEM images similar to those seen for the "walls" of carbon nanotubes [93]. A scanning TEM (STEM) image shows that central portions (the triple layer) of the fold exhibit higher intensities, indicating that it is thicker than the surrounding monolayer regions (Figure 5.2b). Residual particles preferentially decorate folding structures, implying that the particles are trapped inside the folding, or preferentially adhere around the folding edges during sample preparation as expected for the enhanced chemical reactivity of highly-curved graphene.

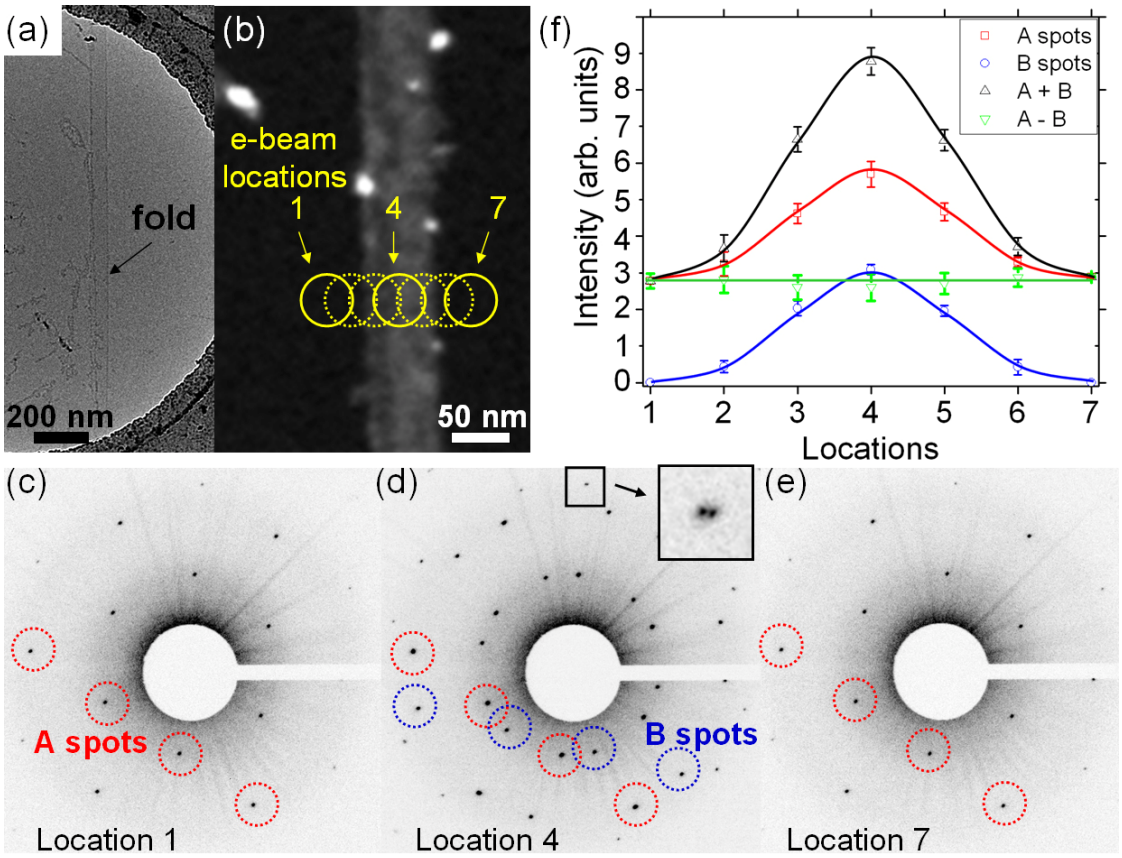

Figure 5.2 TEM and diffraction analysis of double folding structures. (a) TEM image of a ribbon-like folding structure in suspended graphene. (b) HAADF (High-angle annular dark field) STEM image of a graphene sheet with a folding structure. Circles denote different locations 1-7 for diffraction acquisition using a nano-parallel electron beam (NPEB). The NPEP has a diameter of 45 nm. (c-e) Series of diffraction patterns across the folding structure. (c) Diffraction pattern at location 1. (d) Diffraction pattern at location 4, at the folding. Inset shows a zoom-in image of the (0-220) A spot, which shows the splitting of two spots with a very small rotation angle of 0.4°. (e) Diffraction pattern at the location 7. (f) Diffraction spot intensity (A spot, B spot, their sum, and their difference) variations at different locations.

To confirm that the ribbon-like structures of Figures 5.2b are indeed a local triple-layer fold, we perform diffraction scanning across the folding structures using a nano parallel electron beam (NPEB). While scanning NPEB across the folding from locations 1 to 7 (Fig. 5.2b), we acquire diffraction patterns and monitor the transition across the fold. In location 1, which is outside of the fold, we observe one set of hexagonal diffraction spots (A spots) as shown in Fig. 5.2c. By comparing the (0-110) and (1-210) spot intensity, we confirm that this region is composed of monolayer graphene [17, 94]. As we move the electron beam onto the fold structure, we find that another set of hexagonal spots (B spots) appears in the diffraction pattern, originating from the middle layer of folded graphene (Fig. 5.2d). The intensity of A spots inside the fold structure is twice that seen in monolayer regions, and a closer look at the (0-220) A spot reveals two distinct diffraction spots (0.4° rotation mismatch). This indicates that the diffraction pattern is comprised of three sets of hexagonal spots, and confirms that the folded region is a triple layer of graphene. We also note that the small angle splitting in the A

spots is consistent with our observation that the two folding lines appear to be parallel in the STEM image. Figure 5.2f shows the variation of the diffraction spot intensity across the fold from locations 1 to 7. We observe that the intensity sum of A and B spots is a factor of three larger in folded regions than in monolayer regions, again consistent with our picture of a local triple-layer.

We can also easily identify grafolds with scanning electron microscopy (SEM) and atomic force microscopy (AFM). To do so, we transfer CVD graphene to a silicon oxide/silicon substrate. In the SEM image of Fig. 5.3a, we see dark line features across the graphene sample. The low-magnification STEM image of suspended CVD graphene shows that grafolds exhibit similar line features (Fig. 5.3b), which suggests that the dark lines in Fig. 5.3a are folds in graphene samples. When we perform the AFM scan on such dark lines, we observe a very similar ribbon-like feature as previously observed in the TEM study (Fig. 5.3c). Atomic force microscopy (AFM) images are aquired with an MFP3D scanning probe microscope (Asylum Research instruments) in non-contact mode. Moreover, the sample indeed shows the higher height profile (~ 1 nm) inside the line (Fig. 5.3d). All these observations confirm that SEM can be used to identify folds in graphene. We also encounter more complex fold structures in graphene. Fig. 5.3e shows a quadruple fold structure in CVD graphene and the height difference (~ 0.7 nm) of observed steps is consistent with the thickness of double layer graphene.

5.2 Atomic resolution TEM imaging of folds in graphene

For a double-folded graphene, which has two independent choices of folding axes, the two fold lines can be non-parallel ($\theta_1 \neq \theta_2$). In this case, all three layers can be relatively rotated from one another. Figure 5.4 shows an atomic resolution TEM image of such a double fold with non-parallel fold lines. As a result of such non-parallel double folding, the fast Fourier transform (FFT) of the atomic resolution TEM image shows three distinct sets of hexagonal patterns (marked by blue, red, and yellow arrows in Fig. 5.4b) from the three relatively misoriented layers. Between the two fold lines, graphene exhibits a moiré pattern arising from the rotational stacking in multilayer graphene [86], while we find single layer graphene outside of the folding lines.

Moreover, we can further process the FFT signal to visualize the individual layers within the double fold structure in real space. Figures 5.4d-f show reconstructed images of the double fold, which selectively shows each layer in the double fold structure. To obtain Fig. 5.4d, we remove the hexagonal pattern signals marked by blue and yellow arrows, and perform an inverse Fourier transform using only the hexagonal pattern marked by red arrows. After this processing, the single-layer-like graphene lattice signal coming from the middle layer of the double fold structure is clearly visible in real space (Fig. 5.4d). For Fig. 5.4e and 5.4f, we perform the same procedure and successfully reconstruct the top and bottom graphene layers (each separately) by selecting out the hexagonal pattern signals marked by blue (Fig. 5.4e) and yellow (Fig. 5.4f) arrows.

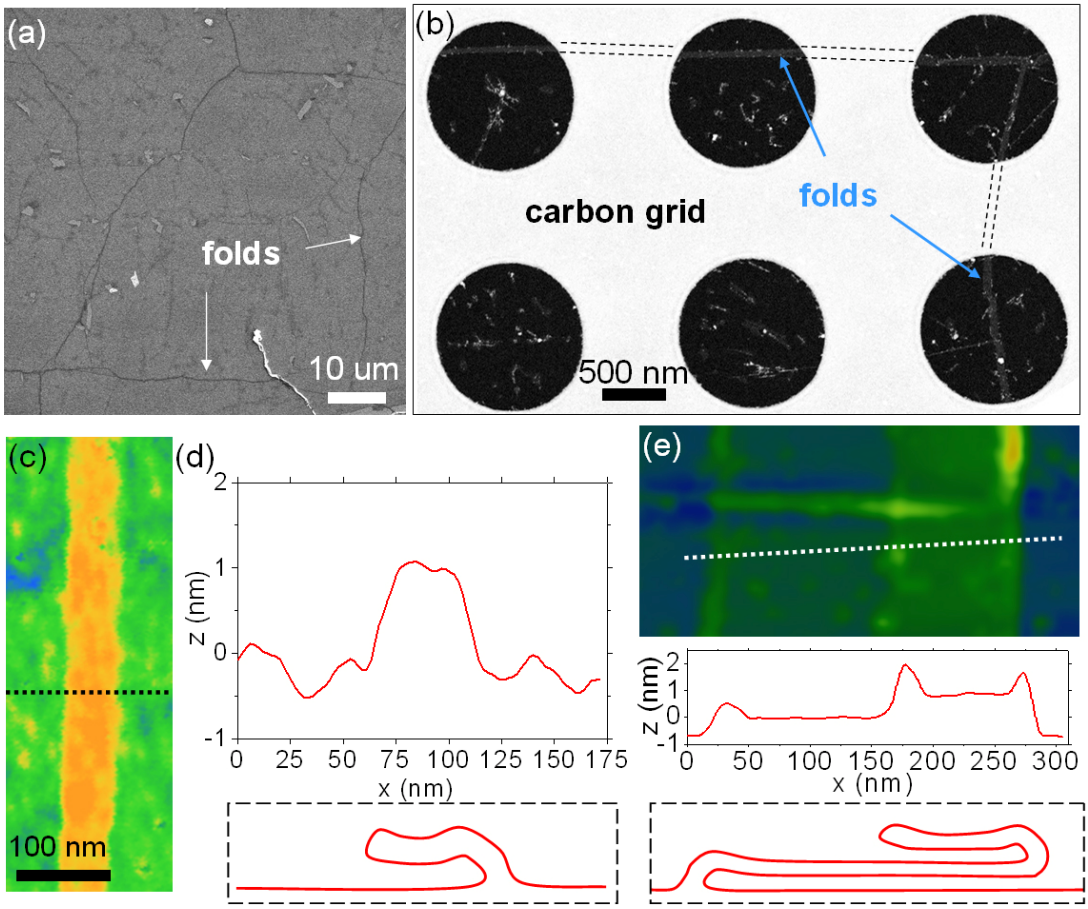

Figure 5.3 SEM, AFM, and STEM images of folds in CVD graphene. (a) SEM images of CVD graphene transfered to a silicon oxide/silicon substrate. Folds appear dark relative to monolayer graphene. (b) HAADF STEM image of CVD graphene transfered to a Quantifoil holey carbon TEM grid. The white background is the region of the amorphous carbon film and the dashed lines are a guide to the eyes for folds in graphene. (c) AFM scan of graphene fold in CVD graphene transfered to silicon oxide/silicon substrate. (d) Top - The height profile of the folding structure along the dotted line in Fig c. Bottom - Proposed folding structure (double folding) from the AFM data. (e) Top - AFM scan of multiple folding structure in graphene. The white dotted line is used for the height profile scan. Middle - The height profile of the folding structure. The height difference (0.7 nm) of observed steps is consistent with the thickness of double layer graphene. Bottom - Proposed folding structure (quadruple folding) from the AFM data.

Double folds can also occur in which the folds are parallel ($\theta_1 = \theta_2$). Borrowing textile industry terminology, we have previously termed these pleat folding structures [90]. In these structures, the top and bottom graphene layer will have the same rotation angle. Fig. 5.5a shows a rotated atomic resolution TEM image of a pleat folding structure around one folding edge. We have rotated the image to apply the previous angle assignment scheme. As expected, the folding edge line shows a very straight line feature in the TEM image, where the triple layer and single layer graphene are located in the left and right side of the folding edge, respectively. Its FFT exhibits two sets of hexagonal patterns instead of three sets (Fig. 5.5b) because top and bottom layers are aligned with each other but not with the middle graphene

layer in the pleat foldings. Such sets of hexagonal patterns are marked with red and blue circles in Fig. 5.5b.

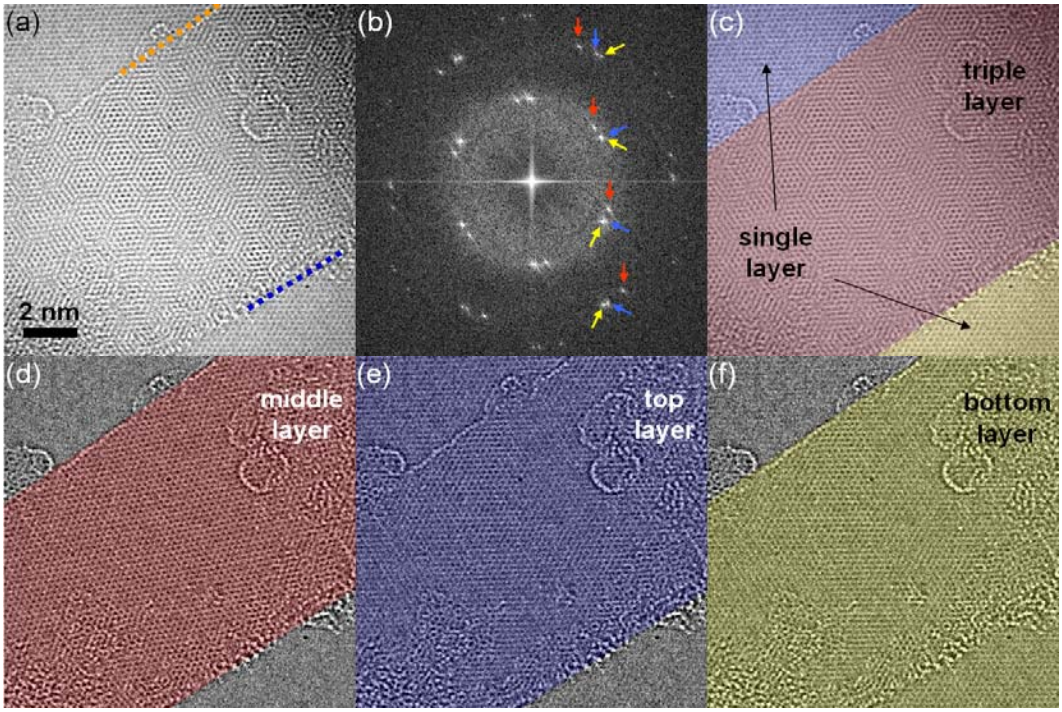

Figure 5.4 Direct visualization of individual layers in a double fold. (a) Atomic-resolution TEM image of a double fold structure in graphene with non-parallel folding edge lines. The folding edges are overlaid with dotted lines. (b) FFT of Fig. 2a showing three different hexagonal sets originating from double folding. The hexagonal sets marked by blue, red, and yellow arrows originate from the top, middle, and bottom layers in the triple layer region, respectively. (c) Color-coded image of Fig. 2a. The areas occupied by top, middle, and bottom layers are overlaid with blue, red and yellow, respectively. (d) Filtered image showing only the middle layer. From Fig. 2b, hexagonal pattern signals marked by blue and yellow arrows are removed and red signal is solely used for reconstruction. (e) Filtered image showing the top layer (with blue signal). (f) Filtered imaging showing the bottom layer (with yellow signal).

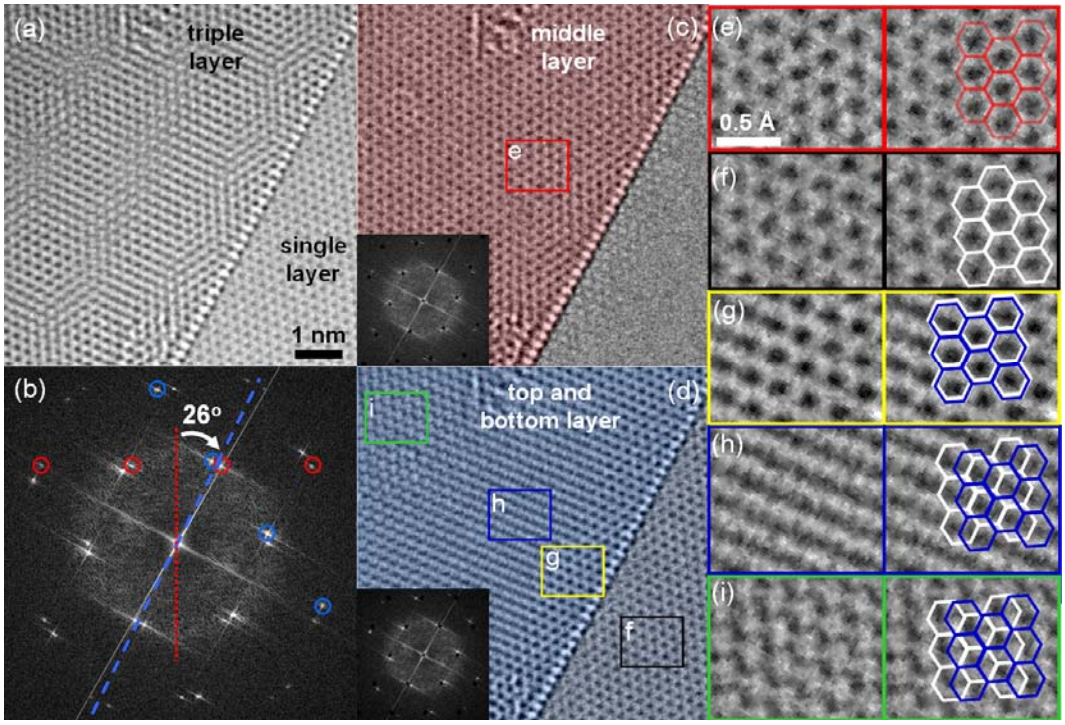

Figure 5.5 Rotated atomic resolution TEM image of a double (pleat) fold with parallel folding. (a) Atomic resolution TEM image of a pleat folding with $\theta = 26^o$. The image shows one of the two pleat fold edges. (b) FFT of Fig. 3a shows two different hexagonal sets of diffraction patterns originating from pleat folding. The hexagonal set marked by horizontal red circles originates from the middle layer in the triple layer region. The blue dashed line is drawn as parallel to the folding edges in the Fig. 3a. Note that the figures are rotated for the proper angle assignment. (c) Filtered image of Fig. 3a using the only the hexagonal pattern from the middle layer signal (marked by red in Fig. 3b). (d) Filtered image of Fig. 3a using only the hexagonal pattern from the top and bottom layer signal (marked by blue in Fig. 3b). (e) Zoom-in image of rectangle in Fig. 3c. (f-i) Zoom-in images of rectangles in Fig. 3d. Right side images are shown with corresponding local atomic registry.

The previously described reconstruction process for individual layer visualization can also be used for pleat folds. Fig. 5.5c and 5.5d show the filtered images using the hexagonal patterns marked by red and blue circles, respectively. The FFT signal marked with red circles contributes to the sandwiched middle layers. To apply the angle assignment scheme, we also have rotated the TEM image so that the $\vec{a}_1 - \vec{a}_2$ vector in the sandwiched middle graphene layer is aligned vertically as shown in Fig. 5.1a. By this image rotation, we imagine a structure wherein top and bottom graphene layers are relatively rotated to the reference middle layer after folding. The FFT of the image can be used to check this process; the hexagonal pattern (marked by red circles), which originates from the middle layer graphene, should be aligned horizontally in the FFT as shown in Fig. 5.5b. After the TEM image rotation, we can directly measure the deviation angle of the fold axis (blue dashed line) from the referenced vertical direction (red dotted line). This gives us a direct measurement of $\theta = 26^o$ for the fold angles. The zoom-in image of lattice structure in the middle layer also

shows the expected aligned lattice direction (Fig. 5.5e). The imaging condition employed produces the bright atom contrast and the graphene lattice structure is overlaid in the right side of the Fig. 5.5e.

With a pleat fold, the signals from the top and bottom layers are closely overlapped in the frequency domain and cannot be decoupled from each other via the aforementioned image filtering process. Instead, interference effects between top and bottom layers will be apparent. Fig. 5.5d shows the reconstructed image from the top and bottom graphene layers. Interestingly, in the different regions of the overlapped structure, we observe distinct lattice contrast patterns (Fig. 5.5f-h) due to different local stacking relations. For example, in Fig. 5.5f, the image contrast is nearly doubled while maintaining the single-layer contrast pattern. This corresponds to local AA stacking, where the atomic positions in two layers are exactly overlapped, doubling the image signal. On the other hand, Fig. 5.5g shows a highly distorted pattern, exhibiting line patterns rather than the hexagonal patterns. This is due to intermediate stacking where the local atomic registry produces streaked atomic positions. The other region displays the graphene lattice pattern but the bright-dark contrast is reversed as shown in Fig. 5.5h. With our imaging conditions, the AB stacking of graphene lattice can give us such a reversed contrast [73]. Therefore, we confirm that there is a smooth transition from AA to AB stacking between top and bottom layers in different regions of a pleat fold. Fig. 5.6a shows another atomic resolution TEM image of a pleat folding structure with parallel folding edge lines ($\theta = 27^o$).

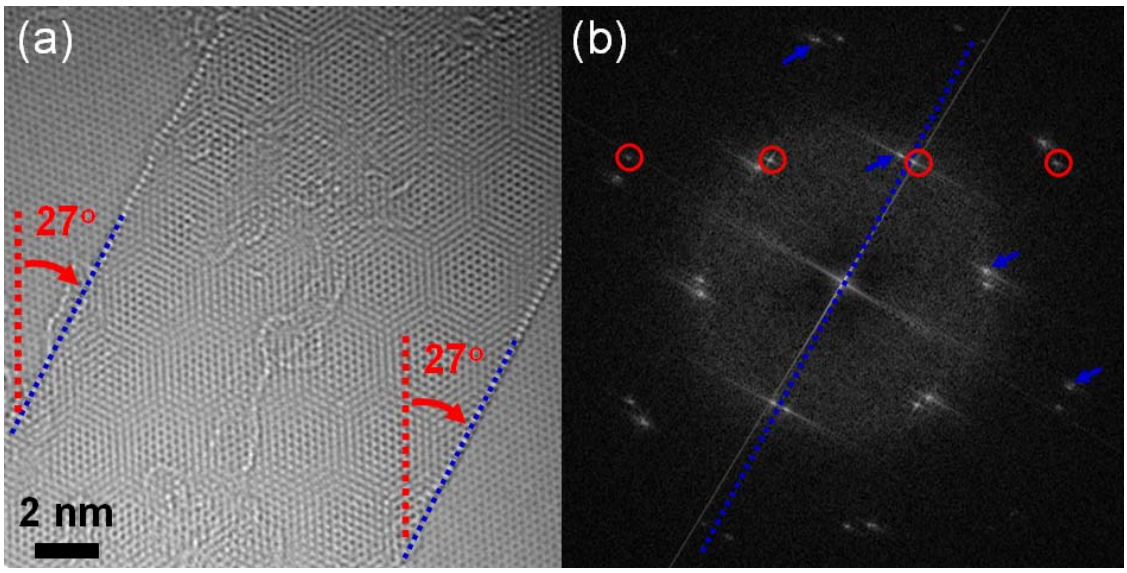

Figure 5.6 Atomic resolution TEM image of a pleat folding structure. (a) A double folding structure with parallel folding lines with $\theta = 27^o$. To the left and right of the folding structure is monolayer graphene. The folding edges are overlaid with blue dotted lines. (b) Fast Fourier transform (FFT) of Figure 4a, which shows two sets of hexagonal patterns. The circled set of hexagonal pattern (red) is from middle layers. The blue dotted line is drawn to be parallel to the folding lines. The hexagonal set marked by blue arrows is from top and bottom graphene layers, which have the same lattice directions after folding.

We have analyzed approximately 50 double fold structures to better understand the fold formations and investigate the angle dependence in folding. Fig. 5.7 shows that the number of double fold structures with a significant difference between two fold angles is quite small; the majority of angle differences is less than 1 degree. This shows that the two fold angles are not independent during the double folding formation. Instead, the two fold lines tend to align with each other since a large mismatch in the two fold angle will induce significant deformation and highly strained singular points as the two folding lines converge. Parallel double folds need not suffer from the energy cost associated with this singularity. We note that the observed parallel folding is closely related to the theory of a developable surface, a surface that can be unrolled onto a flat plane without tearing or stretching [95].

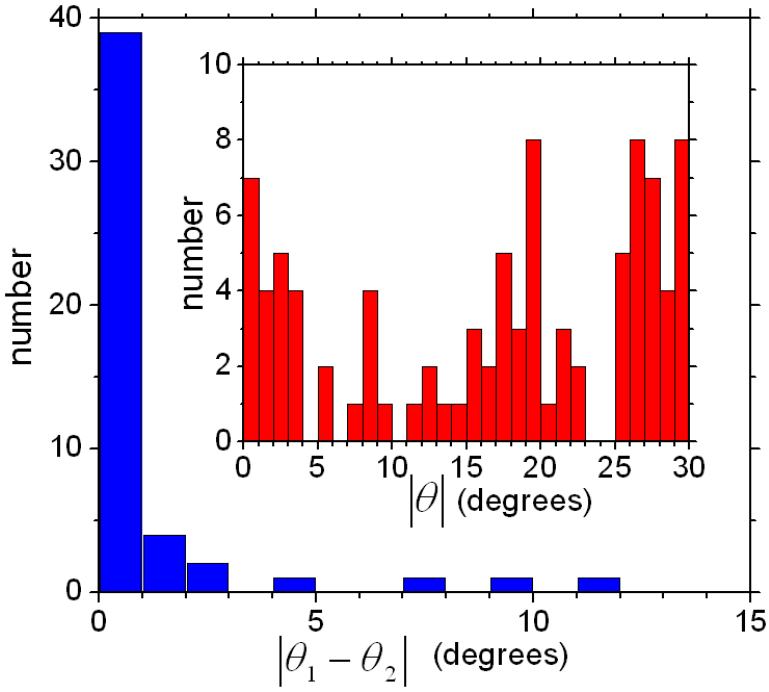

Figure 5.7 Angle dependence of folding axis in double folds. Histogram of angle difference between two folding axes in double fold structures of graphene. The fold angle difference is smaller than 1 degree for most of the observed double folding structures. Inset shows a histogram of observed fold angles ($0 \le |\theta| \le 30^o$) in the double fold with respect to the graphene lattice direction. Each fold in double fold structures is counted.

The inset of Fig. 5.7 shows that the fold formations occur in quite random directions relative to the graphene crystalline orientation. Previously, it has been observed that folding at the *free* edges of graphene predominantly occur in the zigzag ($\theta = 0^o$) and armchair ($\theta = 30^o$) directions with mechanical agitation, due to lattice registry effects [89]. Random directions of double fold formations imply that the interlayer energy difference in different stackings is not the dominant factor in our double fold cases. The fact that the folds are *within*

the sheet of graphene, not around the free edges, may play an important role since it provides more constraints on the fold formations. In the case of free edge folding, it is relatively easy to readjust the angles and locations of fold, especially small folded regions. The polycrystalline nature of CVD graphene also contributes to the random directions in fold formations. The observed grain sizes in CVD graphene, around a few micrometers [94], are smaller than the extended lengths of double folds, usually longer than tens of micrometers. If a double fold is extended through many graphene grains without a significant change of its folding direction, the misorientations between each grain can lead to the relative variations in the angles of fold axis with respect to the graphene crystallographic direction.

Even though the folding axis exhibits a highly random direction with respect to the graphene lattice direction, we sometimes observe a pleat folding with $\theta_1 = \theta_2 = 30^o \cdot n$ (n is integer), a higher symmetry fold case. In this case, all triple layers are in rotational alignment. Fig. 5.8a shows such a case, where the folding line formations occur in the zigzag direction of the graphene lattice ($\theta = 0^o$). The FFT of the image shows only one set of hexagonal patterns, which is evidence for the presence of non-rotated triple layers. Even though there is no relative rotation, the triple layers still can have various stacking relations according to the locations of folding axes. For $\theta = 0^o$ pleat folds, ABA (Bernal stacking), AAA, ABC, and other intermediate stackings can be obtained by small shifts in locations of folding axes. The stacking relations, together with the folding angles, will play important roles in altering the properties of folded graphene from its planar counterpart.

Zoomed-in images in the different regions of the triple layers display very distinct intensity patterns as shown in Fig. 5.8b-d. To properly interpret the local stacking relations in the triple layers, we generate simulation TEM images from the constructed atomic models and compare those images with the experimental observations. We construct atomic models of the graphene fold and perform structural relaxations using the SIESTA code [96] with a double-zeta (DZ) basis set until the forces are smaller than 0.04 eV/Angstrom. Psuedopotentials [97] and density functional theory with the local density approximation [98, 99] are used. The grafold structure is simulated in a periodic supercell of length 8.4 nm in the direction perpendicular to the fold and in the graphene plane, and 2.1 nm perpendicular to the graphene plane. Around the fold edges, a relaxed double fold exhibits bulged structures, which can be thought of as a partial nanotube (Fig. 5.9a). Away from the fold edges, the triple layer region contains a flat region where a proper stacking relation to the other layers can be defined. By varying the initial conditions of constructed models, we can also obtain relaxed structures with different stacking relations in the flat region. In the atomic models shown in Fig. 5.8e and 5.8g, the ABC and ABA-stacking can be found in the flat triple regions of double fold structures.

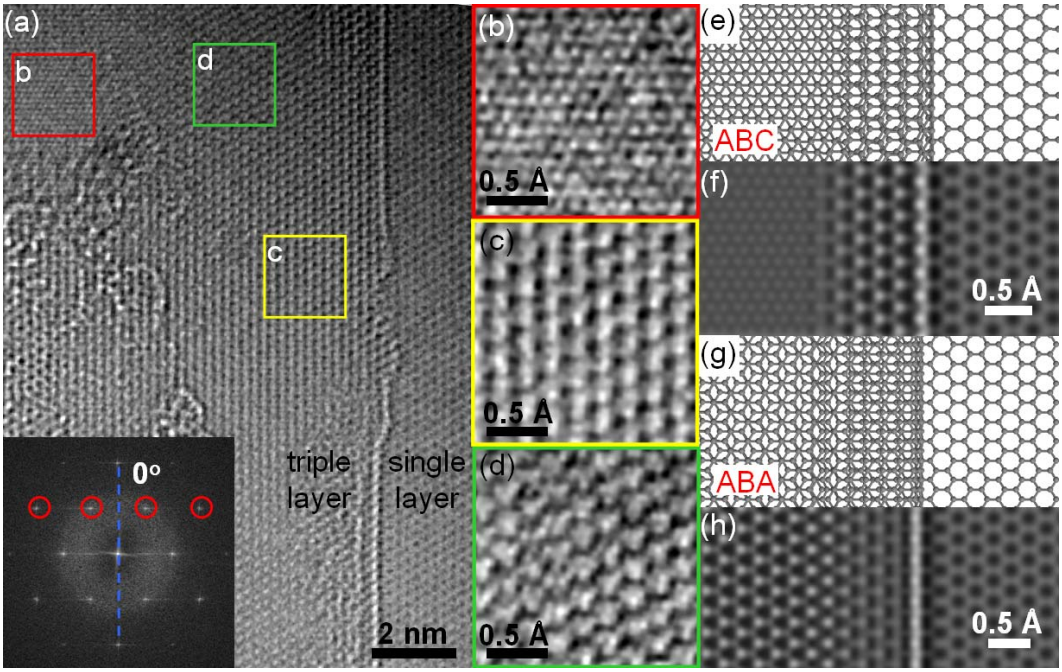

Figure 5.8 Rotated atomic resolution TEM image of parallel double (pleat) folding with $\theta = 0^o$. (a) Atomic resolution TEM image of a pleat folding in the zigzag direction ($\theta = 0^o$). The boxes are the field of view for Fig. 5b, 5c, and 5d. The inset is the FFT of the TEM image, which shows one set of hexagonal spots. (b) Zoomed-in image of the triple-layer region shows the ABC stacking relation. (c) Zoomed-in image with a stacking relation close to ABA stacking. (d) Zoomed-in image with an intermediate stacking relation. (e) Relaxed atomic model of a pleat folding in the zigzag direction $\theta = 0^o$ with ABC stacking at the flat triple layer region. (f) Simulated TEM image from atomic model in Fig. 5e. (g) Relaxed atomic model of a pleat folding in the zigzag direction with ABA stacking at the flat triple layer region. (h) Simulated TEM image from atomic model in Fig. 5g.

From these atomic models, we perform image simulations using MacTempas software with a set of parameters which reflects the experimental conditions. These images are shown in Fig. 5.8f and 5.8h. Around the folded region, the stacking between triple layers is not well-defined and about 1 nm width of image is distorted compared to other flat regions. Beyond these regions, the simulation images exhibit uniform image structures at the flat triple regions. ABC and ABA stacking produce very distinct intensity patterns; ABC stacking particularly produces dominant intensity variation at the half length of the conventional graphene unit cell, 1.23 nm.

We find that the local regions in Fig. 5.8b exhibit the ABC stacking, displaying the expected intensity variation at the half of the graphene unit cell length. On the other hand, the region in Fig. 5.8c shows an intensity pattern very similar to ABA stacking. Interestingly, the local region in Fig. 5.8d exhibits the intermediate stacking relation, deviated from ABC and ABA stacking. This variation of stacking relation means that the triple layers stacked on each other are not parallel but have different local curvature in the out of plane direction.

5.3 Electronic bandstructure calculation

The electrical and optical properties of graphene can be dramatically modified by changing the number and stacking relations of adjacent layers due to inter-layer interactions [5, 100-108]. AB-stacked (Bernal stacked) bilayer and triple-layer graphene have distinct properties from monolayer graphene [5, 100-105]. Non-regular stacking such as rotated two-layer graphene leads to interesting properties such as variable van Hove singularities and renormalization of charge carrier velocity [106-108]. Interesting questions arise upon laterally (in-plane) changing the number of graphene layers; in such situations, charge carriers will experience abrupt band-structure transformations at sites of layer number transitions. Even though there are a few previous theoretical calculations concerning electronic band structures of folded graphene, they have mainly focused on the bilayer graphene systems with single folds [109-111]; complex multiple fold structures with inhomogeneous layer numbers, such as pleat folds, have remained unexamined.

To better understand how folding affects graphene's material properties, we model the pleat folding structure in the supercell approximation [112]. The triple layer region is connected to the outer monolayer graphene by curved graphene regions formed from partial nanotubes. This simple model is then relaxed using the SIESTA code with a double-zeta (DZ) basis set until the forces are smaller than 0.04 eV/Angstrom. The relaxed pleat folding structure ($\theta = 0^o$) originally formed from (8,8) and (13,13) armchair nanotubes is shown in Fig. 5.9a. The length of the unit cell is 8.04 nm in the direction perpendicular to the fold and in the graphene plane, and 2.5 nm perpendicular to the graphene plane.

The geometry of the fold in the relaxed structure is influenced by the interlayer interactions and strain due to the curvature of the fold. In Fig. 5.9a, it is apparent that the relaxed structure has flat regions which transition smoothly to bulges at the edges of the fold. These bulges are similar to those found in collapsed nanotubes [113]. The relaxed structure shows a stacking very similar to the ABC stacking pattern and the width of the folding can be indexed as $n = m = 4$ and 2/3. (see the **Section 5.5 Indexing of a pleat folding structure** for the detailed indexing scheme). However, unlike graphite, the grafold structure has regions of large curvature which necessitates that the layers are no longer parallel to each other. Thus, the registry is changed as the graphene layer gets close to the fold, a result seen in previous studies of the bilayer graphene edge [88].

We calculate the band structure of the grafold system along the direction of the fold as shown in Fig. 5.9b. For a fold along the zigzag direction, the K point in the graphene Brillouin zone maps to $(1/3)(2\pi/a)$ in grafold, which we label as "K" in the figure. The band structure exhibits a semi-metallic character with the pi-states having a small, indirect overlap of ~8 meV near the "K" point. This unconventional electronic band-structure is one example of what can be obtained in grafold nanostructures where many effects are simultaneously in play, such as curvature, interlayer coupling, layer registry, and confinement. Detailed discussions on the effects of the layer registry can be found in the **Section 5.6 Band structures of shifted bilayer graphene**. With narrow grafold structures, we also find that the occupied states in the vicinity of the Fermi level are localized near the folded region. This can be seen in Fig. 5.9c where an isosurface of the local density of states, integrated over occupied states within 0.1 eV of E_F, is shown. This localization may be useful for constructing electronic devices based on grafold nanostructures.

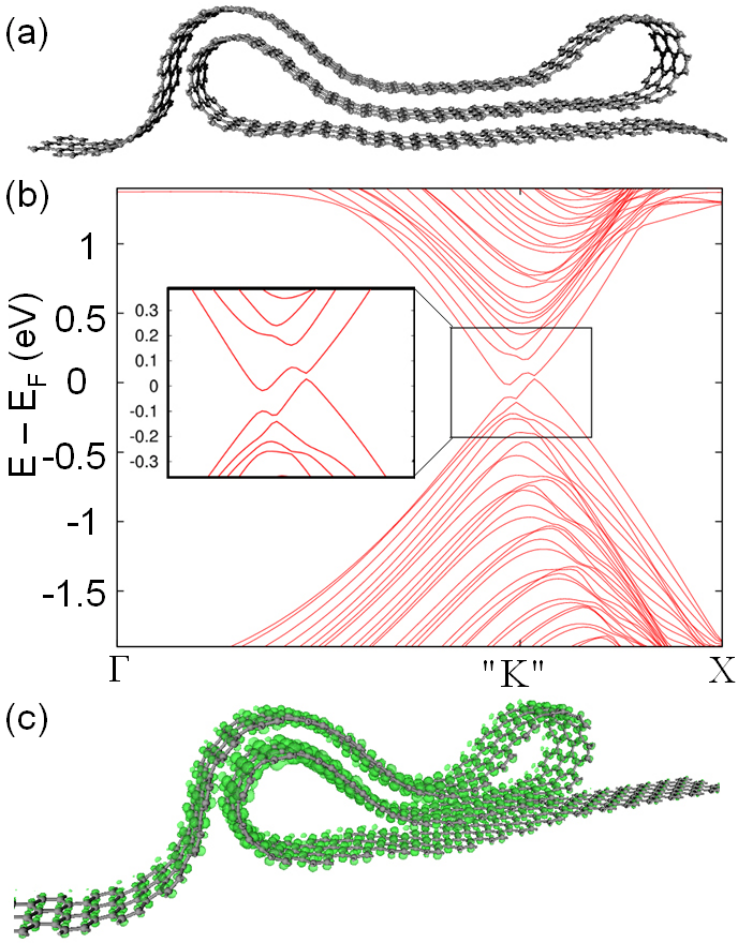

Figure 5.9 Theoretical calculation of double folding structures in graphene. (a) Model of the pleat folding structure of $\theta = 0^o$ that has been relaxed. The fold is periodic into the page, although only a finite width is shown here for clarity. (b) Electronic band structure of the pleat folding along the direction of the fold. The system is semi-metallic with a slight indirect overlap between the occupied and unoccupied states. (c) Calculated local density of states integrated for the occupied states from 0.1 eV below E_F to E_F for a narrow double folding with a triple layer region of length ~ 1 nm. The shown iso-surface is 10% of the maximum value and shows the occupied states near the Fermi level are localized to the region near the fold. The modeling and calculations are mainly performed by Brad D. Malone and Marvin L. Cohen.

5.4 Controlling folds in graphene

The formation of pleat folds occurs spontaneously during chemical vapor deposition (CVD) graphene synthesis or transfer processes. Local wrinkles (or buckling) in graphene naturally form to relieve strain during the cool-down from high-temperature CVD growth temperatures [114, 115], during which the synthesis substrate contracts and the graphene

slightly expands [23, 114, 115]. These wrinkle structures often collapse to form folded structures when the copper substrate is etched away and the graphene is transferred to target substrates. The TEM analysis of the angle dependent folding frequency and the folded area (fold frequency weighted by folding width) shows that folds have a fairly random distribution of orientations (Fig. 5.10a and 5.10b).

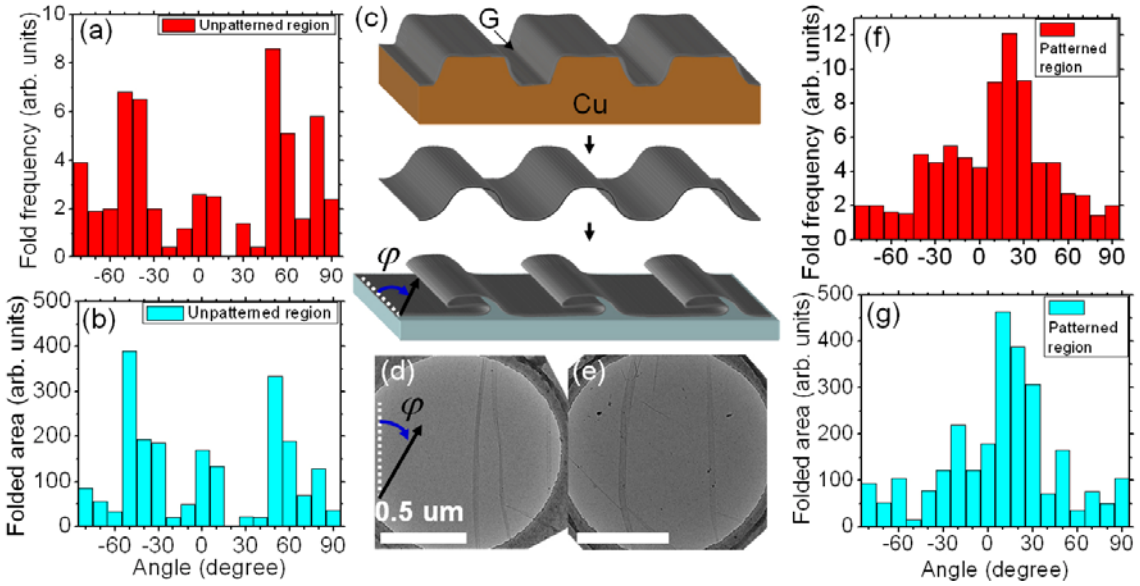

Figure 5.10 Controlled folding formations in graphene: comparison of graphene folding formations from regular and patterned copper substrates. (a) Histogram of angle-dependent fold formation frequency in graphene grown on unpatterned copper foil. (b) Histogram of angle-dependent folded area in folds in graphene grown on unpatterned regular copper foil. (c) Schematic process of directional control of folding formations in graphene during synthesis. A copper substrate with patterned etched trenches is used for CVD graphene growth. After transferring the graphene to other substrates, foldings are more frequently aligned with the patterned direction. (d-e) Graphene synthesized using the patterned copper substrate and transferred to a Quantifoil holey carbon TEM grids. Aligned folding formations are observed. $\varphi = 0^o$ is the pattern direction in the copper substrate. (f-g) Histogram of angle-dependent fold formation frequency and folded area in graphene grown on etched line trenches of copper foil. The angle at zero degrees is the direction of the patterns.

Grafold applications necessitate the ability to control the directions and locations of grafolds. We demonstrate that the directions and placement of folding formations can in fact be controlled by intentionally inducing, and then reconfiguring, surface curvatures in graphene during either the synthesis or transfer process. Fig. 6c shows a route to controlled graphene folding in which we control the preferential folding directions by growing the graphene on a patterned substrate prior to transfer. In this method, a copper substrate with etched line trenches is used for CVD graphene growth. We synthesize graphene on a copper substrate with etched line trenches. We spincoat PMMA on copper foil and pattern parallel lines with electron beam lithography (1 μm or 2 μm width, with 10 μm pitch). Then we partially etch the copper foil with $Na_2S_2O_8$ solution (concentration of 0.1 mg $Na_2S_2O_8$ /1 mL water) for 1.5 minutes. After etching, we remove the PMMA mask with acetone and grow

CVD graphene on the patterned copper foil.

Graphene synthesized using this method and transferred to a Quantifoil holey carbon TEM grid is shown in Fig. 5.10d and 5.10e. Here, $\varphi = 0^o$ is the patterned trench direction in the copper substrate used for graphene synthesis. The histogram of angle-dependent folding frequency shows that the predominant folding formations occur along the trench direction (Fig. 6f and 6g) where a sample area of over 5,000 um^2 was investigated.

We propose another possible route for controlled placement of grafolds. Figure 5.11a shows a schematic of this proposal. After a standard CVD synthesis, graphene is transferred onto a substrate which has patterned metal (for example, Cu) rails or other removable features. The features are then etched away, allowing the local slack in the graphene to collapse and resulting in folding of the graphene at the desired regions. SEM images of graphene on a silicon substrate with a patterned copper rail, before and after the copper etching and graphene folding, are shown in Figures 5.11b and 5.11c, respectively; the observed features and apparent absence of graphene tearing suggest that the new slack results in graphene folding at the desired patterned locations.

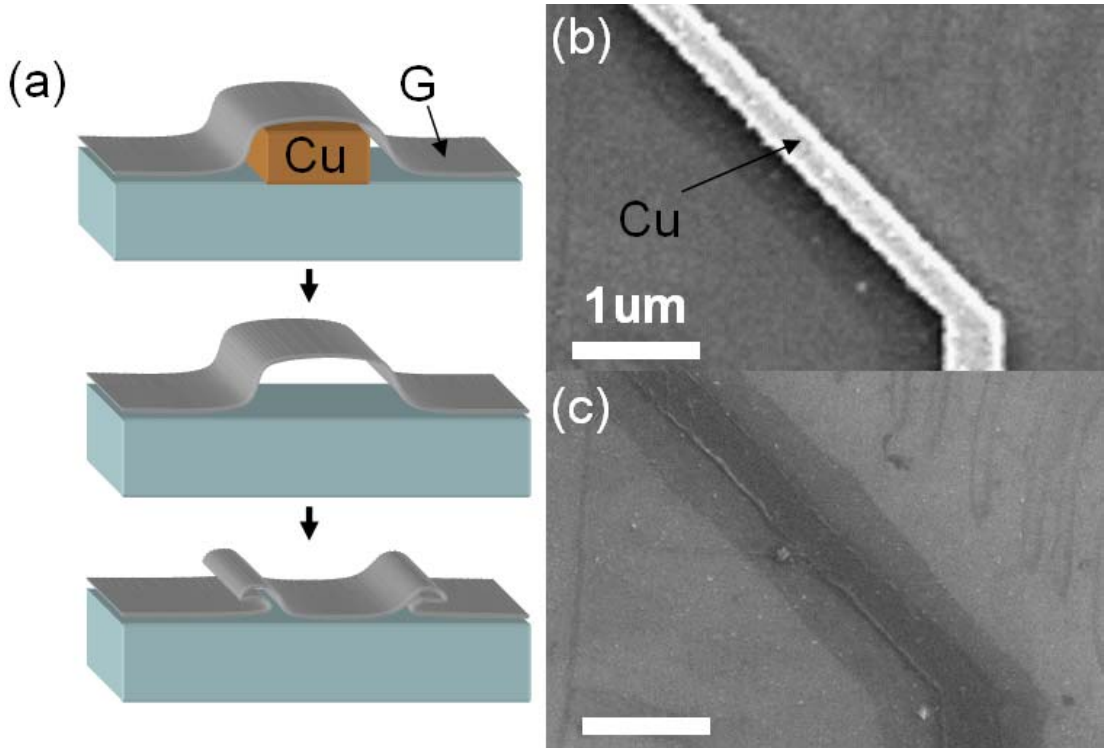

Figure 5.11 Proposal for controlled placement of grafold. (a) Schematic process of controlled placement of folds in graphene. Graphene is transferred onto a substrate which has patterned metal features. After underetching of the metal features, the graphene collapses and may fold along these pre-patterned regions. (b) SEM image of graphene draped over a copper metal pattern on a silicon substrate. (c) SEM image of the same region after the copper is underetched. The image is suggestive of graphene folding aligned with the removed copper structure.

Grafolds can also serve as a localized intercalation platform. To demonstrate this possibility, we intercalate C_{60} into the grafolds. C_{60} has been intercalated into graphite and various nanotubes in prior studies [116-119]. The introduction of C_{60} could potentially induce interesting changes in the system's properties such as electronic band structure modifications [117, 118]. For C_{60} intercalation, graphene-covered TEM grids and ultra-pure C_{60} crystals are placed in a clean quartz ampoule that is then evacuated to 10^{-6} Torr and sealed. The sample is then placed in a furnace at 600 ^{o}C for 7 days. After cooling, the TEM grid is lightly rinsed in isopropyl alcohol and allowed to dry.

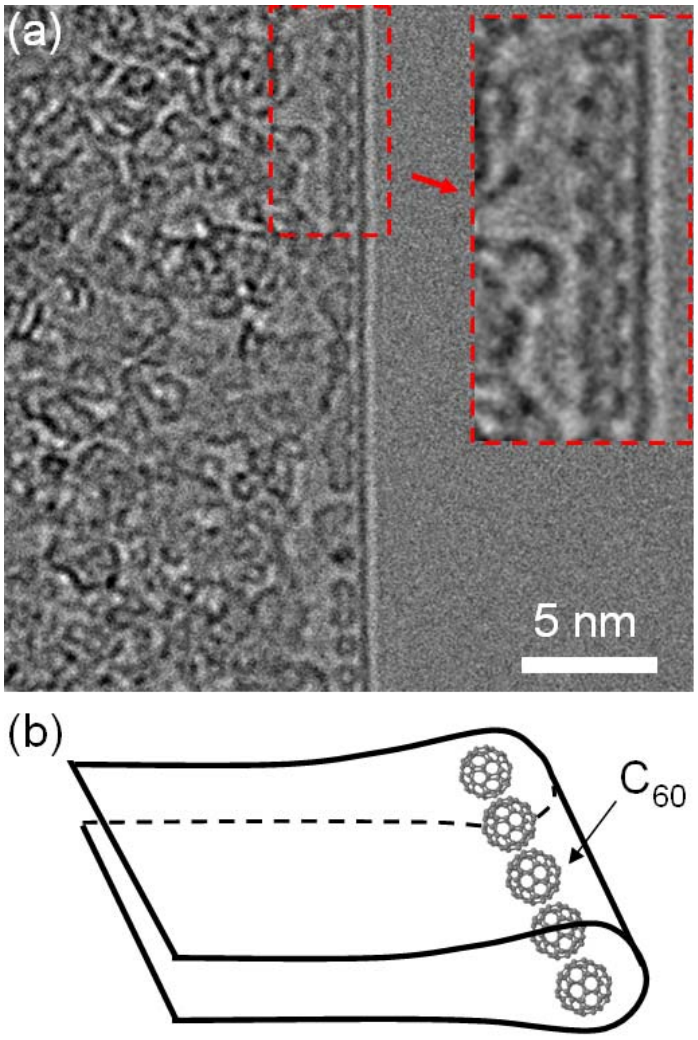

Figure 5.12 Intercalation of C_{60} into a single fold in graphene. (a) TEM image of a graphene edge fold with intercalated C_{60}. Along the straight fold edge, C_{60} are closely packed forming a single chain of C_{60}. (b) Schematic view of the fold structure with local C_{60} intercalation. The TEM image was taken by Benjamin Aleman.

In Fig. 5.12a, we show a TEM image of C_{60} intercalation into a graphene edge fold. Even though the C_{60} are randomly distributed away from the folded edge, we find that the C_{60} are closely packed forming a single chain of C_{60} molecules along the straight folded edge, confirming successful intercalation into the grafold. The C60 intercalation into grafold was mainly conducted by Benjamin Aleman. The available intercalants are essentially unlimited, opening up the possibility of tailoring grafold structures into a wide new class of materials with novel physical properties.

5.5 Indexing of a pleat folding structure

For a pleat folding in graphene, a translational vector between the two folding lines can be assigned as $\vec{w} = n\vec{a}_1 + m\vec{a}_2$. From this vector, the width w and the folding angle θ can be determined.

$$w = a\sqrt{n^2 + nm + m^2} \tag{5.1}$$

$$\theta = \tan^{-1}\left({(n-m)} \Big/ {\sqrt{3}(n+m)} \right) \tag{5.2}$$

However, finite local curvatures at the folded edges (Fig. 9a) may lead to ambiguous assignment of folding lines. Here, we suggest a way to define the folding edge lines to avoid this problem. Figure 9 show the schematic of this process.

First, we define an axis of interest (blue dashed line) in the flat folded region around which the area has a certain well-defined stacking relation as shown in Fig. 5.13a. Any axis of interest chosen inside the flat region can assign unique folding lines (and indexing) for a pleat structure. There are three points of interest which are intersected by the blue dashed line in the three stacked graphene layers. Fig. 5.13b shows the top-view of the folding structure shown in Figure 9a. For the structure shown here, an ABC-stacking relation can be identified in the flat region. The points of interest are marked by the blue dot. Next, we unfold the pleat folding structure to obtain the corresponding flat graphene sheet while tracking the three points of interest as shown in Fig. 5.13c. We can now easily calculate the translational vectors between these three points. The folding edge lines (blue dashed lines in Fig. 5.13c) can be defined as the perpendicular bisectors of the lines connecting the three points of interest. In the pleat folding strcture shown in Fig. 5.13 (also the folding structure in Fig. 5.13a), the indexing is $n = m = 4$ and 2/3. For the case of foldings in the zigzag or armchair directions of graphene lattice ($\theta = 0^o$ or $\theta = 30^o$), the indexing satisfies $n = m$ or $m = 0$, respectively.

5.6 Band structures of shifted bilayer graphene

We perform first-principles calculations for two layers of graphene with different relative shifts along the armchair direction to consider the effects that layer registry has on the electronic structure of the fold (Fig. 5.14). We use the plane-wave pseudopotential method [120] and density functional theory with the local density approximation [98, 99], as implemented in the Quantum-ESPRESSO code [121]. The core-valence interaction is modeled using norm-conserving pseudopotentials [97]. A plane-wave cutoff of 60 Ry is used for the valence wavefunctions. The graphene lattice constant is 2.46 Å and the separation between the layers is fixed at 3.35 Å. The unit cell length perpendicular to the graphene sheets is 15 Å. The Brillouin zone is sampled with a $32 \times 32 \times 1$ Monkhorst-Pack k-point grid, and a Gaussian smearing of 0.05 eV is used for the electronic occupations.

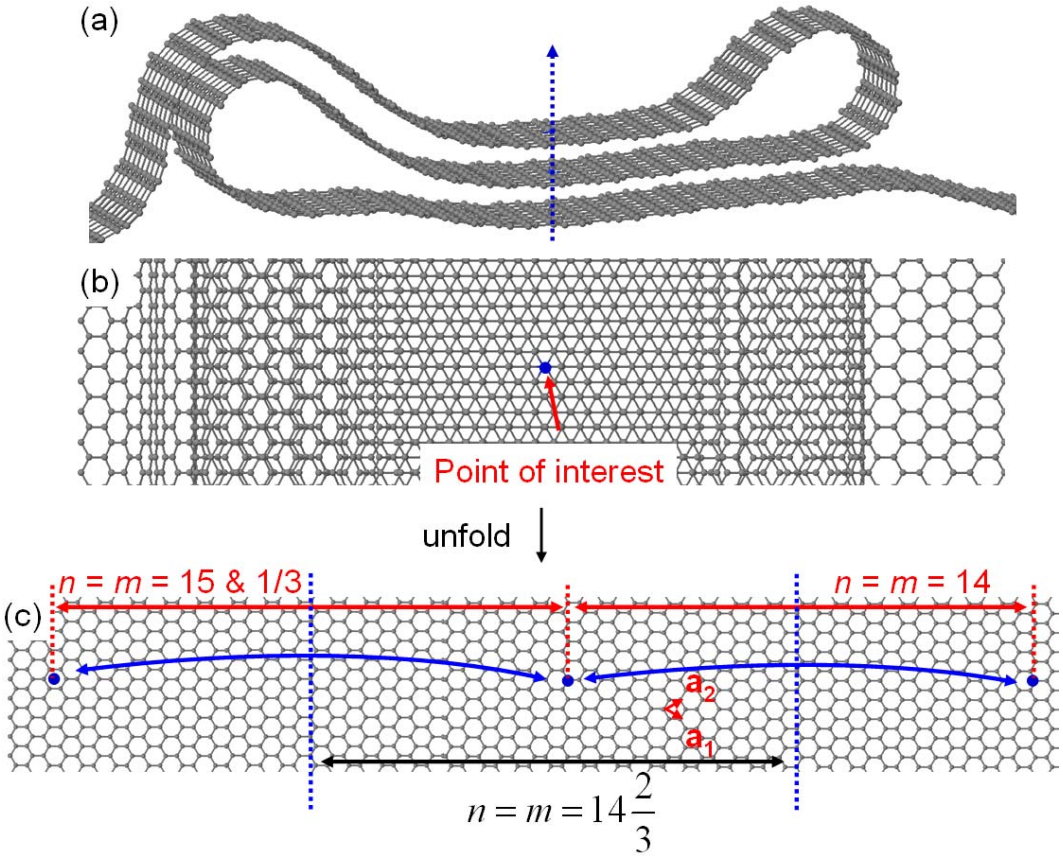

Figure 5.13 Schematic of indexing of a pleat folding structure. (a) Assignment of an axis of interest in the folding structure. There are three points of interest which are intersected by the blue dashed line in the three stacked graphene layers. (b) Top-view of the folding structure shown in Figure 9a. An ABC-stacking relation can be identified in the flat region and the points of interest are marked by the blue dot. (c) Unfolding the structure to obtain a flat graphene sheet and finding the translational vectors connecting the three points of interest to index the folding lines (blue dashed lines). In the folding structure shown in the schematic, the indexing is $n = m = 4$ and 2/3.

As expected, the shift corresponding to AB stacking (Fig. 5.14c) between layers is most energetically favorable. Other configurations a, b, and d in Fig. 5.14 are higher in energy by 14, 6, and 1 meV/atom, respectively. The band structures for these configurations are shown in Fig. 10, Top. In agreement with previous studies [100, 122], the bands near E_F for AB stacking show quadratic dispersion and a small band overlap very close to the K point. For AA stacking, linear bands cross at E_F away from the K point. For a shift intermediate between AA and AB stacking (Fig. 5.14b), the conduction and valence bands show gaps at k-vectors away from the K point along the K-M and K-Γ directions. For another shift (Fig. 5.14d), we find two bands that cross away from K, above E_F, while there is a gap at K and along the K-Γ direction.

These calculations show that a shift in registry (relative translational position) of two

graphene layers can create multiple valence band maxima and conduction band minima near, but shifted away from, the K point. The k-vector positions of these extrema relative to the K point and the band gaps are similar to what we calculate for the grafold structure. A similar effect was found in previous calculations for double-wall carbon nanotubes with shifted rotational orientations [123]. The indirect band overlap seen in the grafold band structure is not seen for two graphene layers, but could come about by other perturbations such as the curvature of the fold.

Although registry shifts away from AB stacking (or ABA or ABC for trilayer graphene) would not be expected for stacked graphene layers, the curved regions in grafold may allow the registry to change along the structure. Indeed, in our calculated grafold structure, the registry is not fixed throughout the fold. Therefore, these shifted registry effects can be present in the grafold band structure.

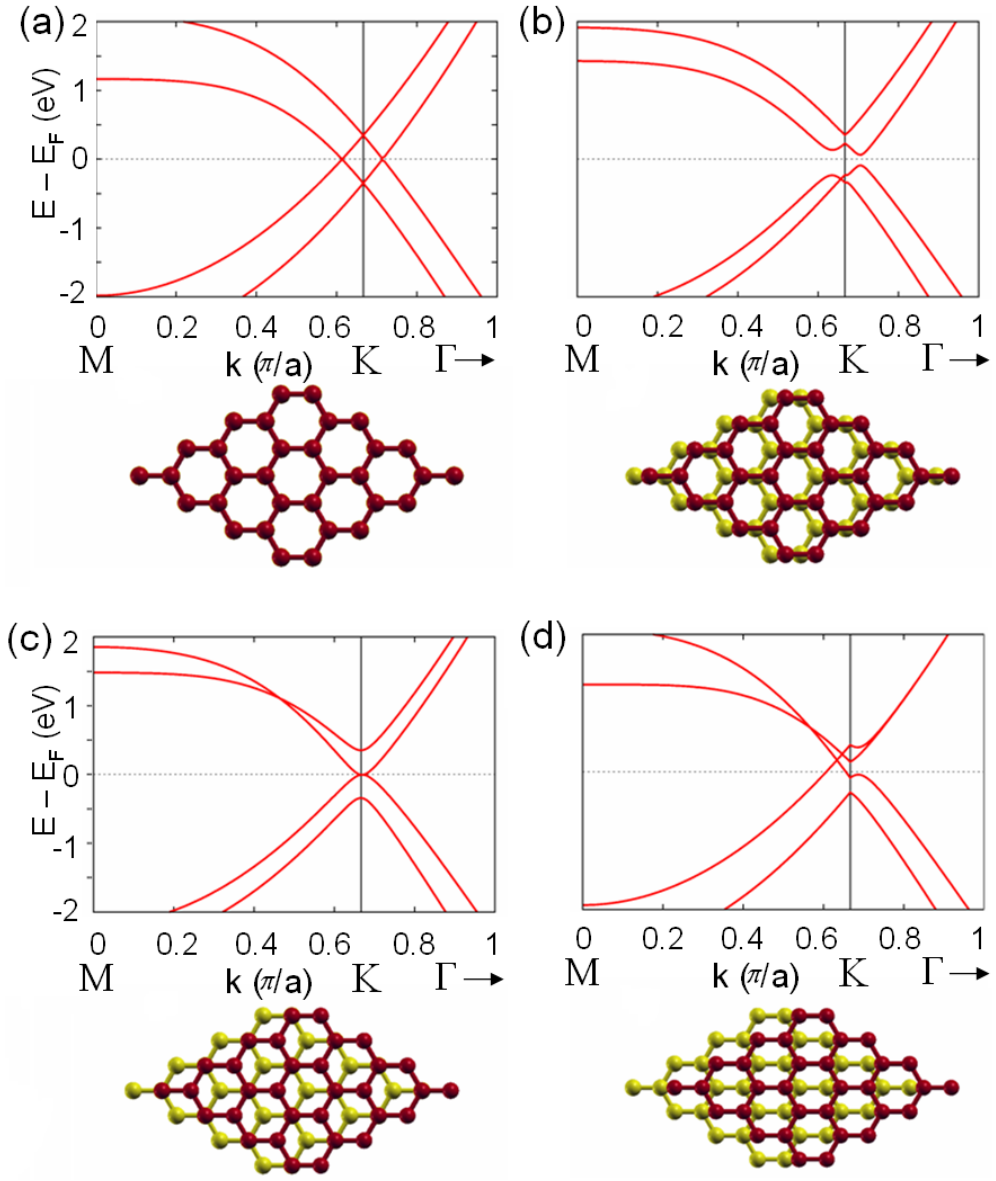

Figure 5.14 Calculated band structures of shifted bilayer graphene. (a)-(d), Calculated band structures along the M→K→Γ direction for two layers of graphene (Top) with corresponding atomic structures (Bottom) having different relative shifts in the armchair direction. (a) and (c) are for AA and AB stacking, respectively, while (b) and (d) are intermediate stackings. In (a), two pairs of bands cross at E_F away from the K point and have linear dispersion. In (c), conduction and valence bands touch at E_F at the K point and have quadratic dispersion. The intermediate case (b) shows a gap, with band extrema away from the K point. In (d), a band crosses E_F at two points away from the K point. The calculations were conducted by Kevin T. Chan and Marvin L. Cohen.

Chapter 6
Ripping graphene: Preferred directions

In many solids, the formation of cracks due to applied stress is a well-known failure mechanism, and hence one of the most important problems in materials science. In a two-dimensional sheet-like material such as graphene, applied tensile stress can also lead to catastrophic failure (ripping) by related crack formation, which we call tearing. The study of tearing in graphene is not only critical in gaining an understanding of the fundamental two-dimensional interatomic interactions, but it has ramifications for a host of mechanical applications (as well as electronic and thermal applications).

Theoretical studies including molecular dynamics simulations have given some insight into the mechanical properties and breakdown mechanisms of graphene under tension [124-128]. Previous experimental studies on graphene's mechanical properties include nano-indentation using atomic force microscopy [12, 129], and an investigation of graphene tearing related to the interaction between graphene and substrates [130]. Most experimental studies, however, have suffered from moderate spatial and time resolution, making it difficult to observe local tear shapes, or their modes of propagations in real time.

In this chapter, we investigate experimentally and theoretically tears in suspended monolayer graphene. We examine the crystallographic orientations of torn edges using TEM imaging and electron diffraction. Torn edges induced by mechanical stress maintain straightness for substantial distances (fractions of microns or greater) in either armchair or zigzag direction and occasionally change directions by 30 degrees (or multiples of 30 degrees). We also observe in real time the propagation of tears stimulated by electron beam irradiation. Theoretical simulations which take into account unpaired electrons at torn edges show preferred armchair and zigzag directions for graphene ripping, with occasional tear kinks, in agreement with experimental observations.

The graphene membrane occasionally develops tears, due to unavoidable mechanically applied stress during the graphene transfer process that involves wet etching and drying in air. Figure 6.1a shows a TEM image of suspended graphene transferred to a TEM grid. The outer circle is the amorphous carbon support boundary for the graphene membrane. A single graphene tear, outlined with a dashed line for clarity, originates from the lower left edge of the carbon support and then extends toward the central region of the membrane. A zoomed-in image around the tear shows that the opening is wider near the carbon support and gets narrower around the tip of the tear, as shown in Fig. 6.1b. This and similar images consistently show that torn edges in graphene are generally straight with occasional changes in direction of 30 degrees, which strongly suggests that the directions of the observed tears are closely related to graphene's hexagonal lattice symmetry.

To investigate the crystalline directions of torn graphene edges, we perform electron diffraction near tear regions. We note that the samples are, within the 1.2 μm diameter circular suspended membrane region, typically single-crystal (see below for behavior near grain boundaries) [94]. The inset of Fig. 6.1a shows the rotation-calibrated diffraction pattern

of graphene for the associated membrane. From the diffraction pattern, we can assign the crystalline direction of the graphene lattice as shown in Fig. 6.1b. We find that the torn edges are aligned with either armchair or zigzag directions. The red and blue dotted lines in Fig. 6.1b represent armchair and zigzag edges in the tear line, respectively. Similar analysis of tears in different suspended graphene membranes consistently show that tears are straight along either the armchair or zigzag directions and occasionally change directions in multiples of 30 degrees.

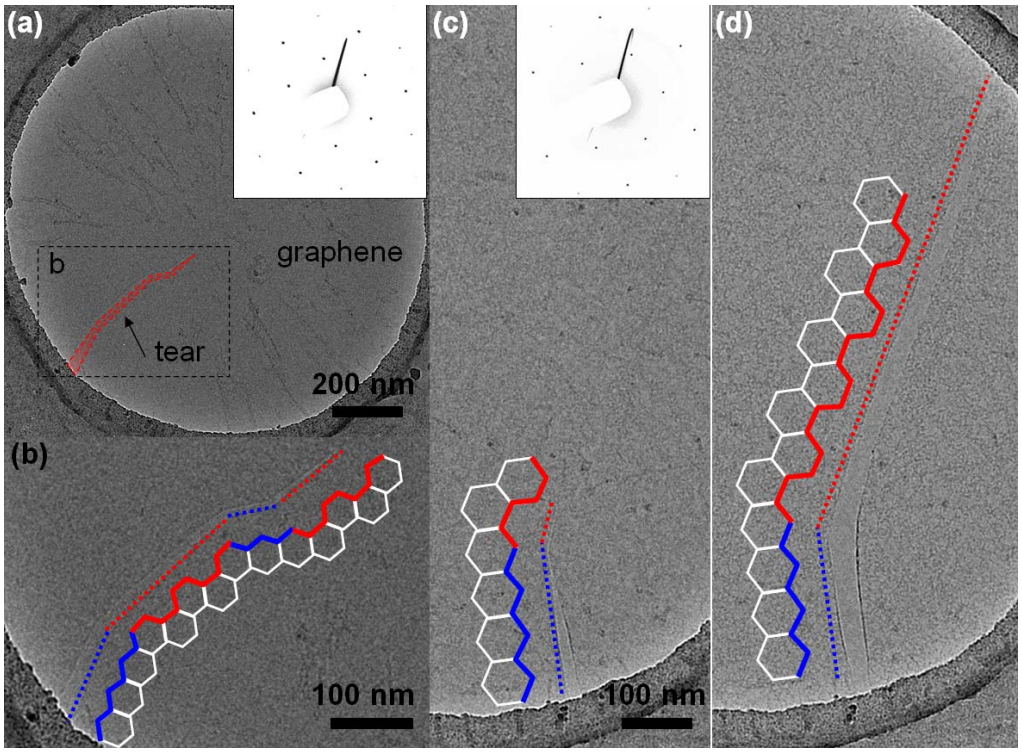

Figure 6.1 Tears in a suspended graphene membrane. (a) TEM image of suspended graphene transferred to a Quantifoil holey carbon TEM grid with a tear near the edge of the carbon support. The inset is the rotation-calibrated diffraction pattern of graphene. The dashed rectangle is the field of view for Fig. 1b. (b) Zoomed-in TEM image of the tear in graphene. The tear exhibits straight lines with the direction occasionally changing by 30 degrees. The red and blue dotted lines represent armchair and zigzag tear edges, respectively. (c) TEM image of a graphene tear before the propagation. The inset is the rotation-calibrated diffraction pattern of graphene membrane. (d) Propagated tear in graphene under the electron beam. The freshly torn line is straight following the armchair direction of the graphene lattice.

Tears are found both spanning the entire membrane or only part of the membrane (as in Fig. 6.1a-c). We find that partially-spanning tears can sometimes be induced to propagate further by action of the TEM electron beam. Fig. 6.1c and 6.1d show the same area of graphene before and after illumination by the electron beam. The tear maintains its straightness as it grows from its tip. In Fig. 6.1d, the freshly torn edge follows the armchair direction of graphene lattice. The propagation of tears can occur quite fast (up to ~ 1 μm/sec)

with even low electron dose (~ 0.01 A/cm^2). Previous TEM studies, including atomic resolution TEM work on graphene, provide possible explanations to the mechanisms of observed tear propagation under the electron beam [71, 73, 131]. Electron-beam irradiation effects can be categorized into elastic scattering effect (knock-on damage) and inelastic scattering that produces electronic excitations [132, 133]. Among these, knock-on damage is generally believed to be the main irradiation effect in graphene since excitation effects are rapidly quenched as a result of metallic nature of graphene [132]. For pristine graphene, the knock-on energy threshold for incident electrons is around 86 keV [134]. We mainly use an electron energy of 100 keV for TEM imaging in this study; however, tear propagation has been observed at lower electron accelerating voltages, including 80 kV and even 20 kV. Moreover, the rate of tear propagation seems to be enhanced at 20 kV, which does not agree with what we might expect from knock-on irradiation effects [132]. These facts demonstrate that knock-on damage is not the main mechanism of tear propagation.

High-energy electrons can excite the electronic states in graphene by inelastic scattering and breaking bonds locally through ionization damage [132, 133]. The effects of ionization damage will be especially dramatic at highly strained and therefore vulnerable carbon-carbon bonds. We believe that the observed tear propagation is mainly caused by a combination of local high strain concentrated at tear tips, and ionization effects; high-energy electrons transfer energy to strained carbon-carbon bonds and induce tear propagation. Electron-beam induced heating is another potential contributor to tear propagation (since the negative coefficient of thermal expansion of graphene [23] would increase the tensile strain with heating and thus promote tearing), but given our experimental parameters and graphene's high thermal conductivity [20], we find that heating is not significant during the imaging [135]. We also note that perfect graphene membranes without preexisting tears exhibit no induced tears under even much higher electron dosages.

Figure 6.2 shows the crystalline direction-dependent histograms of torn edges. Here we define zero degrees as along the zigzag direction of tear lines. For statistical significance, we investigate more than 50 partially torn graphene membranes. As expected, a preponderance of the tear lines is aligned with either the armchair or zigzag direction. Interestingly, armchair direction tear lines are twice as prominent as those in the zigzag direction.

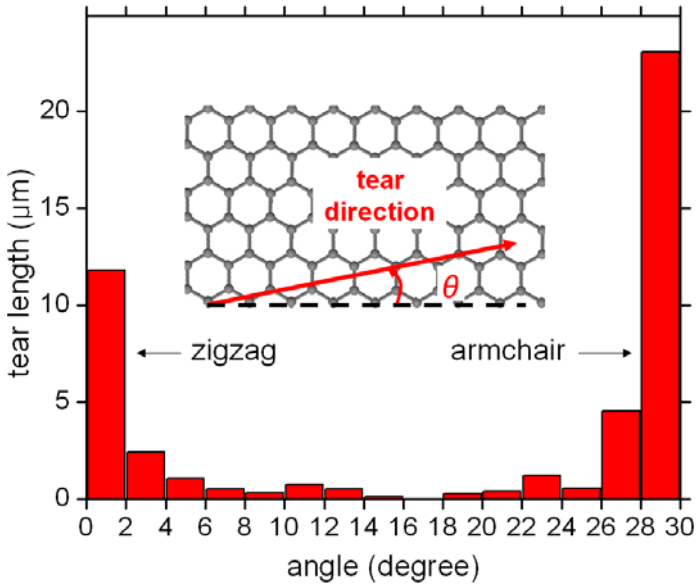

Figure 6.2 Histograms of angle dependence in torn edges. Zero degrees is defined as the zigzag direction of the graphene lattice (Inset). Most tear lines align to either the armchair or zigzag direction. Armchair-aligned tear lines are about twice as abundant as zigzag.

Figures 6.3 and 6.4 show atomic-resolution TEM images of crack edges of graphene. These edges are in situ fabricated with electron beam and allow us to obtain atomically smooth edge structures, which is difficult to achieve with graphene samples produced with chemical processes. Figure 6.3 shows an armchair crack edge segment (longer than 20 nm), where more than 90 % of edge maintains the perfect armchair structure with occasional missing edge carbon atoms.

Figure 6.4 shows atomic-resolution TEM image of crack edge in zigzag direction. However, instead of pure zigzag atomic structure, we observe the extended pentagon-heptagon (5-7) reconstructed edge structure. This 5-7 reconstructed edge can be obtained with local carbon bond rotations and is expected to have lower edge energy compared to the pure zigzag edge structure [136]. Under the electron beam illumination, we also observe transitions between the 5-7 reconstructed structure and pure zigzag structure [137]. Figures 6.3 and 6.4 also demonstrate that intentionally tearing graphene can be a good way to obtain graphene nanoribbons with atomically well-define edges.

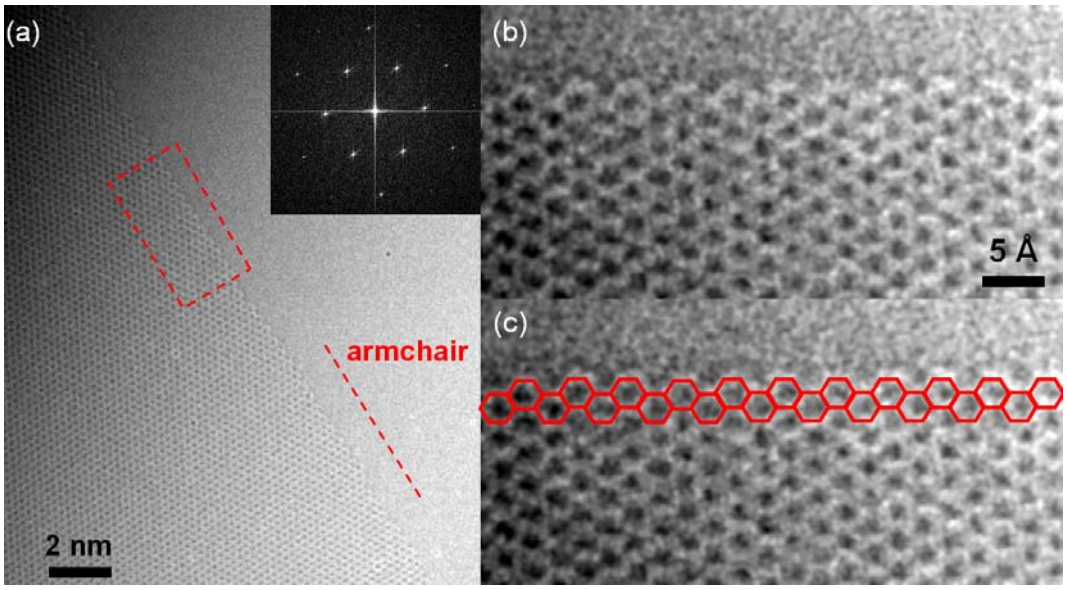

Figure 6.3 Atomic-resolution TEM image of graphene crack edge in armchair direction. (a) Atomic resolution TEM image of armchair crack edge. The inset is the Fourier transform of the image. The red dashed box is the field of view for figure b and c. (b) The zoom-in image of the graphene edge. (c) TEM image with atomic overlay. The figure clearly shows a pristine armchair graphene edge.

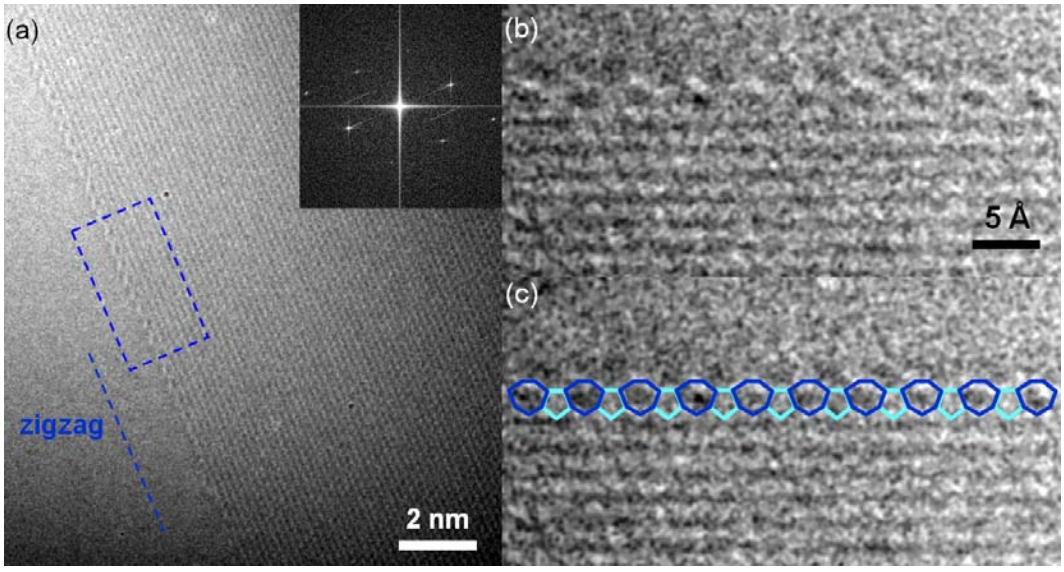

Figure 6.4 Atomic-resolution TEM image of graphene crack edge in the zigzag direction. (a) Atomic resolution TEM image of a crack edge in zigzag direction. The inset is the Fourier transform of the image. The blue dashed box is the field of view for Figure b and c. (b) Zoom-in image of the graphene edge. (c) The same Figure with atomic overlay. The figure clearly shows a pentagon-heptagon reconstructed zigzag graphene edge.

We now turn to a theoretical analysis of tearing in graphene. We first note that the prevalence of tear lines in armchair and zigzag directions, and abrupt angle changes between these directions, are not obvious from simple classical fracture theory [138]. The strength to crack propagation is measured by the critical stress intensity factor $K \sim \sqrt{Y \cdot \gamma}$, where Y is Young's modulus and γ is surface energy, or edge energy in case of graphene. Since Y is isotropic for graphene, critical stress will be mainly determined by the edge energy γ. Our observations imply that the angle-dependent energy curve for graphene edge is a concave function with minima at 0 and 30 degrees, an unusual trend [139].

Consider a graphene sheet under strain applied at an angle χ to the armchair direction of graphene. The inset in Fig. 6.5 shows possible crack paths in this situation: (green) shortest path normal to the applied strain with an intermediate orientation of the crack; (red and blue) along pure armchair or zigzag directions at an acute angle to the strain direction; or (yellow) a piecewise-straight crack composed of long pure zigzag and armchair segments such that on average it remains normal to the strain. The plot in Fig. 6.5 shows the dependence of energy of each crack type on the orientation of strain using the analytical expressions for edge energies [139] and numerical data calculated using the ReaxFF forcefield [140, 141]. At each given angle χ, our model predicts the lowest-lying curve to represent the energetically preferred crack direction. It can be seen that there exists only a narrow interval of orientations at which intermediate-direction cracks are favored, and under realistic conditions of inhomogeneous local strain distribution that also changes as the crack propagates, only straight armchair or zigzag crack edges should be seen.

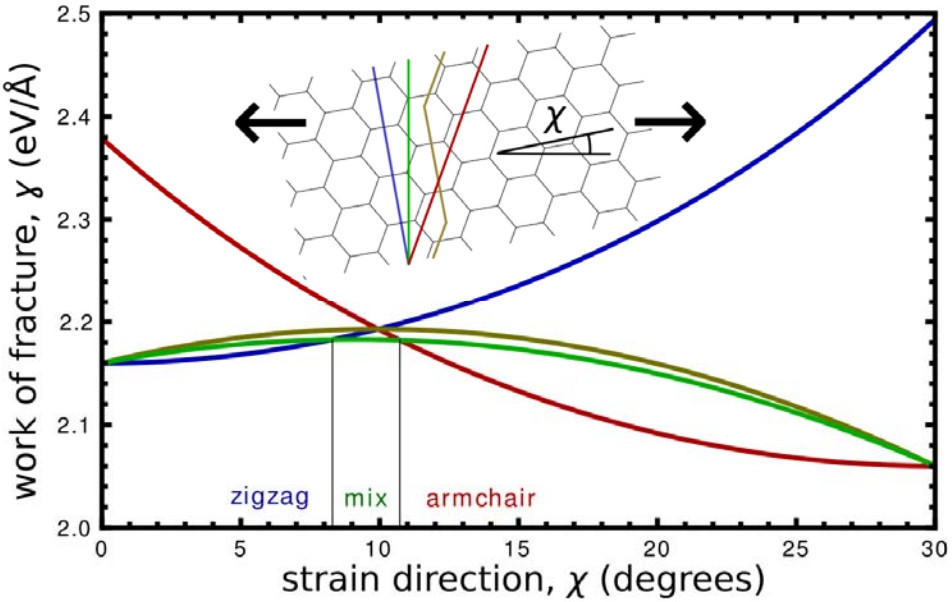

Figure 6.5 Direction-dependent energetics of cracks in graphene. At a given orientation of local strain with respect to graphene lattice, as described by the angle χ, the lowest-energy curve represents the stable crack direction. The intermediate direction of edge (green) is favorable only in a narrow window of χ, so that armchair and zigzag-edged tears should be observed predominantly. The calculations were conducted mainly by Vasilii I. Artyukhov and Boris I. Yakobson.

To verify the predictions of this energetic argument, we simulate ripping graphene under tension using the same forcefield. We take rectangular graphene sheets with a tear tip placed at the right edge (marked with yellow arrows) as shown in Fig. 6.6a-c. The graphene lattice is oriented with the horizontal along an (a) armchair, (b) zigzag, and (c) intermediate edge, respectively. Tension is applied vertically and induces the propagation of the tears from right to left in the simulation. Fig. 6.6d-f shows final results after the tear propagations. The torn edges maintain straightness in the armchair (red dashed lines) or zigzag (blue dashed line) directions as shown in Fig. 6.6d-e. As predicted above, for the intermediate direction, the tear edge follows the horizontal direction in the beginning but changes its direction to follow the armchair edge direction, thus minimizing crack energy despite increasing its length (Fig. 6.6f). These simulation results agree very well with our experimental observations. We also note that torn edges, especially in the armchair direction, exhibit atomically clean edge structures.

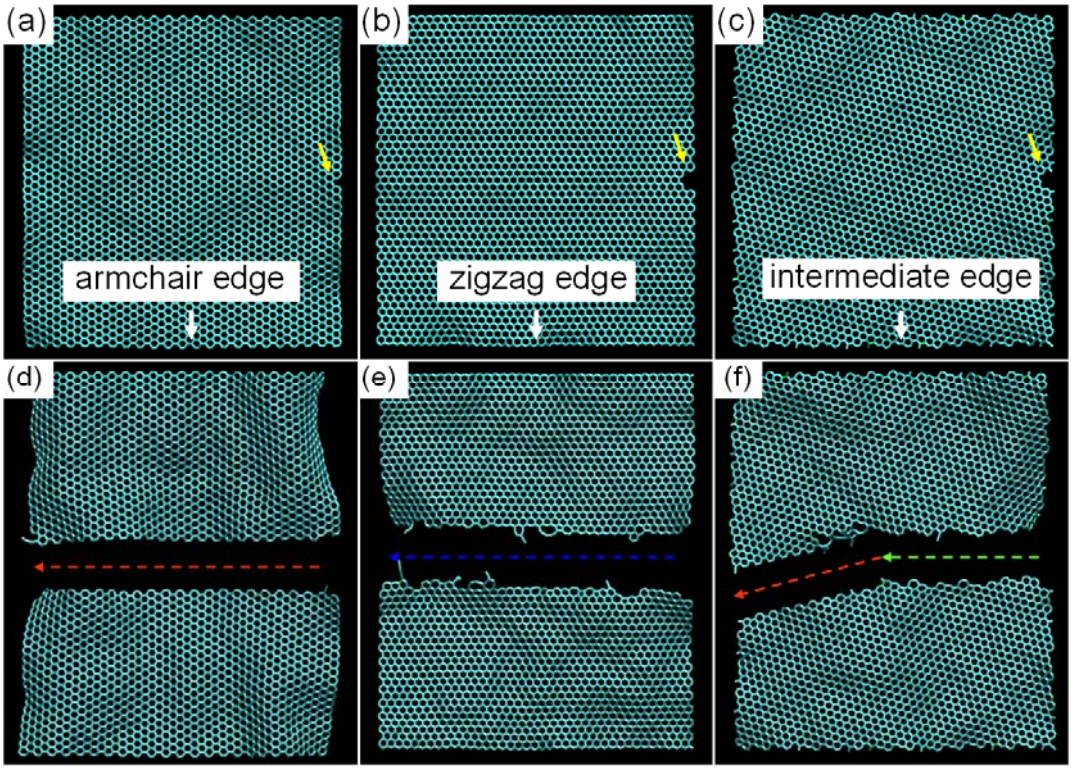

Figure 6.6 Simulations of ripping graphene. (a-c) Rectangular graphene sheet seeded with a tear tip at the right side (marked with yellow arrows). In the horizontal direction, the edges of graphene show (a) armchair, (b) zigzag and (c) intermediate edges, respectively. Tension is applied vertically and induces the propagation of the tears from right to left in the simulation. (d-f) Simulation results after the tear propagations. (d-e) The torn edges maintain straightness in the armchair (red dashed lines) or zigzag (blue dashed line) directions. (f) For the intermediate direction, the tear edge initially follows the horizontal direction (green) but then changes direction and follows the armchair edge direction. The simulations were performed by Vasilii I. Artyukhov and Boris I. Yakobson.

Also of interest is the behavior of tears in the vicinity of, or even crossing, structural anomalies such as folds or grain boundaries (GBs). Although our suspended membranes are mostly defect-free, on occasion folds [18] or GBs [94, 142] will cross the sample, as our CVD graphene exhibits tilt grains of size with a few to tens of micrometers [94]. Previous studies suggest that the presence of a GB may have detrimental effects on the mechanical strength of the graphene membrane [60, 129, 142]. In our experiments, graphene GBs are readily identified with observations of adsorbents along the GBs and diffraction analysis [94, 142]. Interestingly, we find that, in cases where GBs do exist within the suspended membrane, the observed tears do not generally coincide with GBs, and the same crystalline orientation is seen on the two opposing sides of a tear line. Invariably we observe tear lines following the usual armchair or zigzag directions in the graphene lattice which may happen to cross a GB with minimal perturbation, as shown in Fig. 6.7.

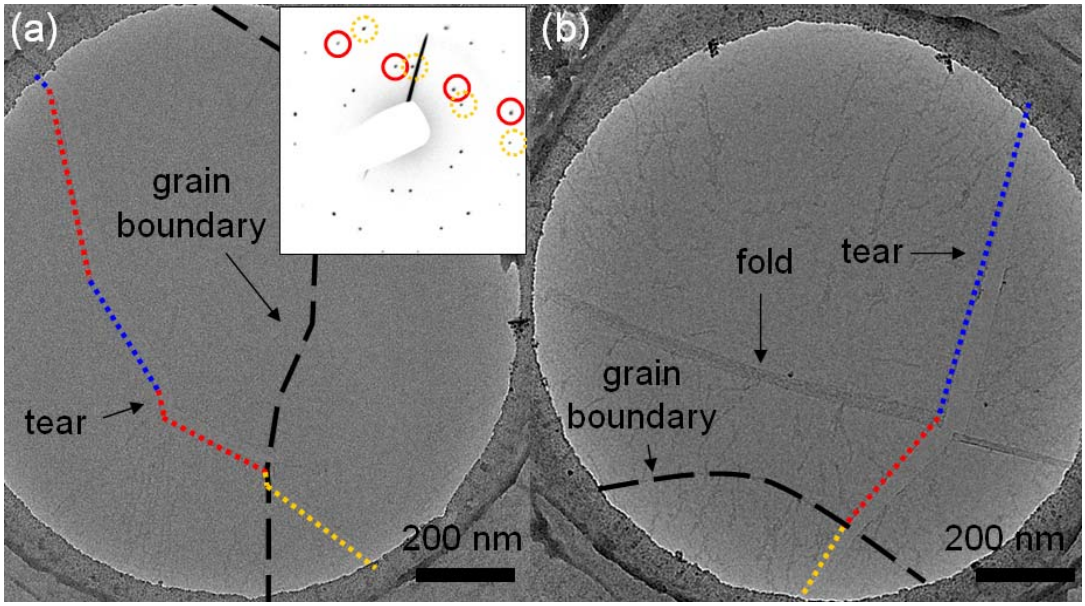

Figure 6.7 Graphene tears crossing grain boundaries (GBs). (a) TEM image of graphene tear crossing, not following, a grain boundary (GB) in graphene. The GBs are identified by the high absorbent concentration along the grain boundary together with electron diffraction. Inset of the diffraction pattern around the GB showing two sets of hexagonal patterns from two adjacent tilt grains, where the hexagonal pattern marked with red and dashed yellow circles corresponds to the grain in the left and right sides, respectively. The blue dotted lines represent tear lines in the zigzag direction. The red and yellow dotted lines represent tear lines in the armchair direction. (b) Another TEM image of a graphene tear crossing a GB and fold in graphene. The blue dotted line represents a line in the zigzag direction. The red and yellow dotted lines represent the armchair direction.

The observation that tears cross GBs instead of following them appears to contradict the common-knowledge notion that GBs represent "weak spots" of materials. The apparent disagreement originates from the fact that in ductile materials, GBs prevent the migration of defects which is responsible for plastic flow, thus making the material less ductile and easier to break. However, at relevant experimental temperatures (and timescales), sp^2 carbon is expected to behave as a completely brittle material [143], making this phenomenon irrelevant. GBs in graphene do contain dislocations that produce strain, but the strain fields of consecutive 5-7 pairs actually cancel out locally [144]. From the viewpoint of edge energy analysis, it is important that graphene GBs typically have some random orientation, not coinciding with either AC or ZZ direction. Hence, if the material were to break along the GB, this would expose an energetically unfavorable edge.

At this point it is worth recalling that K_c also depends on the stiffness of the material, which becomes direction-dependent in the vicinity of a GB. Specifically, it decreases for loads normal to the boundary, which can make non-pristine edges stable. Therefore, the behavior of cracks near grain boundaries can be expected to be bimodal: when the stress is normal to the GB, as is in the case of, e.g., recent experiments where AFM tips were indented into the middle of a grain [129, 142], the tear can follow the boundary. However, if the tear initiated away from the GB and at some random orientation with respect to it (so that the

strain direction is away from normal to the GB), the stiffness it experiences is more or less unaffected by the GB, and the tear will pass right through it, simply switching to the most favorable direction in the new grain—as is indeed observed in the present work.

In conclusion, we have shown that tears in suspended monolayer graphene predominantly align to the armchair or zigzag directions. Real-time tear propagation has been observed under an electron beam, which is mainly attributed to a combination of high strain at the tip of tears and ionization effects from high-energy electrons. Our theoretical analysis based on the analytical expression for direction-dependent edge energy explains why tears predominantly form along armchair and zigzag directions, and molecular dynamics simulations confirm this explanation. Electron-beam assisted ripping graphene may be an effective and simple way to selectively tailor graphene edges. The edge structures of graphene have important effects on the electronic properties [145]. Controlling the edge structure of graphene, therefore, is of very importance for graphene electronic applications. Our demonstration of tear propagation in graphene via electron beam may be an interesting way to manipulate graphene membranes and allow for selective edge termination.

Chapter 7
Thermal stability of graphene and high-temperature *in situ* TEM monitoring

Graphene has various interesting thermal properties. For example, suspended graphene has thermal conductivity of about 5000 W/mK at room temperature [20]. Graphite is stable at very high temperatures (sublimation at around 4000 K) [146] and graphene, or suspended graphene, may also be thermally robust. On the other hand, the two-dimensional nature of graphene may limit its stability. Unfortunately, due to difficulties of preparing suspended graphene samples and the experimental set-up, there has not been an experiment on high-temperature thermal stability of suspended graphene.

In this chapter the thermal stability of suspended graphene will be discussed. We prepare suspended single-layer graphene and perform in situ Joule heating experiments in a transmission electron microscope (TEM). We estimate that suspended chemical vapor deposition (CVD)-grown graphene is stable at temperatures up to (or exceeding) 2600 K.

Figures 7.1a and 7.1b show sample preparation and experimental set-ups for in situ Joule heating experiments on suspended CVD-grown graphene. We transfer the graphene to a commercial TEM grid (Quantifoil holey carbon film grid) using a clean direct transfer process [44]. After the transfer, the TEM grid is cut with a razor blade into small pieces and attached to an aluminium wire with conducting epoxy (Fig. 7.1a). This sample is inserted into the TEM (JEOL 2010) for in situ experiments. Near the region cut by the razor blade, we locate suspended graphene on the Quantifoil amorphous carbon film (Fig 7.1b). The amorphous carbon film gives mechanical support for the suspended graphene. The large area of CVD-grown graphene makes it relatively easy to locate suspended graphene and perform in situ experiments. Using a nanomanipulation platform inside the TEM (Nanofactory AB), we make an electrical contact to the suspended graphene with a mobile tungsten probe and induce Joule heating (Fig 7.1b).

To confirm that the graphene is single layer, we characterize CVD-grown graphene by Raman measurement and electron diffraction. Raman measurements are performed using a Renishow Raman system (Model – inVia) with a 514 nm laser. The laser beam size of about 1 μm is used. Fig. 7.1c shows the representative Raman spectrum from graphene which has been transferred to silicon oxide/silicon substrate. The absence of a D peak shows that the CVD-grown graphene is of high quality. The intensity ratio of 2D and G peaks confirms that the graphene is mostly single layer [31]. The electron diffraction pattern also confirms that graphene is mostly single layer [44].

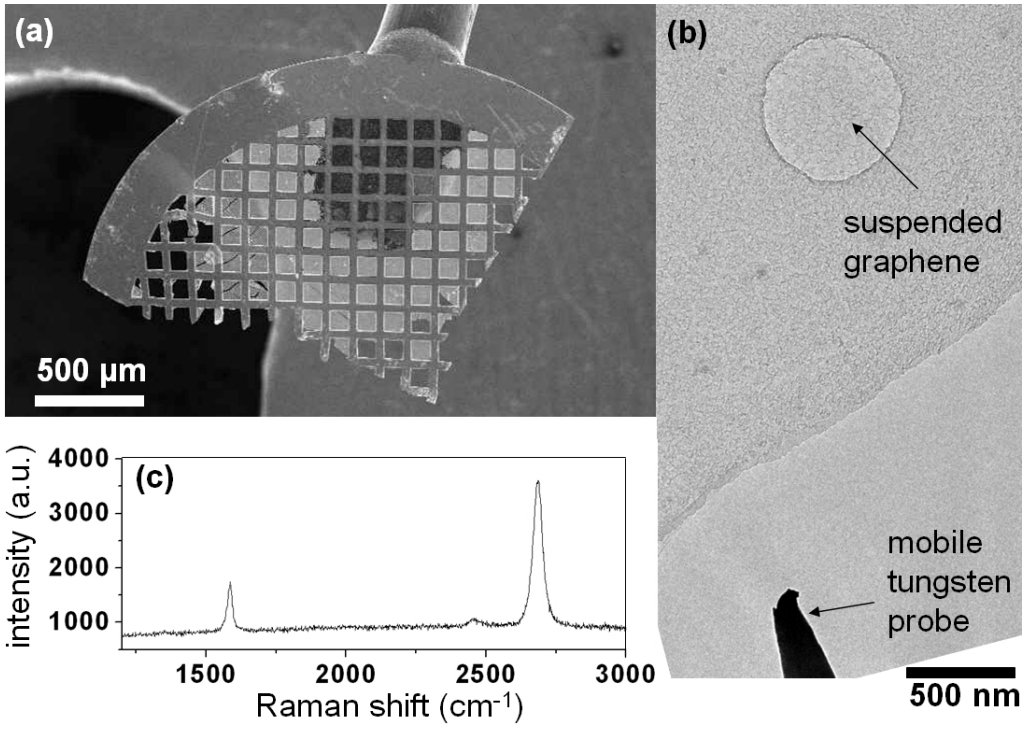

Figure 7.1 Sample and experimental set-up of in situ Joule heating of suspended graphene. (a) SEM image of a TEM grid (Quantifoil holey carbon film grid), covered with graphene and then cut with a razor blade. The TEM grid is attached to an aluminium wire for insertion to a TEM holder. (b) TEM image of the graphene sample and the mobile tungsten probe for the in situ TEM experiment. Suspended graphene is found inside the holes in the amorphous carbon film. Graphene is contacted by the mobile tungsten probe, and electrical current flows through the graphene. (c) Raman spectrum of CVD-grown graphene transferred to silicon oxide/silicon substrate.

We find that the suspended single-layer graphene can be heated up and remain stable at 2600 K (and possibly higher temperatures) with Joule heating. Figure 7.2a shows the TEM image of suspended graphene after Au is pre-deposited with an e-beam evaporation process. TEM images have been taken with acceleration voltage of 100 keV to minimize the electron beam damage to the sample during the experiments. Using the mobile tungsten probe, we establish electrical contact to the graphene and induce the Joule heating. As we increase the Joule heating power, we observed in situ evaporation of gold nanoparticles (Fig. 7.2b-d). From this result, we confirm that the suspended graphene has reached at least 1275 K, the evaporation temperature of Au nanoparticles [147].

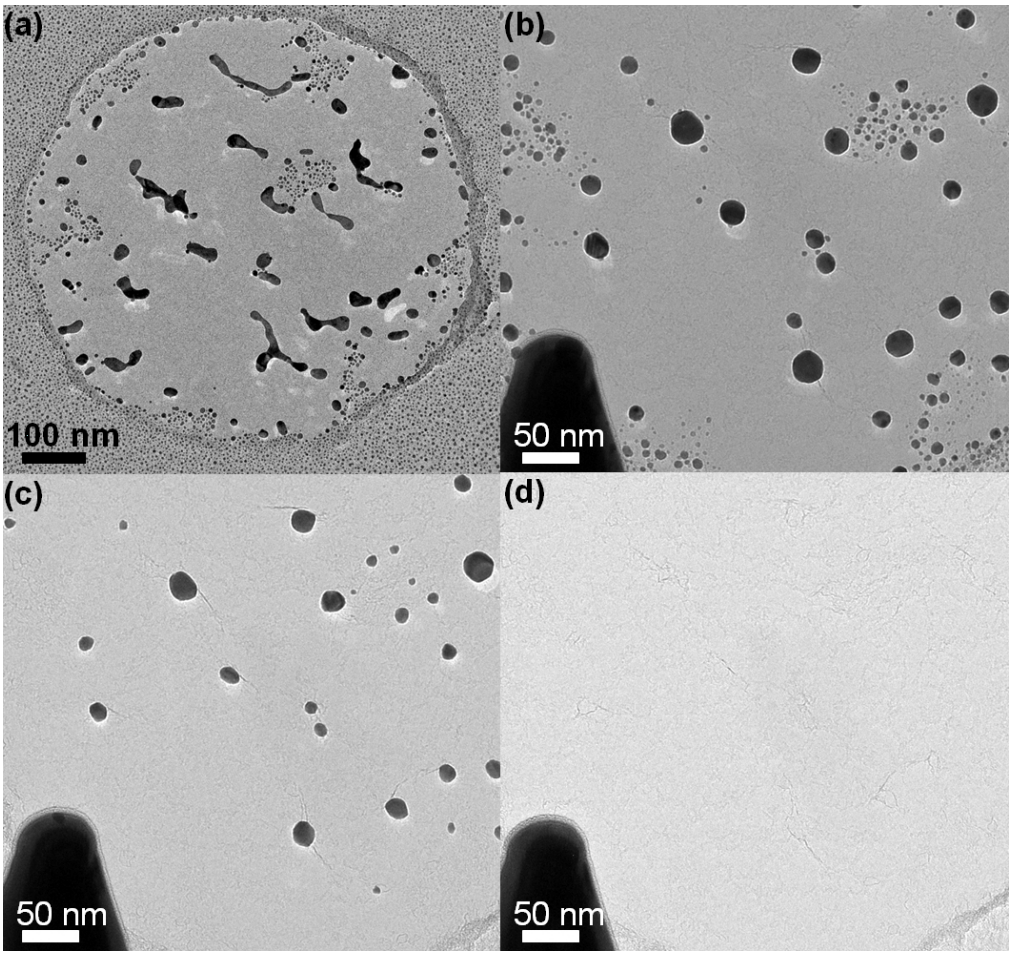

Figure 7.2 In situ evaporation of pre-deposited Au particles on suspended graphene. (a) TEM image of suspended graphene after Au (nominal thickness of 0.6 nm) is deposited with an e-beam evaporation process. (b-d) Sequential TEM images of in situ evaporation of Au particles on the suspended graphene. (b) TEM image of the Au-deposited graphene after establishing electrical contact with the mobile tungsten probe. The tungsten probe is positioned in the left-lower corner. (c) TEM image as Au particles start to evaporate with Joule heating. (d) TEM image of the graphene after Au particles have completely disappeared.

Figure 7.3a shows Joule heating power versus time for the in situ experiment. When the Joule heating power is P_1 = 0.55 mW, all the Au particles pre-deposited on graphene have completely evaporated. Later, the graphene was found to be stable with higher Joule heating power, P_2 = 1.9 mW.

Our procedure for estimating the temperature of suspended graphene with Joule heating power P_2 is as follows. The exact position of maximum temperature during a Joule heating experiment depends on sample geometry and requires knowledge of the thermal and electrical properties of the material (graphene and amorphous carbon film). However, since the gold frame of the TEM grid and the tungsten probe are thermally well anchored and act as heat sinks, the region of maximum temperature in the sample is in the central suspended region of the carbon film and graphene as shown in Figure 3(b).

We can set an equation from the thermal equilibrium conditions,

$$P_{heating} - P_{radiation} = c\kappa \cdot \Delta T \tag{7.1}$$

where P_{heating} is Joule heating power, $P_{\text{radiation}}$ is power escaping through radiation, c is a sample and experiment dependent constant, κ is the average thermal conductivity of sample between the maximum and minimum temperature region, and ΔT is temperature difference between the maximum temperature, T_{max}, and minimum temperature, T_{min}, in the sample.

We can safely assume that the minimum temperature is room temperature, T_{r} = 300 K (at the tungsten probe and gold frame). $P_{\text{radiation}}$ is estimated by using

$$P_{radiation} = \int_S \varepsilon\sigma T(S)^4 \, dS < A\varepsilon\sigma T_{\max}{}^4 \tag{7.2}$$

where ε is emissivity (assumed to be 1 in the calculation), σ is the Stefan-Boltzmann constant and S is the surface area of the sample. We can set an upper limit on $P_{\text{radiation}}$, which is $A\varepsilon\sigma T_{\text{max}}{}^4$, where A is the surface area of the amorphous carbon film and graphene (from the hottest region in the sample). A is estimated as 200 μm^2 from a TEM image in our experiment. The radiation power $P_{\text{radiation}}$ is found to be negligible compared to P_{heating} when T_{max} is lower than 1500 K.

Putting $T_{\text{max}} = T_1$ = 1275 K and P_1= 0.55 mW, the reference point deduced from the Au particle evaporation, in the eq. (1) and eq. (2), we find $c\kappa = 5.6 \times 10^{-4}$ mW/K. Using this $c\kappa$ value and solving eq. (1) and eq. (2) with a new Joule heating power, P_2 = 1.9 mW, gives a lower limit for T_{max} at 2600 K. Since thermal conductivity κ falls due to enhanced phonon-phonon scattering at high temperatures [147], the assumption of the same $c\kappa$ value tends to give lower values in the calculation of T_{max}. Therefore, we conclude that the suspended CVD-grown graphene is stable at temperatures of at least 2600 K.

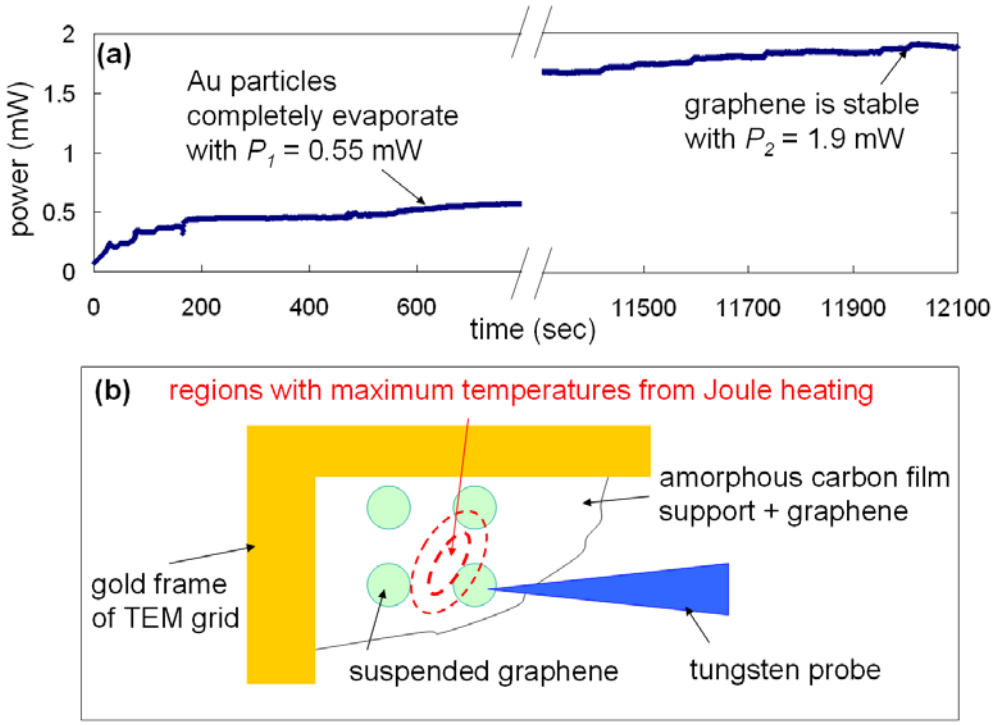

Figure 7.3 Joule heating power data and experimental geometry of the in situ experiment. (a) Joule heating power variation in time during the experiment. (b) Geometry of the in situ Joule heating experiment. Electrical current is flowing from the tungsten probe to the gold frame and inducing Joule heating on the suspended graphene and carbon film. Graphene regions between the gold frame and the tungsten probe reach the highest temperature in the sample.

After transferring the graphene to a TEM grid, graphene usually suffers from contamination. The adsorbates on graphene surface contribute to contrast variations from conventional TEM imaging. Joule heating can be used to clean the surface of the suspended graphene by removing adsorbates. Figure 7.4 shows TEM images of the suspended CVD graphene before and after the in situ Joule heating. In Figure 7.4a, the carbon residues, which are originated from the graphene synthesis and transferring process, are located in 30 ~ 50 % of area on the graphene surface. As the graphene is heated up by Joule heating, the carbon residues start to undergo structural reconstructions. Notably, the edge contrast of individual residues becomes higher (Fig. 7.4b).

These structural transformations can be explained with the crystallization of carbon residues into graphene flakes. The edge lines of small graphene flakes become clear as the folded-edge structures, which can produce clearer line, develop at high temperatures. This structural change of graphene flakes will be further discussed later in this chapter. Moreover, extended Joule heating can also remove these graphene flakes from the substrate graphene and produce relatively large area of very clean single-layer graphene. This cleaning process and resulting graphene membranes can be very useful as a TEM imaging membrane (Figure 7.4c).

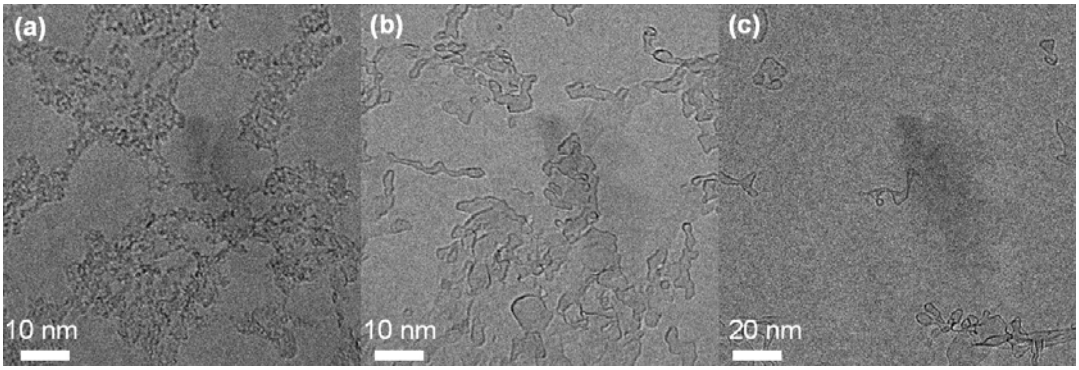

Figure 7.4 Joule heating-induced cleaning of suspended graphene surface. (a) TEM image of CVD-grown graphene after transferring to the TEM grid. Residue from the transferring process, together with extra layer of graphene flakes from the graphene synthesis process, cover some areas of graphene. (b) TEM image of the graphene after Joule heating. Due to the Joule heating, graphene flakes undergo reconstruction process and edges of graphene flakes begin to stand out. (c) TEM image of the suspended graphene after further Joule heating treatment. Most of the graphene flakes disappear leaving the suspended graphene of very clean surface.

At the elevated temperatures from the Joule heating, crystallized graphene flakes on the background graphene membranes undergo structural changes and make various movements. Figure 7.5 shows the sequential TEM images of these structural changes and movements of graphene flakes. By comparing Figure 7.5a and 7.5b, we notice that some edge of a graphene flake suddenly becomes sharp. The graphene flake curls up and makes a folded-in edge structures at high temperature annealing [87, 88, 148]. At high temperatures, the folded edge structure seems preferable than unfolded edge structure. The sharp edge lines around the graphene flakes (Figures 7.5 and 7.6), therefore, can be interpreted as folded-in double-layer edge of graphene flakes.

In Figure 7.5b-f, a graphene flake, circled with dashed line, makes various lateral movements on the graphene substrate. In Figure 7.5c, we observe that the graphene flake make a translational movement. Then, the graphene flake starts to make rotational movements. It rotates multiple times about 10 degree clock-wise and counter-clock-wise (Figure 7.5d-f). One thing to notice is that the upper part of the graphene flake seems to be anchored to the neighboring graphene flake.

Interestingly, we observe that extended Joule heating can anneal and weld graphene flakes together at very high temperatures. Figure 7.6 shows sequential TEM images of the coalescence process. The graphene flakes, which are also shown in Fig. 7.5, are monitored as we further increase the Joule heating power. First, the graphene flake at the center makes a counter-clock-wise rotational movement (Figure 7.6a). Later, some part of the graphene flake edge undergoes structural reconstruction, which is marked with the arrowhead. This transformation is possibly because some carbon atoms at the edge evaporate with very high temperatures (Figure 7.6b). Similar phenomenon also has been observed in recent other works [87, 148, 149]. Later in time sequence, we observe the overlapping and coalescence of these two graphene flakes (Figure 7.6c). Finally, the annealing through Joule heating produces a seamlessly-fused graphene flake (Figure 7.6d). This is the first-time demonstration that two

small graphene flakes can be welded together to make a bigger piece. Related welding of two carbon nanotubes has been previously observed [150].

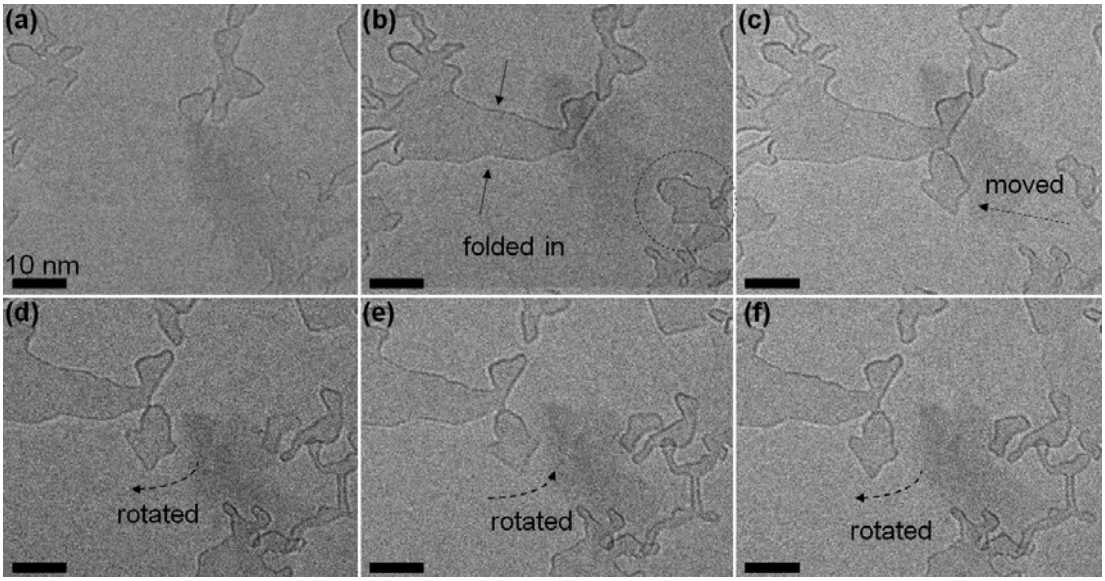

Figure 7.5 Sequential TEM images of translational and rotational movements of small graphene flakes. (a) TEM image of graphene flakes with various shapes on the suspended graphene background. Some graphene flakes show clear edge line (folded edge) and unclear edge (unfolded edge). (b) Clear edge lines (marked with arrows) suddenly appeared in a graphene flake from graphene's folded edge. The graphene flake circled with the dashed line starts to make movements. (c) TEM image after a graphene flake made a translational movement. (d - f) TEM sequential images of rotational movements of the graphene flake.

In this chapter we have shown that the suspended single layer CVD-grown graphene can be stable at very high temperatures (at 2600 K or higher) via in situ Joule heating experiments. Typical TEM heating stages can operate only up to around 1000 K. Even a specialized heating holder can only reach approximately 1400 K [151]. Our in situ Joule heating experimental set-up demonstrates the high-temperature stability of graphene and opens up opportunities for high temperature reaction monitoring beyond the commercial TEM heating stage range.

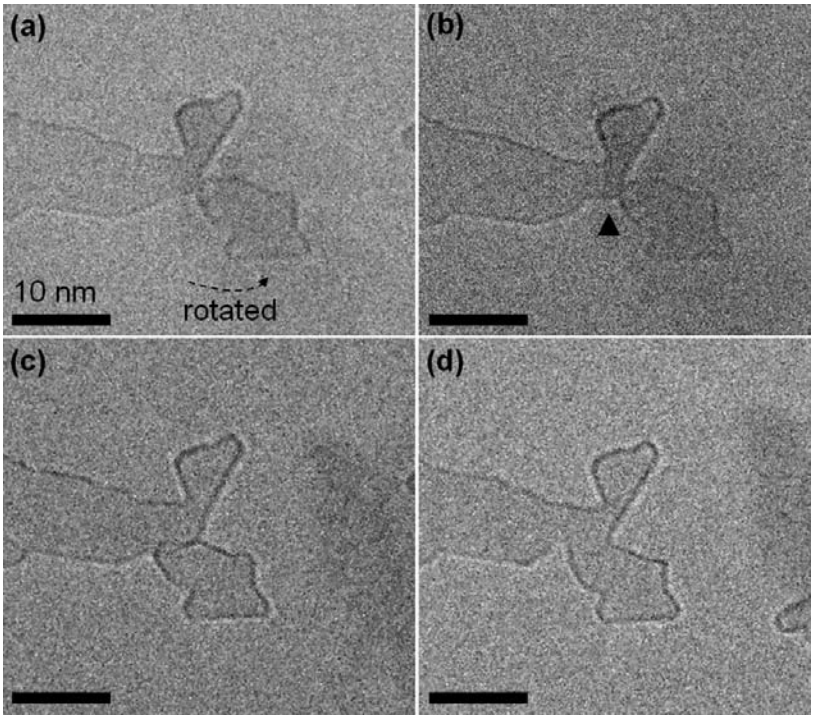

Figure 7.6 Coalescence of graphene flakes. (a) The graphene flake at the center (also shown in figure 4) make a counter-clock-wise rotational movement showing it is just attached not fused to the graphene flake at the left side. (b) With Joule heating, some part of the graphene flake edge (marked with the arrowhead) undergoes the structural reconstruction. (c) Two graphene flakes start to coalesce. (d) Finally, two graphene flakes coalesce together completely.

Chapter 8
Raman spectroscopy of rotated double-layer graphene: Rotational-angle dependence of electronic structures

Recently there has been growing interest in double-layer graphene in which the two graphene layers are not conventionally stacked but relatively rotated by an arbitrary angle [40, 106-108, 152-160]. Such graphene double layers are expected to display characteristics distinct from both monolayer graphene as well as the extensively studied AB-stacked bilayer graphene [5, 102-104]. Previous theoretical investigations suggest that electronic and optical properties of double layer graphene will strongly depend on this rotational angle [107, 108, 152-154]. Because the entire range of rotational angles is in principle experimentally accessible via artificial stacking, the properties of rotated double-layer graphene might be tuned to suit the application at hand, making this material a useful component in future nano-electronic devices. Limited low-energy electrical transport measurements have suggested that rotated graphene layers maintain the linear dispersion relation as in single-layer graphene [155, 160]. Furthermore, angle-resolved photoemission spectroscopy measurement has shown that rotated layers in multilayer epitaxial graphene exhibit weak interlayer interactions [156]. On the other hand, scanning tunneling microscopy studies in the low rotation angle regime have demonstrated strong interlayer interactions such as carrier velocity renormalization and the occurrence of Van Hove singularities away from the Dirac point energy [106, 157]. Despite these suggestive findings and the applications potential, there have unfortunately been no comprehensive experimental or theoretical studies of the influence of rotation angle on the electronic properties of double-layer graphene.

In this chapter we present a systematic experimental and theoretical study of rotated double-layer graphene. We employ Raman spectroscopy, a powerful tool for investigating the electronic and vibrational properties of carbon-based materials [161-164], together with theoretical calculations of the electronic-structure-dependent Raman response. We experimentally sample a range of misorientation angles from 0 to 30 degrees in steps of ~1 degree, and we focus on the intensity, peak position, and peak width of the 2D and G Raman modes. Previous limited Raman studies on folded graphene [165-169] have made interesting observations relevant to rotated double-layer graphene, such as 2D peak blue-shifts and G peak resonance, but the origin of these phenomena could not be clearly identified.

To obtain rotated double-layer graphene we start by synthesizing monolayer polycrystalline graphene via chemical vapor deposition (CVD), yielding material with a grain size of several micrometers [31, 94]. By consecutively transferring two such monolayers of CVD graphene onto a TEM grid [45], we obtain double-layer graphene with domains having randomly rotated stacking angles. We utilize holey carbon transmission electron microscope

(TEM) grids with an array of holes 2 μm in diameter. Within each hole we perform a TEM analysis to identify the misorientation angle of the suspended double-layer.

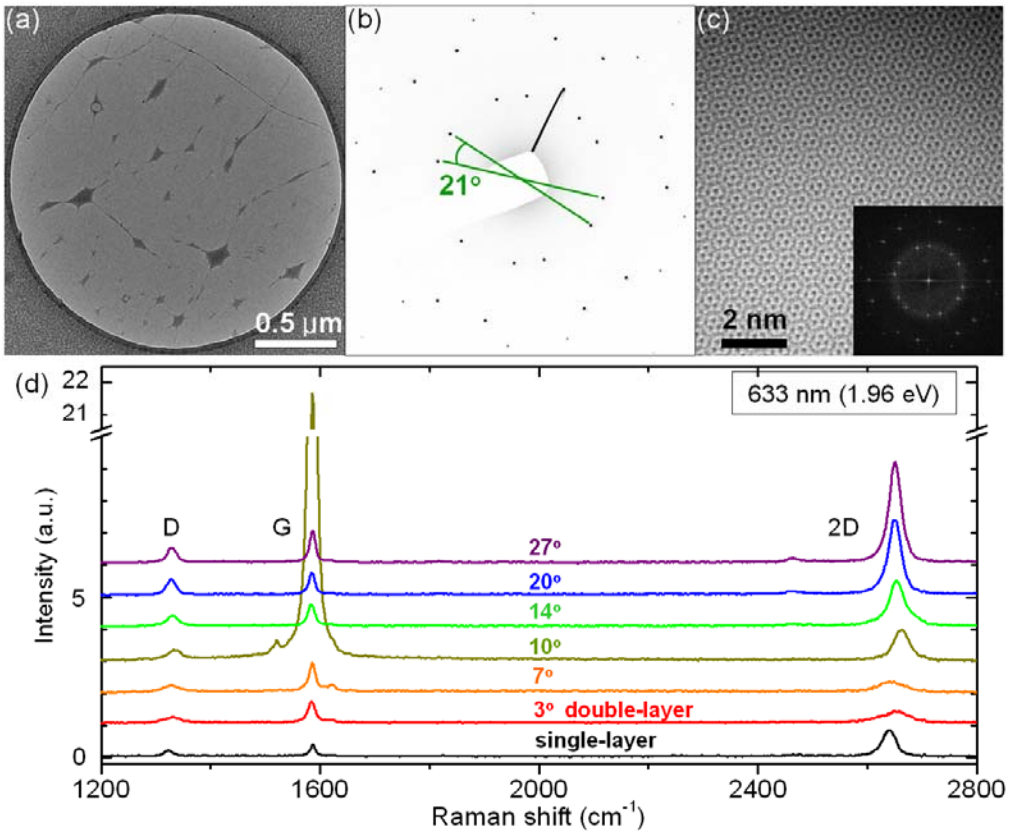

Figure 8.1 Suspended rotated double-layer graphene and Raman spectrum. (a) TEM image of misoriented double layer graphene. The graphene sample is suspended in a hole of 2 um diameter. (b) Diffraction pattern of the graphene sample shown in (a). The two sets of hexagonal patterns are relatively rotated by 21 degrees. An electron beam size of ~ 1 μm is used for diffraction acquisition. (c) Atomic resolution TEM image of double-layer graphene with rotational angle of 21 degree showing a moiré pattern. Inset shows a fast Fourier transform (FFT) of the image. (d) Raman spectra of misoriented double-layer and single layer graphene measured with 633 nm wavelength laser (1.96 eV). The spectra are shifted vertically for clarity.

Fig. 8.1a shows a typical real-space TEM image of double-layer graphene. The sample areas are largely clean and flat. There are also apparent small scattered dark regions, which are not present in single-layer graphene. These dark regions are most likely carbon residues trapped between the two graphene layers and can be used to quickly distinguish double-layer from single-layer graphene regions in our samples. Other than these small residue pockets, the rotated double-layer graphene samples generally have clean interfaces between the two layers, showing clear moiré patterns at the atomic scale (Fig. 8.1c).

For this study, we choose only double-layer graphene specimens where each layer suspended over the hole consists of a single domain. For these samples, two sets of hexagonal

diffraction spots, one from each layer, are obtained, as exemplified in Fig. 8.1b. From the diffraction spots we unambiguously determine the rotation angle between the two misoriented single-crystal layers spanning a hole. We are cautious to avoid samples with tilt grain boundaries [94] or local fold structure from the transfer process [18], which would give more than two sets of hexagonal diffraction spots over the sample area. In contrast to previous Raman studies with folded graphene samples, here we can easily mass-produce rotated double-layer samples with broad coverage of rotation angles (Fig. 8.2). Following TEM analysis, we perform Raman spectroscopy measurements on the indexed rotated double-layers inside the designated holes.

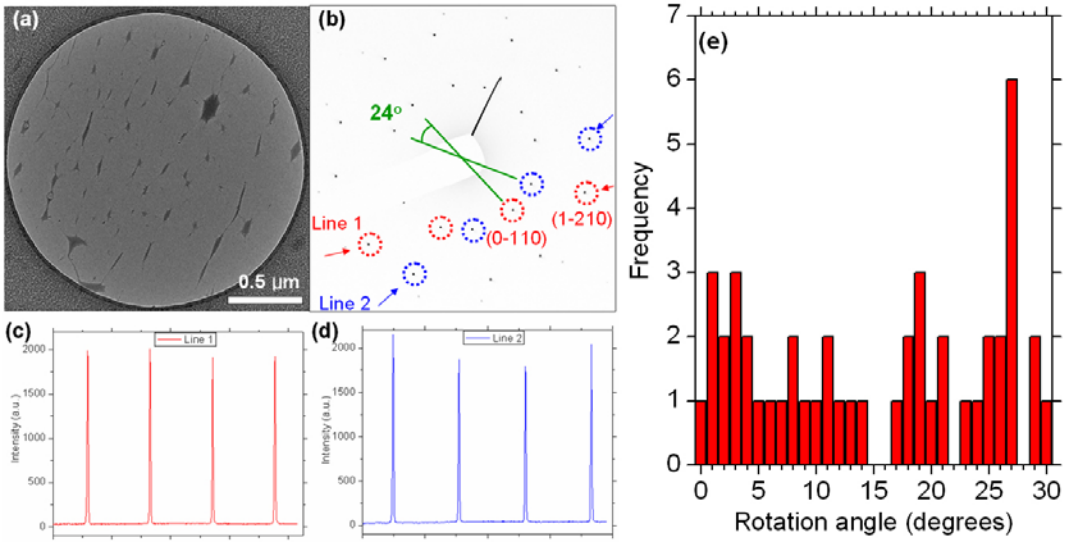

Figure 8.2 TEM imaging and diffraction of double layer graphene. (a) TEM image of double layer graphene. (b) Diffraction patter of the graphene sample shown in Fig a. It shows 24 degree rotation. The arrows indicate the lines for intensity scan for Fig. c and d. The diffraction is acquired with about 1 μm e-beam size. (c) Line intensity of line 1. (d) Line intensity of line 2. (e) Histogram of rotation angles in the studied double-layer graphene samples.

Figure 8.1d shows selected Raman spectra of a misoriented double-layer graphene (having rotation angles of 3, 7, 10, 14, 20, and 27 degrees) and of single-layer graphene. The single-layer graphene shows the typical signature of a 2D/G peak integral intensity ratio around 6, and 2D peak width (FWHM) of 28.7 ± 0.9 cm^{-1}. In the case of rotated double-layer graphene, the data clearly show a change in spectral features from low-angle to high-angle misorientations. Low-angle (<~ 8 degrees, for 633 nm laser wavelength) misoriented double-layers exhibit the Raman signature of a strong coupling between layers. In the high-angle regime (> 13 degrees), the double-layers display Raman spectra closer to those of single-layer graphene. The 2D peak of double-layer graphene is blue-shifted relative to the 2D peak in monolayer graphene, with the blue-shift magnitude depending non-monotonically on the rotation angle. We also observe a strong resonance of the G peak at an intermediate angle (~ 10 degrees). Additionally we find that the peak position and width of G peak are almost angle independent (Fig. 8.3), while the intensity and width of the 2D peak again show quite

complex angle dependence. As we will show later, these observations can be explained by the rotation-angle dependent electronic bandstructure.

We also observe a D peak (two times weaker than G peak), which indicates the presence of defects, most likely introduced by the fabrication process and TEM characterization. Additionally, at certain rotational angles we observe extra peaks around the G peak. These peaks have been investigated in recent studies [169, 170].

We consider here in more detail our experimental results for the G Raman peaks of rotated double-layer graphene. Measured Raman spectra with frequencies close to the G peak are shown in Fig. 8.4a for a single layer and selected rotational angles of double-layer graphene. Compared to single-layer, the double-layer graphene G peak has slightly larger FWHM (2 to 6 cm^{-1}) while the center location shows slight shift (1 to 3 cm^{-1}) towards red. Even though these broadening and red-shifts are more prominent at the very-low angle regimes (< 3 degrees), the rotation-angle dependence is generally very weak (Fig. 8.3). The consistency of the G peak positions throughout the single and double-layer samples demonstrates that double-layer samples do not have significant doping or strain differences from single-layer graphene [161]. Unlike its width and peak position, the G mode intensity at laser wavelength of 633 nm is, however, extremely angle dependent. As shown in Fig. 8.4b we find more than a thirty-fold increase of G peak intensity at 10 and 11 degrees, compared to other angles, where the intensity is largely angle independent.

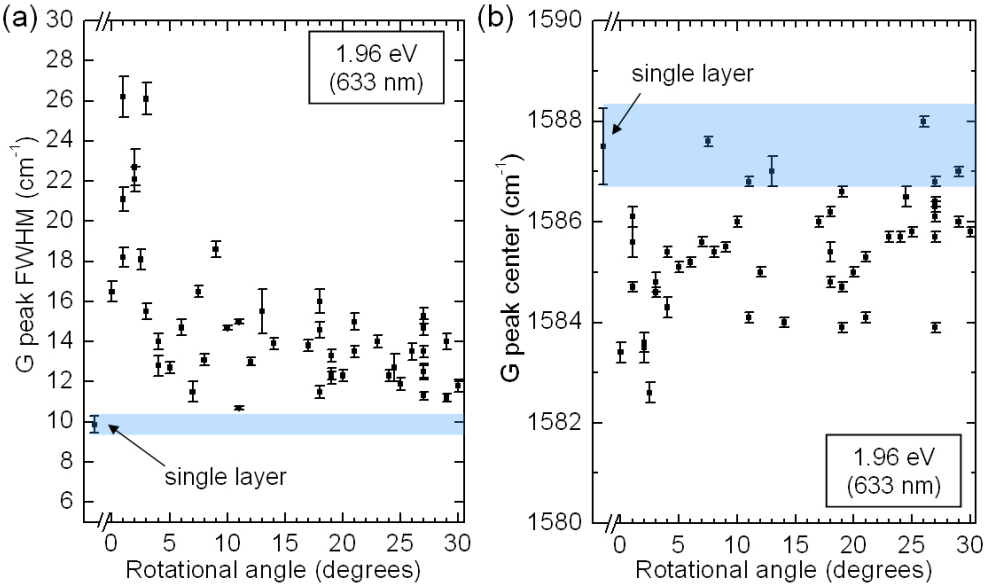

Figure 8.3 Rotational angle dependence of Graphene G peak FWHM and center location measured with 633 nm laser wavelength. (a) Rotated double-layer graphene G peak full-width half-maximum (FWHM). The blue horizontal area represents the value from single layer graphene. (b) Rotated double-layer graphene G peak center location. The blue horizontal area represents the value from single layer graphene.

The graphene 2D Raman peak, which is the most sensitive peak to electronic and phonon band structure changes in graphene [161], exhibits even more complex rotational-

angle dependence. Fig. 8.5a shows the measured Raman spectra around the graphene 2D peak for double-layer and single-layer graphene. The full width at half maximum (FWHM) of the 2D peak is large at small rotation angles and is close to the single-layer values at large angles (Fig. 3b). However, the decrease is not monotonic, and around 7 - 9 degrees we observe an increase in FWHM. The 2D peak position overall shows a blue-shift and is strongly angle dependent (Fig. 8.5c). We find from 0 to 8 degrees a decrease in blue-shift, from 10 to 1 cm^{-1}, followed by a sharp increase to 22 cm^{-1} at 10 degrees. From 10 to 17 degrees, the blue-shift decreases to 11 cm^{-1} and is nearly angle independent at higher angles. We observe that the rotation angle at which there is strongest variation in the 2D peak position coincides with that of the G peak intensity enhancement angle and local increase in 2D FWHM. This implies that these features share a common origin.

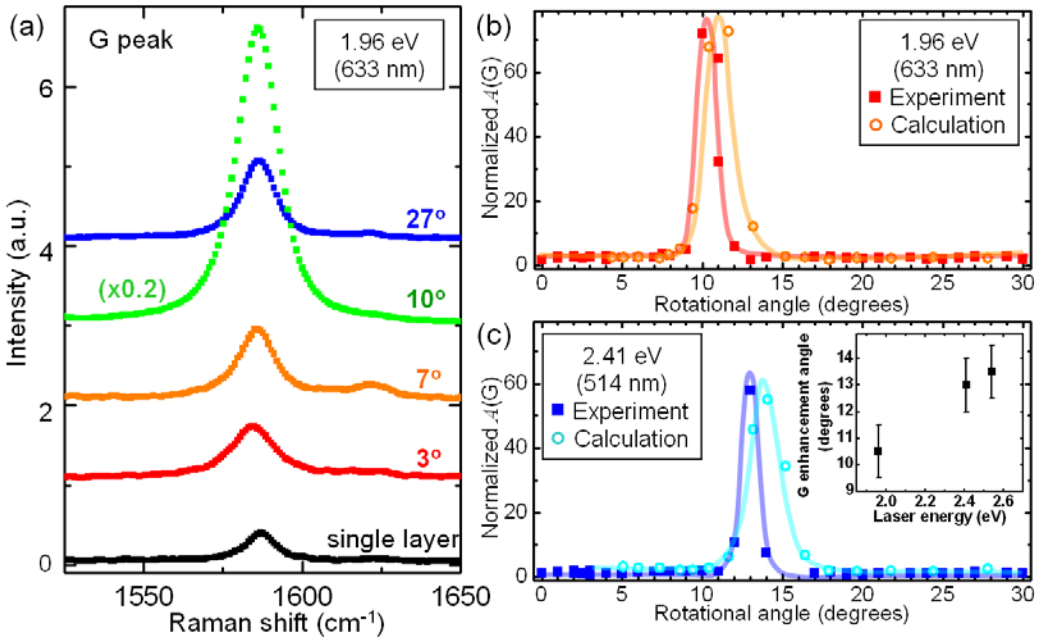

Figure 8.4 Rotational angle dependence of G peak intensity. (a) Graphene Raman G peak for rotated double-layer and single-layer graphene. (b) Dependence of G peak integral intensity (normalized to the single-layer value) on the rotation angle for 1.96 eV (633 nm) laser excitation. The filled and unfilled symbols show experimental and theoretical calculation values respectively. The lines are guides to the eye. (c) G peak integral intensity with 2.41 eV (514 nm) laser excitation. The inset shows measured dependence of critical angle on laser energy.

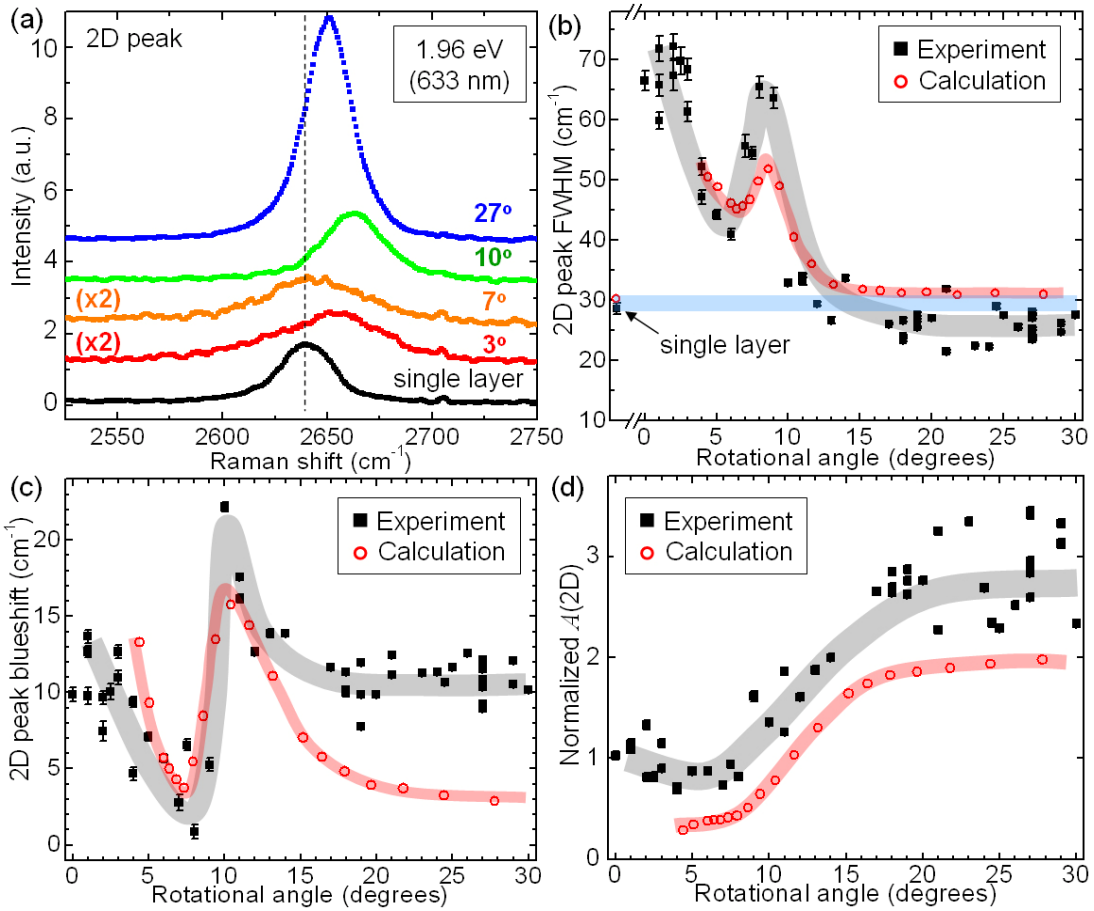

Figure 8.5 Rotational angle dependence of Raman 2D peak. (a) Graphene 2D peak for rotated double-layer and single-layer graphene. The vertical dashed line represents the center of single layer 2D peak. (b) Rotated double-layer graphene 2D peak FWHM. We have fitted the 2D peaks with a single Lorentzian peak for simplicity. The black squares and red circles are the experimental and theoretical calculation values. The blue horizontal area represents the experimental value from single layer graphene. The grey (experiment) and red (calculation) areas are guides to the eye. (c) Rotated double-layer graphene 2D peak blue-shift in respective to the value from single layer graphene. (d) Integral intensity of 2D peak. Experimental and calculation values were normalized to the single-layer value.

The measured 2D intensity also shows a dramatic change with respect to rotation angles (black square data in Fig. 8.5d). For non-interacting double-layer graphene, one would expect twofold increase in the 2D peak intensity as compared to the single-layer graphene. In the low angle regime (< 10 degrees), however, the integral intensity of the 2D peak is nearly 50 % reduced compared to what would be expected for the non-interacting double-layer graphene. In the middle range, the intensity shows the increasing trend and finally above 17 degrees become similar to or greater than two times the value in single layer graphene.

In order to achieve a more complete understanding of rotation angle dependence of double-layer graphene Raman features, we turn to a theoretical analysis of the Raman spectrum as a function of rotational angle (supplementary materials). We first consider a

simplified band structure analysis that accounts for the existence of the experimentally observed critical misorientation angle; we then perform the tight binding calculation of Raman spectrum in the entire range of misorientation angles.

In momentum space, for two noninteracting layers misoriented by angle θ, the respective momentum space Brillouin zones (BZ) of the top and bottom graphene layers are rotated by θ as shown in Fig. 8.6a. Band structure modifications occur mostly where the Dirac cones of top and bottom layers are overlapping. Fig. 8.6b shows the simplified electronic band-structure in the vicinity of the overlap of these two Dirac cones. In this region, the density of states (DOS) of double layer graphene is modified from non-interacting graphene, exhibiting Van Hove singularities as shown in Fig. 8.6c [106]. The energy difference between conduction and valence Van Hove singularities scales with the rotational angle and can reach the energy of a few eV at the optical range in the case of higher rotational angles.

For a given Raman excitation laser energy E_{laser}, we calculate a critical rotational angle θ_c where the energy between the conduction and valence Van Hove singularities equals E_{laser}. Using the Dirac dispersion relation of monolayer graphene, the critical angle can be calculated as

$$\theta_c = \Delta k / K = {3aE_{laser}}\Big/{\hbar v_f 4\pi} \tag{8.1}$$

where a is the lattice parameter of graphene (2.46 Å), $\hbar$ is the reduced Planck's constant, and v_f is the Fermi velocity in monolayer graphene (10^6 m/s). In the case of a 633 nm laser excitation (1.96 eV), we find $\theta_c = 10^o$, in excellent agreement with $\theta_c = 10^o$ determined experimentally (Fig. 8.6b). Therefore, we expect that for double-layer graphene with rotational angle close to θ_c, the Raman spectra at corresponding laser energy E_{laser} will be strongly affected by the coupling between top and bottom graphene layer. Furthermore, we expect that for angles larger than θ_c Raman spectra will resemble those of a single layer graphene since all the optical excitation occurs in an isolated simple Dirac cone structure (intervalley 2D scattering process for such a case is shown as blue lines in Fig. 8.6e). On the other hand, for angles smaller than θ_c we expect Raman spectra quite different from those of single layer graphene, since the closeness of the Dirac cones from the top and bottom layers in momentum space allows for scattering paths significantly different from those of the monolayer (black lines in Fig. 8.6e).

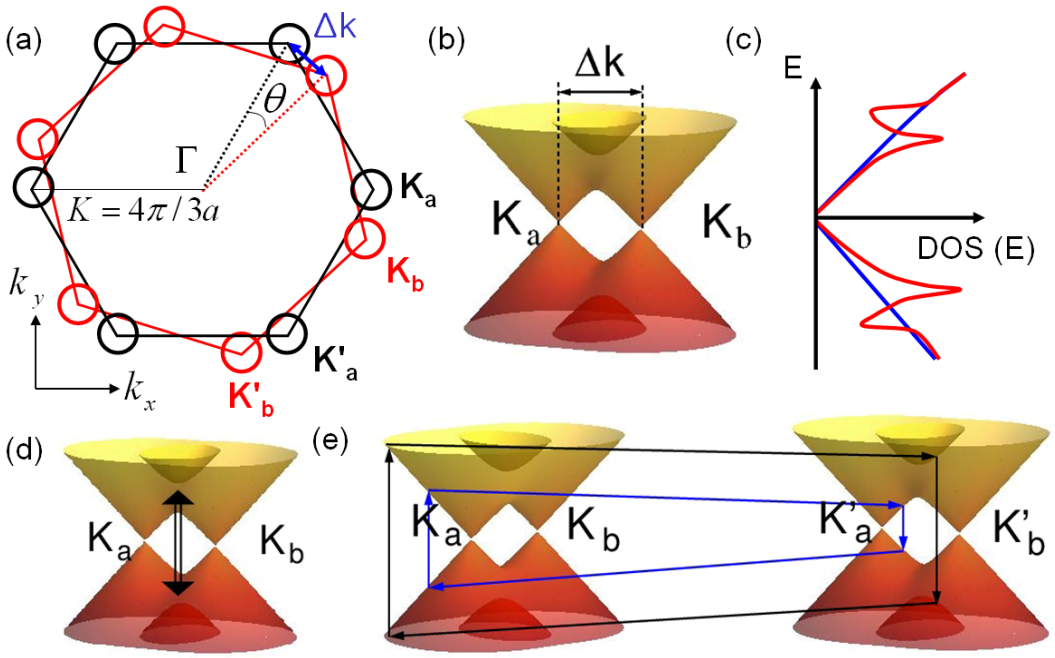

Figure 8.6 Electronic band-structure and Raman scattering processes in rotated double-layer graphene. (a) Brillouin zone (BZ) of rotated double-layer graphene misoriented by θ. The circles represent the locations of Dirac cones from the first (black) and second (red) layer. The distance between two near-by Dirac cones is Δk. (b) Energy dispersion relation in the vicinities of two Dirac cone overlap. Van Hove singularities are induced from band-overlap between two Dirac cones. (c) Sketch of energy dependence of density of states (DOS) near the Fermi level of rotated double-layer graphene without (blue) and with interlayer interactions (red). DOS exhibit distortions from the interlayer interactions showing Van Hove singularities. (d) Some processes that contribute to the Raman G peak amplitude. (e) Intervalley 2D Raman scattering processes for rotated double-layer graphene in which the laser excitation energy is smaller (blue lines) or larger (black lines) than the energy difference between conduction and valence Van Hove singularities.

Although the simple model utilized above correctly accounts for the observed critical rotation angle, it cannot provide a satisfactory quantitative explanation of the detailed Raman peak intensities observed experimentally (especially below critical mismatch angles) and a more complete theoretical approach is needed. We therefore perform tight-binding calculations of Raman spectra in double-layer graphene for a series of commensurate structures, with varying rotational angles. We compute the Raman spectrum by standard perturbation expansion [161] in the electron-photon and electron-phonon interaction. To construct tight-binding models for a rotated double-layer graphene at arbitrary θ, we use Slater-Koster parameters fitted to density functional theory (DFT) calculation of rotated graphene [108]. We also rescale all tight-binding hopping parameters by 18% in order to account for GW computed correlation effects [171-173]. For electron linewidth we use constant value of 190 meV (half width at half maximum) in order to reproduce correctly the amount of G-peak enhancement at the critical angle. We expand the electron-photon and electron-phonon interaction to nearest neighbor carbon atoms. Unlike the electronic structure, which we compute for each rotational angle, we assume that the phonon band structure is

unchanged going from single to double-layer graphene (supplementary info).

The computed Raman G and 2D peak features are consistent with the observed experimental trends. The calculated G peak intensity (red circles in Fig. 8.4b) shows that the critical angle agrees with the experimentally observed value. Our calculations show that the main contribution to the G peak enhancement arises from resonant electron-hole excitations near the Van Hove singularities (Fig. 8.6d) as one would expect from our simple model based on critical mismatch angle.

Computed values (red circles in Fig. 8.5) of 2D Raman spectra also agree well with experimentally obtained results, which confirms that the systematic trend in the behavior of the 2D Raman peak originates from the changes in the electronic structure of rotated double-layer graphene. In order to further elucidate the origin of the 2D Raman features, we perform Raman spectrum calculations in which the effects of interlayer coupling are included only in the electron wavefunctions or only in the electron band energies. We find that double-layer interaction only in the electron band energies is enough to explain the dependence of the 2D Raman peak position on the rotational angle. Since the main change in electron band energies is associated with the opening of the gap, leading to before mentioned Van Hove singularities, we conclude that dependence of 2D peak position on the misorientation angle is a measure of location of the Van Hove singularities. The origin of the increased 2D FWHM and decreased intensity at the low misorientation angle regime is much more complex since the effect of interaction between layers on electron wavefunctions becomes important as well as the occurrence of constructive and destructive interference between various Raman scattering pathways. We have also performed a continuum model study of the Raman spectroscopy of rotated bilayers, using the reduced Hilbert space of Refs. [107, 154]. The FWHM, peak position and intensity of the 2D Raman peak in the continuum model study show similar trends as those in the tight-binding model, thus re-enforcing our physical picture obtained here.

The standard Raman signature of single-layer and AB-stacked bilayer graphene [163, 164] has been widely used to characterize chemically synthesized graphene samples where rotational stacking is common [30, 31]. The present study shows that the usual Raman method for assignment of layer number should be applied with caution for rotationally stacked graphene samples. Moreover, our study provides a convenient way to deduce the rotational angle in double-layer graphene. From the combined information of the 2D peak width, 2D peak location, and the 2D/G intensity ratio, one can deduce the general rotational angles in double layer graphene samples. Furthermore, using different laser excitation energies allows tuning of the critical transition angles (Figure 8.7 and 8.8).

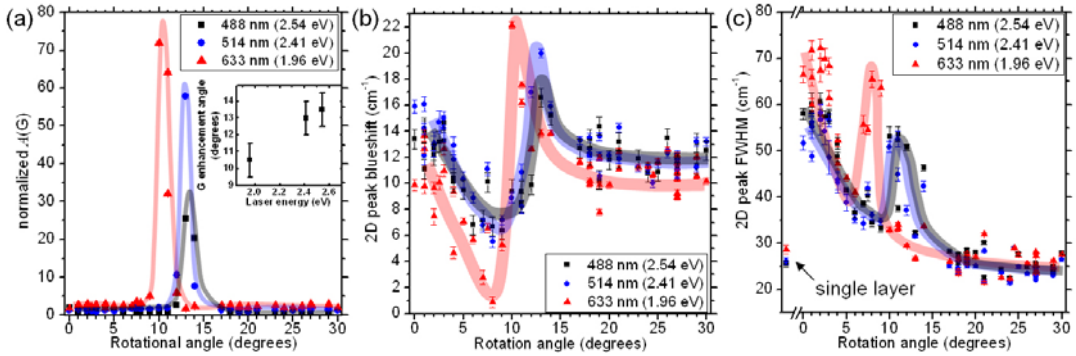

Figure 8.7 Experimental Raman data on rotated double-layer graphene with different laser wavelengths. The general features in the data are shifted to higher rotational angles with higher laser energies. (a) G peak intensity depending on the rotation angle. Intensities were normalized to the single-layer value for each laser wavelength. The inset shows the laser energy dependence of rotational angles with G enhancement. (b) 2D peak blue-shift depending on the rotation angle compared to single-layer graphene values. (c) Graphene 2D peak FWHM depending on the rotation angle.

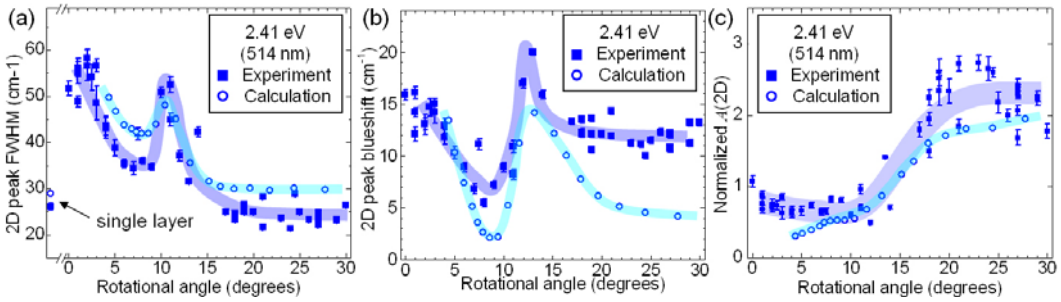

Figure 8.8 Rotational angle dependence of Raman 2D peak with 514 nm laser wavelength (2.41 eV). (a) Rotated double-layer graphene 2D peak FWHM. The squares and circles are the experimental and theoretical calculation values. The blue (experiment) and bright blue (calculation) lines are guides to the eye. (b) Rotated double-layer graphene 2D peak blue-shift with respective to the value from single layer graphene. (c) Integral intensity of 2D peak. Experimental and calculation values are normalized to the single-layer value.

Chapter 9
Graphene nanoribbons obtained by electrically unwrapping carbon nanotubes

Graphene nanoribbons (GNRs) are attractive candidates for nanoelectronics, spintronics and nanoelectromechanical systems (NEMS) [16, 174-184]. Lithographic and chemical methods have been used previously to produce GNRs from layered graphite or suitably prepared graphene [16, 174-176]. Alternatively, GNRs have been produced from multi-wall carbon nanotubes (MWNTs) using chemical oxidation, argon plasma etching, intercalation, or metal particle-assisted unzipping [179-184]. High-quality (typically arc-grown) MWNTs are attractive starting materials as they display excellent current carrying capacity indicative of low defect concentration [185, 186]. Interestingly, nanoribbons derived from collapsed carbon nanotubes were reported already in 1995 [113]. Employing MWNTs or single-wall nanotube (SWNTs) with narrow diameter distributions, unzipping approaches offer the possibility of large-scale production of narrow GNRs with well-controlled widths. Unfortunately, available unzipping methods have serious drawbacks related to surface contamination and introduction of structural defects, resulting in mechanical and electrical degradation [179-184]. Highly desirable would be a MWNT unwrapping method with no reliance on harsh chemical or other detrimental treatment, with the ability to preserve (or even enhance) the quality of the MWNT fabric. Electrical current-induced unwrapping of MWNTs for GNR production is an interesting approach to this requirement.

At very high electrical bias, MWNTs can display superplasticity [187, 188], or undergo structural failure through concentric wall-by-wall breakdown or blow-out with associated staircase-like current drops [185, 186, 189, 190]. In vacuum, this breakdown is believed to be driven by resistive heating and thermal bond breaking (as opposed to oxidation, as might occur during blow-out in air [185]). Evidence for graphene flake production from MWNTs using high dc pulses has been recently reported [191].

In this chapter we apply the technique of current-induced electrical breakdown of MWNTs to produce GNRs. The key is to avoid the typical catastrophic wall blow-out, but instead promote controlled thermally-induced unwrapping of the outer walls of the nanotube. Using *in situ* transmission electron microscopy (TEM), we also characterize GNRs structurally and electrically, including situations for which the GNR is severely mechanically flexed. GNRs derived from this method have high current-carrying capacity, which demonstrates that this is a promising technique for obtaining high quality GNRs from MWNTs.

Experiments are carried out inside a JEOL 2010 transmission electron microscope (TEM) operated at 100 keV, employing a nanomanipulation platform (Nanofactory Instruments AB). We choose this low acceleration voltage to minimize electron beam damages to MWNTs and GNRs. Arc-grown MWNTs are attached to an aluminum wire using conductive epoxy and the wire is then mounted to the stationary side of the holder. An etched

tungsten probe is mounted to the opposite mobile side of the holder. Although the bare tungsten probe can itself serve as the mobile electrode, typically this electrode is first coated with a bundle of MWNTs or amorphous carbon-MWNT composite which facilitates carbon-carbon contact between the mobile electrode and the MWNT to be unwrapped. The probe is moved such that the mobile electrode touches the tip of a MWNT on the wire, creating a carbon-MWNT contact. A stable electrical and mechanical contact at the junction is established by annealing with high current. The sliding process between MWNT core and shell/GNR is maintained at a rate of 1 – 10 nm/sec. A Keithley 2400 SourceMeter is used for electrical bias and current readout across the MWNT. Five nanotubes have been unwrapped using this electrical breakdown method.

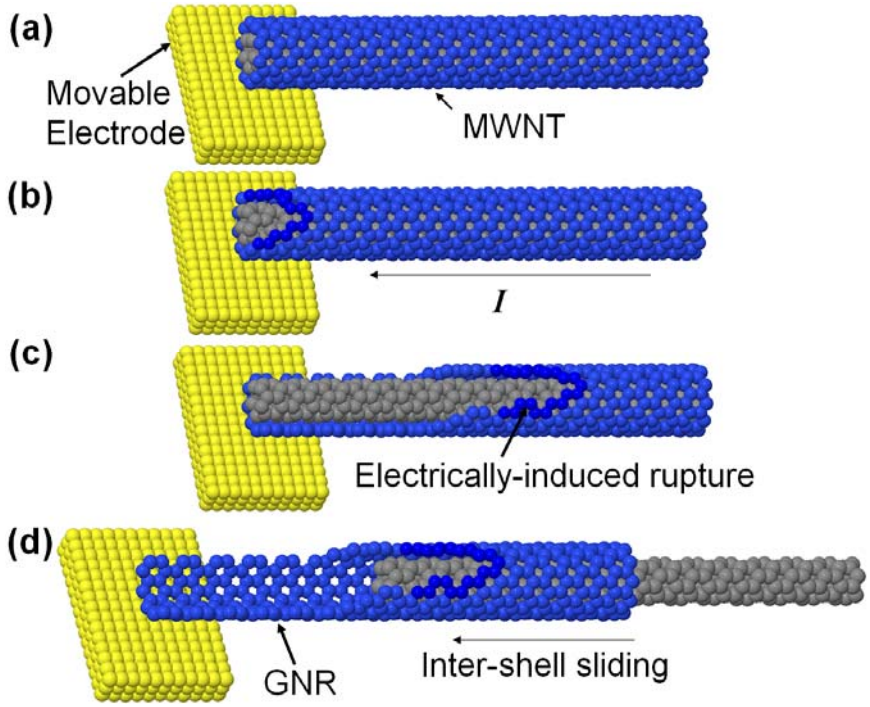

Figure 9.1 Schematic drawings of the proposed graphene nanoribbon (GNR) fabrication from a multi-wall carbon nanotube (MWNT). In the schematic, a double wall carbon nanotube (DWNT) is chosen for simplicity. (a) MWNT before the partial wall rupture. (b) Electrical current induces rupture of the outer wall of a MWNT. (c) Partial outer wall rupture of a MWNT results in a precursor GNR which is under the MWNT inner core. (d) Inter-shell sliding between the GNR and the inner core results in a suspended, electrically contacted GNR.

Figure 9.1 shows schematic drawings of the proposed fabrication process of extracting a GNR from a MWNT. Using a movable electrode, a MWNT is contacted and unwrapping of the outer walls is induced *via* an applied electrical current through the contact and tube. With proper voltage bias control, only part of the MWNT outer wall (upper portion in the schematic) is severed and, as shown in Fig. 9.1c, a precursor GNR is created which clings to the remaining MWNT inner core. The GNR is then systematically removed from the

MWNT *via* sliding between the GNR and the MWNT inner core, as shown in Fig. 9.1d. The newly formed GNR can easily be completely removed from the MWNT, or, most importantly, the sliding process can be terminated when a desired amount of GNR has been slid off. This leaves a pre-selected length of GNR fully suspended in vacuum, with each end electrically and mechanically attached to a conducting electrode (the remaining portion of the MWNT serves as one electrode).

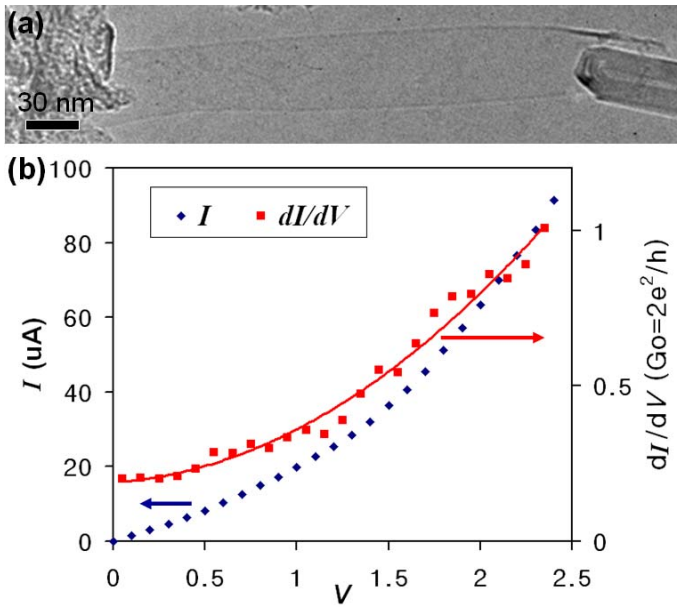

Figure 9.2 TEM images and electrical transport measurement of a GNR derived from a MWNT. (a) TEM image of a GNR derived from a MWNT *via* the electrical rupture and unwrapping method. The original MWNT from which the GNR is derived is shown on the right side; it continues to serve as a mechanical support and electrical contact for the GNR. (b) Electrical transport measurement of the same GNR. The blue diamond and red square dots (color online) are the electrical current and differential conductance at given voltages, respectively. The solid line is a guide to the eye for the differential conductance. At low voltages (< 0.5 V), the response is linear. With higher bias, the conductance increases with increasing bias.

Figure 9.2a shows a TEM image of a GNR experimentally derived from a MWNT using the electrical-current-induced unwrapping technique. The GNR is fully suspended in vacuum, with each end electrically and mechanically attached to a conducting electrode. The original MWNT (30 nm diameter) from which the GNR is derived is located on the right side of the GNR. The length of the GNR is about 300 nm and the width, uniform along the ribbon axis, is 45 nm, suggesting about half (circumferentially) of the MWNT outermost shells were vaporized during the electrical unwrapping process. The proposed unwrapping of MWNTs is a very fast process and the intermediate steps of it were not observed in our TEM experiments due to spatial and temporal limitations. However, this is a very likely scenario and supporting

evidence for this unwrapping of MWNTs is documented in Fig. 9.5. Related modeling of the thermally-induced nanotube wall-rupture mechanism is also discussed later in this article and the supporting information. The edge of the GNR in Figure 9.2a could not be resolved at the atomic scale, posing the possibility that this structure is a collapsed nanotube. Considering that a collapsed nanotube is within the GNR family, we use the term GNR for this structure [113]. In Figure 9.2b, the two-terminal electrical transport for the same GNR is shown. The blue diamond and red square dots are respectively the electrical current and differential conductance at given bias voltages. At low bias voltages (< 0.5 V), the response is mostly linear, while at higher voltages the conductance increases with increasing bias voltage, similar to the behavior observed in MWNT two-terminal electrical transport measurements [189].

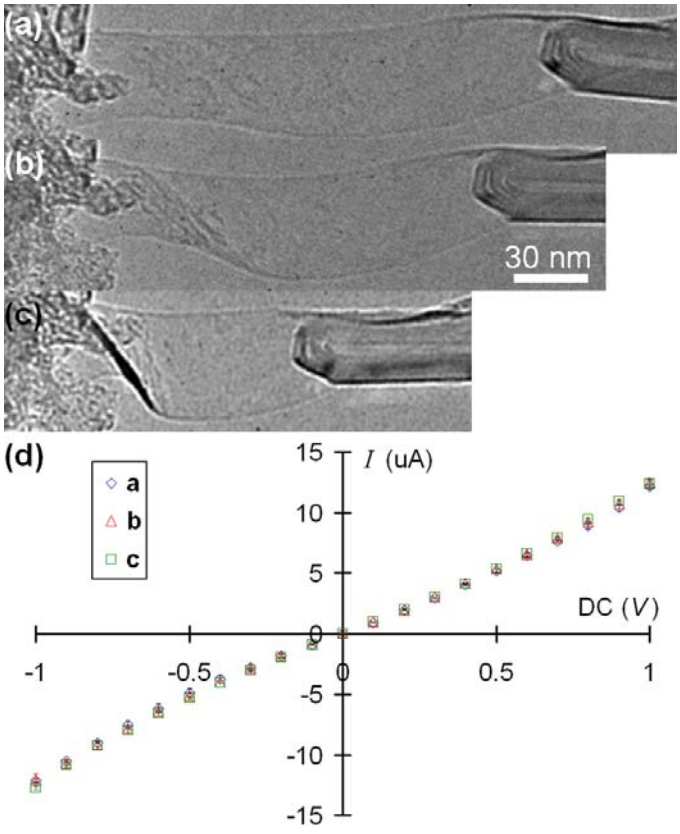

Figure 9.3 Flexing of a GNR and concurrent electrical measurement. (a-c) Sequential TEM images during the flexing process. (d) I-V curves for corresponding flexed states (figures a - c) of the GNR. The two-terminal conductance stays the same even with the dramatic mechanical deformation of the GNR.

Graphene and GNRs have remarkable mechanical properties [12, 15, 16, 19] which make them promising materials for NEMS and flexible devices. To exploit graphene and GNRs for electromechanical purposes, it is crucial to characterize electrical transport under mechanical deformation conditions, but there have been few studies on this subject. The

conductance of graphene films has been observed to drop reversibly when the films are subjected to bending or stretching [19]. The GNR isolation and mounting configuration described here affords highly controlled reversible flexing and simultaneous electrical measurement of a single GNR. Figures 9.3a-c show a series of TEM images acquired during a mechanical deformation of the GNR. Clearly, the GNR shows dramatic distortions as the MWNT electrode is moved to the left, closing the gap between the electrodes. As the degree of flexing is changed, concurrent two-terminal electrical transport measurements are performed. Figure 9.3d shows I-V curves for each deformation state (a-c) of the GNR. The main result is that the two-terminal resistance remains constant even with dramatic flexing of the GNR. This indicates that conductivity of GNRs (and presumably properly mounted graphene) can be maintained even under severe mechanical deformations such as high angle flexing. These results would also imply that rippling, which can occur on suspended graphene [17], does not substantially modify the intrinsic electrical transport properties of graphene or its derivatives.

The ultimate current-carrying capacity of GNRs, and their failure mode under extreme bias conditions, is of great interest. We find that suspended GNRs can carry large currents without failure. For the specimen of Figure 9.2, a maximum two-dimensional current density of ~ 22 A/cm is obtained, comparable to that found for exfoliated graphene on a substrate [192, 193]. Notably, the GNR is here suspended in vacuum, and thus the central portion is not well thermally anchored and presumably at elevated temperature. This suggests an even higher ultimate current limit is possible for thermally anchored GNRs.

Figure 9.4 shows the results of a suspended GNR intentionally driven to electrical failure. TEM images of the GNR and corresponding transport data are shown. As seen in Figure 9.4c, the GNR is stable and the current remains constant (~ 100 μA) for an applied bias of 2.5 V. As the bias is increased to 2.6 V, the current begins to drop and the middle part of the GNR diminishes in width (Figure 9.4a). With fixed bias, the current asymptotically approaches ~65 μA as shown in Figure 9.4c. During the GNR breakdown, no staircase-like current drops are observed, indicating no dramatic "quantized" geometrical configurations; the GNR width gradually and smoothly diminishes. As the electrical bias is increased to ~ 3 V, the GNR fails catastrophically at the central part and current drops to zero, as shown in Figure 9.4b. The breakdown mechanism of the GNR under high bias is likely due to carbon atom sublimation from the GNR edges due to high temperatures [149, 194]. Related current-induced "shrinking" of carbon nanotubes has been reported [195].

We now examine in more detail the electrically-induced MWNT rupture and unwrapping mechanism that leads to GNR formation. The key is the asymmetric electrode contact at the tip of the MWNT. This side-contacting results in asymmetric electrical and thermal transport conditions near the tip of the MWNT. Most notably, this results in a sharp temperature difference between the non-contacted and contacted outer surfaces of the MWNT near its tip. The non-contact side of the MWNT tip achieves a higher temperature than the contact side, and this is where the unwrapping (ejection of carbon atoms) is initiated. The asymmetric breakdown process is documented in Figure 9.5. Figures 9.5a-e show a series of TEM images for the asymmetric side-contact condition. At the bottom of the MWNT tip, amorphous carbon and MWNT composite serves as an electrode. As the bias on the MWNT is increased, the onset of MWNT shell breakdown occurs, as shown in Figures 9.5b-c. The non-contact side of the MWNT tip experiences faster electrical breakdown. Along with the

breakdown, the inner core shells of the MWNT easily slide with respect to the outer shells, as shown in Figure 9.5d, due to thermal agitation. The contact side of the MWNT tip in Fig. 9.5d has more intact layers (eight layers) than the non-contact side (two layers), as indicated by the arrows, which shows clearly that the wall breakdown occurs faster in the non-contact side. MWNT walls at the contact side, which do not have corresponding walls at the other side, readily evolve to low-curvature strips with edges, i.e. GNRs. In Figure 9.5e, the inner core of the MWNT can be seen displaced left with respect to the outer shells. The GNR structures are now nearly isolated.

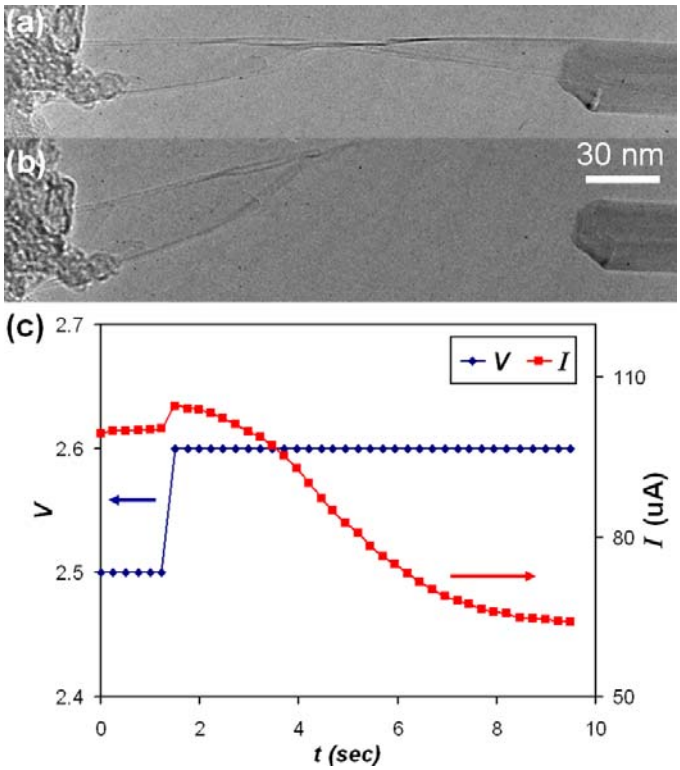

Figure 9.4 Electrical breakdown of a GNR. (a) TEM image of a GNR after partial electrical breakdown. The central part of the GNR has shrunk which implies diffusive electrical transport processes along the GNR. (b) TEM image of the GNR after total breakdown. (c) Voltage and current variation in time during the electrical breakdown. Stable two-dimensional maximum electrical current density is about 22 A/cm. The lack of a staircase-like current drop suggests that the GNR undergoes gradual, not quantized, breakdown.

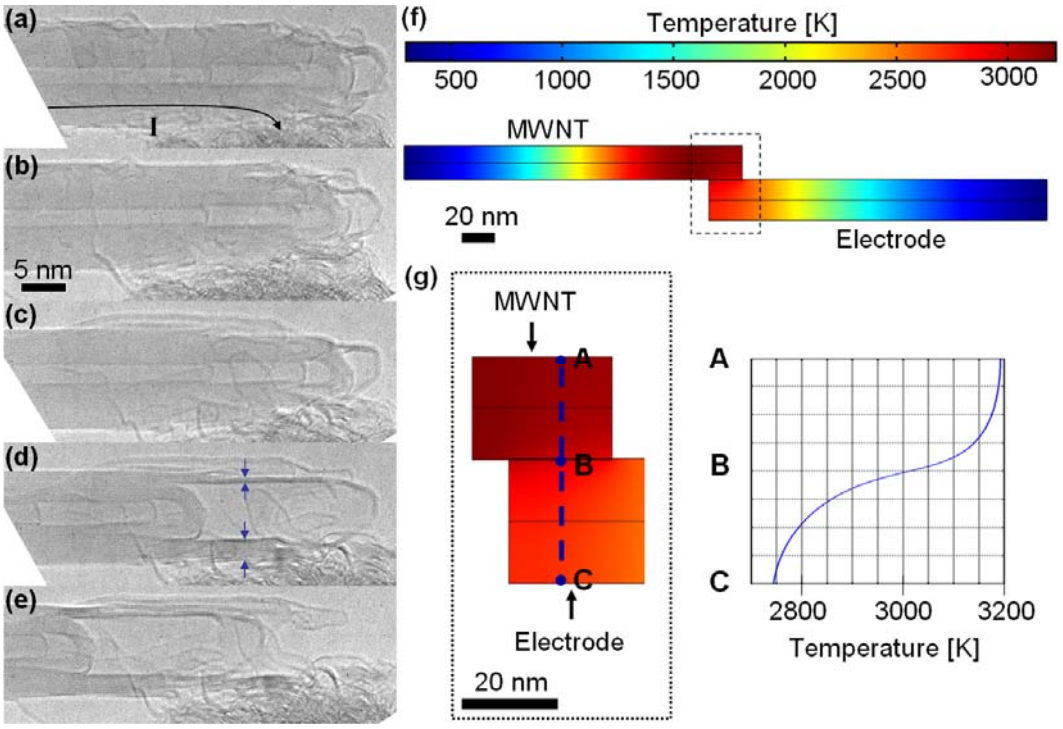

Figure 9.5 Asymmetric rupture of outer shells of a MWNT. (a-e) Sequential TEM images of an asymmetric rupture of MWNT outer shells. (a) Electrical current passes though the MWNT. At the bottom of the MWNT tip, MWNTs and amorphous carbon composite serve as an electrode. (b-c) MWNT walls start to undergo an electrical rupture. The non-contacted side of the MWNT tip ruptures first. (d) The inner core of MWNT slides to the left with respect to the outer shells. In the outer shells, it is clear that the contact side of the tip has more layers (eight layers) than the non-contact side (two layers). (e) The inner core of the MWNT slides farther with respect to the outer shells. Around the MWNT tip, a GNR-like structure appears. (f) Temperature profile of a MWNT and an electrode contacting the side of the tip from finite element analysis. Due to Joule heating, the area near the MWNT-electrode contact generally has a higher temperature than other parts of the system, reaching temperatures above 3000 K. (g) Zoomed-in image and temperature profile of the MWNT tip contact region. Temperature profile along line ABC shows that the non-contact side of the MWNT reaches higher temperatures than the contact side because the electrode acts as a heat sink.

We carry out finite element analysis on a side-contact MWNT geometry to quantify the asymmetric temperature distribution at the MWNT tip. We use COMSOL Multiphysics, a commercially available finite element modeler (http://www.comsol.com/). To simulate the side contact to a MWNT, we have used two MWNTs touching each other's tips as shown in Figure 9.6. The MWNT with a bigger diameter (24 nm) is serving as an electrode in the simulation. The heat equation incorporating the Joule heating component, $\nabla \cdot (\kappa(T) \nabla T) + \rho J^2 = 0$, has been employed in the simulation, where $\kappa(T)$ is the temperature-dependent isotropic thermal conductivity, T is temperature, ρ is resistivity, and J is current density. High temperature thermal conductivity $\kappa(T)$ of a MWNT is assumed to be $\kappa(T) = 1/(\alpha T + \beta T^2)$ with $\alpha = 4.8 \times 10^{-6}$ m/W and $\beta = 4.3 \times 10^{-10}$ m/W·K (values adapted from G. E. Begtrup, *et al.* [147]). Isotropic resistivity $\rho = 2 \times 10^{-6} \Omega \cdot$m of a MWNT is adapted from T. D. Yuzvinsky *et al*. [190].

As a boundary condition, the temperatures on the left and right edges of the system are maintained at room temperature (300 K). And an electrical bias V is applied between these two edges. On the other surfaces, a boundary condition with radiation heat exchange and electrical insulation is incorporated. For a given electrical bias V, we can solve the electrostatic equation and get the current density J in the system. Using the heat equation and boundary conditions, we obtain a temperature profile in the system. To establish the highest temperatures in the system at 3200 K, which is the proposed breakdown temperature of a MWNT [147], we adjust the electrical bias V to the proper value.

Figure 9.5f shows the simulated temperature profile of a MWNT and an electrode contacting the side of the MWNT tip. Due to Joule heating, the area near the MWNT-electrode contact generally has a higher temperature than other parts of the system, reaching temperatures above 3000 K. A close look at the temperature profile of the MWNT tip shows that the non-contact side reaches higher temperatures than the contact side (Figure 9.5g). This results from the electrode serving as a heat sink. The width of the MWNT wall segment that is above the critical temperature for carbon sublimation (approximately 3200 K [147]), along with MWNT outer circumference, dictates the final GNR width.

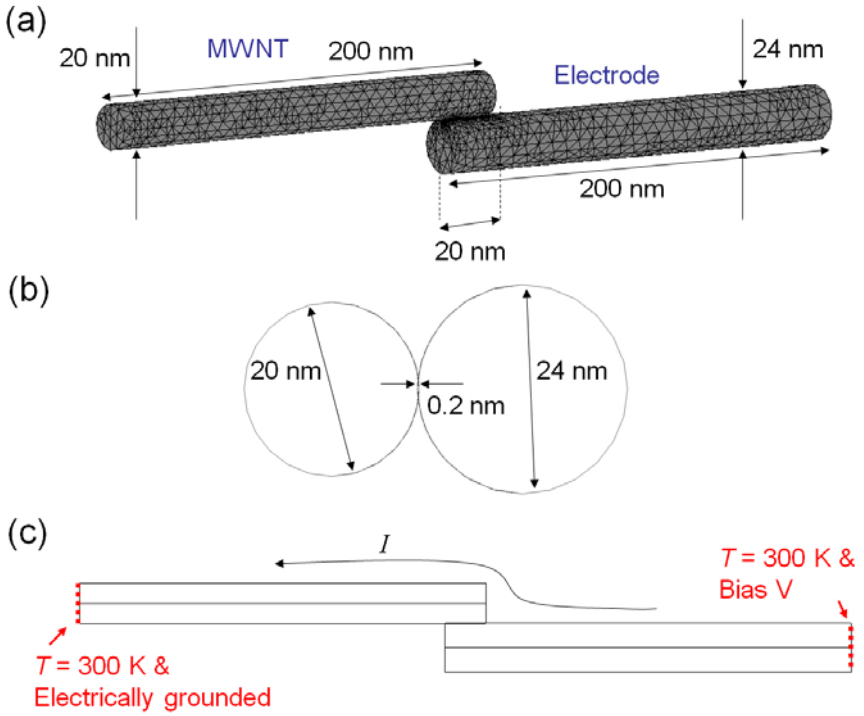

Figure 9.6 Geometry of finite element analysis simulation. (a) The geometry of two MWNTs (with 200 nm length) touching each other's tips. A MWNT with bigger diameter (24 nm) is serving as an electrode. There is a 20 nm overlap along the length between the MWNT and the electrode. (b) The side view of the geometry. The overlap between the MWNT and the electrode is 0.2 nm in the simulation. (c) The boundary conditions of the simulation. At the left and right edges, the temperatures are maintained at room temperature, 300 K, and an electrical bias is applied between these two edges.

Bibliography

[1] K. S. Novoselov, A. K. Geim, S. V. Morozov, D. Jiang, Y. Zhang, S. V. Dubonos, I. V. Grigorieva, A. A. Firsov, Electric field effect in atomically thin carbon films. *Science* **306**, 666-669 (2004).

[2] P. R. Wallace, The Band Theory of Graphite. *Phys. Rev.* **71**, 622-623 (1947).

[3] K. S. Novoselov, A. K. Geim, S. V. Morozov, D. Jiang, M. I. Katsnelson, I. V. Grigorieva, S. V. Dubonos, A. A. Firsov, Two-dimensional gas of massless Dirac fermions in graphene. *Nature* **438**, 197-200 (2005).

[4] Y. B. Zhang, Y. W. Tan, H. L. Stormer, P. Kim, Experimental observation of the quantum Hall effect and Berry's phase in graphene. *Nature* **438**, 201-204 (2005).

[5] A. H. Castro Neto, F. Guinea, N. M. R. Peres, K. S. Novoselov, A. K. Geim, The electronic properties of graphene. *Rev. Mod. Phys.* **81**, 109-162 (2009).

[6] K. I. Bolotin, K. J. Sikes, Z. Jiang, M. Klima, G. Fudenberg, J. Hone, P. Kim, H. L. Stormer, Ultrahigh electron mobility in suspended graphene. *Solid State Commun.* **146**, 351-355 (2008).

[7] P. Blake, E. W. Hill, A. H. Castro Neto, K. S. Novoselov, D. Jiang, R. Yang, T. J. Booth, A. K. Geim, Making graphene visible. *Appl. Phys. Lett.* **91**, 063124 (2007).

[8] R. R. Nair, P. Blake, A. N. Grigorenko, K. S. Novoselov, T. J. Booth, T. Stauber, N. M. R. Peres, A. K. Geim, Fine Structure Constant Defines Visual Transparency of Graphene. *Science* **320**, 1308 (2008).

[9] F. Wang, Y. B. Zhang, C. S. Tian, C. Girit, A. Zettl, M. Crommie, Y. R. Shen, Gate-variable optical transitions in graphene. *Science* **320**, 206-209 (2008).

[10] M. Liu, X. Yin, E. Ulin-Avila, B. Geng, T. Zentgraf, L. Ju, F. Wang, X. Zhang, A graphene-based broadband optical modulator. *Nature* **474**, 64-67 (2011).

[11] F. Bonaccorso, Z. Sun, T. Hasan, A. C. Ferrari, Graphene photonics and optoelectronics. *Nature Photon.* **4**, 611-622 (2010).

[12] C. Lee, X. D. Wei, J. W. Kysar, J. Hone, Measurement of the elastic properties and intrinsic strength of monolayer graphene. *Science* **321**, 385-388 (2008).

[13] D. A. Dikin, S. Stankovich, E. J. Zimney, R. D. Piner, G. H. B. Dommett, G.

Evmenenko, S. T. Nguyen, R. S. Ruoff, Preparation and characterization of graphene oxide paper. *Nature* **448**, 457-460 (2007).

[14] M. A. Rafiee, J. Rafiee, I. Srivastava, Z. Wang, H. H. Song, Z. Z. Yu, N. Koratkar, Fracture and Fatigue in Graphene Nanocomposites. *Small* **6**, 179-183 (2010).

[15] J. S. Bunch, A. M. van der Zande, S. S. Verbridge, I. W. Frank, D. M. Tanenbaum, J. M. Parpia, H. G. Craighead, P. L. McEuen, Electromechanical resonators from graphene sheets. *Science* **315**, 490-493 (2007).

[16] C. Y. Chen, S. Rosenblatt, K. I. Bolotin, W. Kalb, P. Kim, I. Kymissis, H. L. Stormer, T. F. Heinz, J. Hone, Performance of monolayer graphene nanomechanical resonators with electrical readout. *Nat. Nanotech.* **4**, 861-867 (2009).

[17] J. C. Meyer, A. K. Geim, M. I. Katsnelson, K. S. Novoselov, T. J. Booth, S. Roth, The structure of suspended graphene sheets. *Nature* **446**, 60-63 (2007).

[18] K. Kim, Z. Lee, B. D. Malone, K. T. Chan, B. Aleman, W. Regan, W. Gannett, M. F. Crommie, M. L. Cohen, A. Zettl, Multiply folded graphene. *Phys. Rev. B* **83**, 245433 (2011).

[19] K. S. Kim, Y. Zhao, H. Jang, S. Y. Lee, J. M. Kim, K. S. Kim, J. H. Ahn, P. Kim, J. Y. Choi, B. H. Hong, Large-scale pattern growth of graphene films for stretchable transparent electrodes. *Nature* **457**, 706-710 (2009).

[20] A. A. Balandin, S. Ghosh, W. Z. Bao, I. Calizo, D. Teweldebrhan, F. Miao, C. N. Lau, Superior thermal conductivity of single-layer graphene. *Nano Lett.* **8**, 902-907 (2008).

[21] A. A. Balandin, Thermal properties of graphene and nanostructured carbon materials. *Nat. Mater.* **10**, 569-581 (2011).

[22] S. Ghosh, W. Bao, D. L. Nika, S. Subrina, E. P. Pokatilov, C. N. Lau, A. A. Balandin, Dimensional crossover of thermal transport in few-layer graphene. *Nat. Mater.* **9**, 555-558 (2010).

[23] W. Z. Bao, F. Miao, Z. Chen, H. Zhang, W. Y. Jang, C. Dames, C. N. Lau, Controlled ripple texturing of suspended graphene and ultrathin graphite membranes. *Nat. Nanotech.* **4**, 562-566 (2009).

[24] A. E. Morgan, G. A. Somorjai, Low energy electron diffraction studies of gas adsorption on the platinum (100) single crystal surface. *Surf. Sci.* **12**, 405-424 (1968).

[25] J. W. May, Platinum surface LEED rings. *Surf. Sci.* **17**, 267-270 (1969).

[26] M. Eizenberg, J. M. Blakely, Carbon monolayer phase condensation on Ni(111). *Surf.*

Sci. **82**, 228-236 (1979).

[27] J. C. Shelton, H. R. Patil, J. M. Blakely, Equilibrium segregation of carbon to a nickel (111) surface: A surface phase transition. *Surf. Sci.* **43**, 493-520 (1973).

[28] D. R. Dreyer, R. S. Ruoff, C. W. Bielawski, From Conception to Realization: An Historial Account of Graphene and Some Perspectives for Its Future. *Ang. Chem. Int. Ed.* **49**, 9336-9334 (2010).

[29] Q. Yu, J. Lian, S. Siriponglert, H. Li, Y. P. Chen, S. S. Pei, Graphene segregated on Ni surfaces and transferred to insulators. *Appl. Phys. Lett.* **93**, 113103 (2008).

[30] A. Reina, X. T. Jia, J. Ho, D. Nezich, H. B. Son, V. Bulovic, M. S. Dresselhaus, J. Kong, Large Area, Few-Layer Graphene Films on Arbitrary Substrates by Chemical Vapor Deposition. *Nano Lett.* **9**, 30-35 (2009).

[31] X. S. Li, W. W. Cai, J. H. An, S. Kim, J. Nah, D. X. Yang, R. Piner, A. Velamakanni, I. Jung, E. Tutuc, S. K. Banerjee, L. Colombo, R. S. Ruoff, Large-Area Synthesis of High-Quality and Uniform Graphene Films on Copper Foils. *Science* **324**, 1312-1314 (2009).

[32] S. Bae, H. Kim, Y. Lee, X. F. Xu, J. S. Park, Y. Zheng, J. Balakrishnan, T. Lei, H. R. Kim, Y. I. Song, Y. J. Kim, K. S. Kim, B. Ozyilmaz, J. H. Ahn, B. H. Hong, S. Iijima, Roll-to-roll production of 30-inch graphene films for transparent electrodes. *Nat. Nanotech.* **5**, 574-578 (2010).

[33] Y. Lee, S. Bae, H. Jang, S. Jang, S. E. Zhu, S. H. Sim, Y. I. Song, B. H. Hong, J. H. Ahn, Wafer-Scale Synthesis and Transfer of Graphene Films. *Nano Lett.* **10**, 490-493 (2010).

[34] X. S. Li, W. W. Cai, L. Colombo, R. S. Ruoff, Evolution of Graphene Growth on Ni and Cu by Carbon Isotope Labeling. *Nano Lett.* **9**, 4268-4272 (2009).

[35] Z. Sun, Z. Yan, J. Yao, E. Beitler, Y. Zhu, J. M. Tour, Growth of graphene from solid carbon sources. *Nature* **468**, 549-552 (2010).

[36] P. W. Sutter, J. I. Flege, E. A. Sutter, Epitaxial graphene on ruthenium. *Nat. Mater.* **7**, 406-411 (2008).

[37] T. A. Land, T. Michely, R. J. Behm, J. C. Hemminger, G. Comsa, STM investigation of single layer graphite structures produced on Pt(111) by hydrocarbon decomposition. *Surf. Sci.* **264**, 261-270 (1992).

[38] E. Loginova, S. Nie, K. Thurmer, N. C. Bartelt, K. F. McCarty, Defects of graphene on Ir(111): Rotational domains and ridges. *Phys. Rev. B* **80**, 085430 (2009).

[39] A. J. Van Bommel, J. E. Crombeen, A. Van Tooren, LEED and Auger electron observations of the SiC(0001) surface. *Surf. Sci.* **48**, 463-472 (1975).

[40] C. Berger, Z. M. Song, T. B. Li, X. B. Li, A. Y. Ogbazghi, R. Feng, Z. T. Dai, A. N. Marchenkov, E. H. Conrad, P. N. First, W. A. de Heer, Ultrathin epitaxial graphite: 2D electron gas properties and a route toward graphene-based nanoelectronics. *J. Phys. Chem. B* **108**, 19912-19916 (2004).

[41] W. S. Hummers, R. E. Offeman, Preparation of Graphitic Oxide. *J. Am. Chem. Soc.* **80**, 1339 (1958).

[42] K. Erickson, R. Erni, Z. Lee, N. Alem, W. Gannett, A. Zettl, Determination of the Local Chemical Structure of Graphene Oxide and Reduced Graphene Oxide. *Adv. Mater.* **22**, 4467-4472 (2010).

[43] M. Ishigami, J. H. Chen, W. G. Cullen, M. S. Fuhrer, E. D. Williams, Atomic Structure of Graphene on SiO_2. *Nano Lett.* **7**, 1643-1648 (2007).

[44] W. Regan, N. Alem, B. Aleman, B. S. Geng, C. Girit, L. Maserati, F. Wang, M. Crommie, A. Zettl, A direct transfer of layer-area graphene. *Appl. Phys. Lett.* **96**, 113102 (2010).

[45] J. M. Yuk, K. Kim, B. Aleman, W. Regan, J. H. Ryu, J. Park, P. Ercius, H. M. Lee, A. P. Alivisatos, M. F. Crommie, J. Y. Lee, A. Zettl, Graphene Veils and Sandwiches. *Nano Lett.* **11**, 3290-3294 (2011).

[46] K. Kim, S. Coh, L. Z. Tan, W. Regan, J. M. Yuk, E. Chatterjee, M. F. Crommie, M. L. Cohen, S. G. Louie, A. Zettl, Raman Spectroscopy Study of Rotated Double-Layer Graphene: Misorientation-Angle Dependence of Electronic Structure. *Phys. Rev. Lett.* **108**, 246103 (2012).

[47] J. M. Yuk, J. Park, P. Ercius, K. Kim, D. J. Hellebusch, M. F. Crommie, J. Y. Lee, A. Zettl, A. P. Alivisatos, High-Resolution EM of Colloidal Nanocrystal Growth Using Graphene Liquid Cells. *Science* **336**, 61-64 (2012).

[48] D. B. Williams, C. B. Carter, *Transmission Electron Microscopy*. (Plenum Press, New York, 1996).

[49] B. Fultz, J. M. Howe, *Transmission Electron Microscopy and Diffractometry of Materials*. (Springer, Berlin, New York, ed. 3rd, 2008).

[50] M. Haider, S. Uhlemann, E. Schwan, H. Rose, B. Kabius, K. Urban, Electron microscopy image enhanced. *Nature* **392**, 768-769 (1998).

[51] D. J. Smith, Development of Aberration-Corrected Electron Microscopy. *Micro.*

Microanal. **14**, 2-15 (2008).

[52] P. Hartel, H. Rose, C. Dinges, Conditions and reasons for incoherent imaging in STEM. *Ultramicroscopy* **63**, 93-114 (1996).

[53] O. Scherzer, The Theoretical Resolution Limit of the Electron Microscope *J. Appl. Phys.* **20**, 20-29 (1949).

[54] R. Erni, *Aberration-Corrected Imaging in Transmission Electron Microscopy: An Introduction*. (Imperial College Press, London, 2010).

[55] M. Lentzen, Contrast Transfer and Resolution Limits for Sub-Angstrom High-Resolution Transmission Electron Microscopy. *Micro. Microanal.* **14**, 16-26 (2008).

[56] F. Zemlin, K. Weiss, P. Schiske, W. Kunath, K.-H. Herrmann, Coma-free alignment of high resolution electron microscopes with the aid of optical diffractograms. *Ultramicroscopy* **3**, 49-60 (1978).

[57] C. Kittel, *Introduction to Solid State Physics*. (Wiley, ed. 8th, 2005).

[58] J. C. Meyer, A. K. Geim, M. I. Katsnelson, K. S. Novoselov, D. Obergfell, S. Roth, C. Girit, A. Zettl, On the roughness of single- and bi-layer graphene membranes. *Solid State Commun.* **143**, 101-109 (2007).

[59] W. W. Cai, A. L. Moore, Y. W. Zhu, X. S. Li, S. S. Chen, L. Shi, R. S. Ruoff, Thermal Transport in Suspended and Supported Monolayer Graphene Grown by Chemical Vapor Deposition. *Nano Lett.* **10**, 1645-1651 (2010).

[60] R. Grantab, V. B. Shenoy, R. S. Ruoff, Anomalous Strength Characteristics of Tilt Grain Boundaries in Graphene. *Science* **330**, 946-948 (2010).

[61] O. V. Yazyev, S. G. Louie, Electronic transport in polycrystalline graphene. *Nat. Mater.* **9**, 806-809 (2010).

[62] T. R. Albrecht, H. A. Mizes, J. Nogami, S. I. Park, C. F. Quate, Observation of Tilt Boundaries in Graphite by Scanning Tunneling Microscopy and Associated Multiple Tip Effects. *Appl. Phys. Lett.* **52**, 362-364 (1988).

[63] P. Simonis, C. Goffaux, P. A. Thiry, L. P. Biro, P. Lambin, V. Meunier, STM study of a grain boundary in graphite. *Surf. Sci.* **511**, 319-322 (2002).

[64] W. T. Pong, J. Bendall, C. Durkan, Observation and investigation of graphite superlattice boundaries by scanning tunneling microscopy. *Surf. Sci.* **601**, 498-509 (2007).

[65] J. Cervenka, C. F. J. Flipse, Structural and electronic properties of grain boundaries in graphite: Planes of periodically distributed point defects. *Phys. Rev. B* **79**, 195429 (2009).

[66] J. Coraux, A. T. N'Diaye, C. Busse, T. Michely, Structural coherency of graphene on Ir(111). *Nano Lett.* **8**, 565-570 (2008).

[67] F. Varchon, P. Mallet, L. Magaud, J. Y. Veuillen, Rotational disorder in few-layer graphene films on 6H-SiC(000-1): A scanning tunneling microscopy study. *Phys. Rev. B* **77**, 165415 (2008).

[68] J. Lahiri, Y. Lin, P. Bozkurt, Oleynik, II, M. Batzill, An extended defect in graphene as a metallic wire. *Nat. Nanotech.* **5**, 326-329 (2010).

[69] L. Gao, J. R. Guest, N. P. Guisinger, Epitaxial Graphene on Cu(111). *Nano Lett.* **10**, 3512-3516 (2010).

[70] J. C. Meyer, C. O. Girit, M. F. Crommie, A. Zettl, Imaging and dynamics of light atoms and molecules on graphene. *Nature* **454**, 319-322 (2008).

[71] A. Hashimoto, K. Suenaga, A. Gloter, K. Urita, S. Iijima, Direct evidence for atomic defects in graphene layers. *Nature* **430**, 870-873 (2004).

[72] K. Suenaga, H. Wakabayashi, M. Koshino, Y. Sato, K. Urita, S. Iijima, Imaging active topological defects in carbon nanotubes. *Nat. Nanotech.* **2**, 358-360 (2007).

[73] J. C. Meyer, C. Kisielowski, R. Erni, M. D. Rossell, M. F. Crommie, A. Zettl, Direct Imaging of Lattice Atoms and Topological Defects in Graphene Membranes. *Nano Lett.* **8**, 3582-3586 (2008).

[74] A. Sinitskii, V. Abramova, T. Laptinskaya, Y. D. Tretyakov, Domain mapping of inverse photonic crystals by laser diffraction. *Phys. Lett. A* **366**, 516-522 (2007).

[75] H. J. Park, J. Meyer, S. Roth, V. Skakalova, Growth and properties of few-layer graphene prepared by chemical vapor deposition. *Carbon* **48**, 1088-1094 (2010).

[76] O. V. Yazyev, S. G. Louie, Topological defects in graphene: Dislocations and grain boundaries. *Phys. Rev. B* **81**, 195420 (2010).

[77] Y. Y. Liu, B. I. Yakobson, Cones, Pringles, and Grain Boundary Landscapes in Graphene Topology. *Nano Lett.* **10**, 2178-2183 (2010).

[78] J. U. Bowie, Solving the membrane protein folding problem. *Nature* **438**, 581-589 (2005).

[79] P. W. K. Rothemund, Folding DNA to create nanoscale shapes and patterns. *Nature* **440**, 297-302 (2006).

[80] E. Hawkes, B. An, N. M. Benbernou, H. Tanaka, S. Kim, E. D. Demaine, D. Rus, R. J. Wood, Programmable matter by folding. *Proc. Natl. Acad. Sci. U.S.A.* **107**, 12441-12445 (2010).

[81] L. X. Benedict, N. G. Chopra, M. L. Cohen, A. Zettl, S. G. Louie, V. H. Crespi, Microscopic determination of the interlayer binding energy in graphite. *Chem. Phys. Lett.* **286**, 490-496 (1998).

[82] E. Prada, P. San-Jose, L. Brey, Zero Landau Level in Folded Graphene Nanoribbons. *Phys. Rev. Lett.* **105**, 106802 (2010).

[83] D. Rainis, F. Taddei, M. Polini, G. Leon, F. Guinea, V. I. Fal'ko, Gauge fields and interferometry in folded graphene. *Phys. Rev. B* **83**, 165403 (2011).

[84] H. Hiura, T. W. Ebbesen, J. Fujita, K. Tanigaki, T. Takada, Role of Sp(3) Defect Structures in Graphite and Carbon Nanotubes. *Nature* **367**, 148-151 (1994).

[85] H. V. Roy, C. Kallinger, K. Sattler, Study of single and multiple foldings of graphitic sheets. *Surf. Sci.* **407**, 1-6 (1998).

[86] J. H. Warner, M. H. Rummeli, T. Gemming, B. Buchner, G. A. D. Briggs, Direct Imaging of Rotational Stacking Faults in Few Layer Graphene. *Nano Lett.* **9**, 102-106 (2009).

[87] J. Y. Huang, F. Ding, B. I. Yakobson, P. Lu, L. Qi, J. Li, In situ observation of graphene sublimation and multi-layer edge reconstructions. *Proc. Natl. Acad. Sci. U.S.A.* **106**, 10103-10108 (2009).

[88] Z. Liu, K. Suenaga, P. J. F. Harris, S. Iijima, Open and Closed Edges of Graphene Layers. *Phys. Rev. Lett.* **102**, 015501 (2009).

[89] J. Zhang, J. L. Xiao, X. H. Meng, C. Monroe, Y. G. Huang, J. M. Zuo, Free Folding of Suspended Graphene Sheets by Random Mechanical Stimulation. *Phys. Rev. Lett.* **104**, 166805 (2010).

[90] C. Wolff, *The Art of Manipulating Fabric*. (Krause Publications, Iola, WI, 1996).

[91] M. S. Dresselhaus, G. Dresselhaus, Intercalation Compounds of Graphite. *Adv. Phys.* **30**, 139-326 (1981).

[92] S. Park, D. Srivastava, K. Cho, Generalized chemical reactivity of curved surfaces: Carbon nanotubes. *Nano Lett.* **3**, 1273-1277 (2003).

[93] S. Iijima, Helical Microtubules of Graphitic Carbon. *Nature* **354**, 56-58 (1991).

[94] K. Kim, Z. Lee, W. Regan, C. Kisielowski, M. F. Crommie, A. Zettl, Grain Boundary Mapping in Polycrystalline Graphene. *ACS Nano* **5**, 2142-2146 (2011).

[95] M. P. do Carmo, *Differential Geometry of Curves and Surfaces*. (Prentice-Hall, Englewood Cliffs, New Jersey, 1976).

[96] J. M. Soler, E. Artacho, J. D. Gale, A. Garcia, J. Junquera, P. Ordejon, D. Sanchez-Portal, The SIESTA method for ab initio order-N materials simulation. *J. Phys.: Condens. Matter* **14**, 2745-2779 (2002).

[97] N. Troullier, J. L. Martins, Efficient Pseudopotentials for Plane-Wave Calculations. *Phys. Rev. B* **43**, 1993-2006 (1991).

[98] D. M. Ceperley, B. J. Alder, Ground-State of the Electron-Gas by a Stochastic Method. *Phys. Rev. Lett.* **45**, 566-569 (1980).

[99] J. P. Perdew, A. Zunger, Self-Interaction Correction to Density-Functional Approximations for Many-Electron Systems. *Phys. Rev. B* **23**, 5048-5079 (1981).

[100] S. Latil, L. Henrard, Charge carriers in few-layer graphene films. *Phys. Rev. Lett.* **97**, 036803 (2006).

[101] K. F. Mak, M. Y. Sfeir, J. A. Misewich, T. F. Heinz, The evolution of electronic structure in few-layer graphene revealed by optical spectroscopy. *Proc. Natl. Acad. Sci. U.S.A.* **107**, 14999-15004 (2010).

[102] T. Ohta, A. Bostwick, T. Seyller, K. Horn, E. Rotenberg, Controlling the electronic structure of bilayer graphene. *Science* **313**, 951-954 (2006).

[103] E. V. Castro, K. S. Novoselov, S. V. Morozov, N. M. R. Peres, J. Dos Santos, J. Nilsson, F. Guinea, A. K. Geim, A. H. C. Neto, Biased bilayer graphene: Semiconductor with a gap tunable by the electric field effect. *Phys. Rev. Lett.* **99**, 216802 (2007).

[104] Y. B. Zhang, T. T. Tang, C. Girit, Z. Hao, M. C. Martin, A. Zettl, M. F. Crommie, Y. R. Shen, F. Wang, Direct observation of a widely tunable bandgap in bilayer graphene. *Nature* **459**, 820-823 (2009).

[105] M. F. Craciun, S. Russo, M. Yamamoto, J. B. Oostinga, A. F. Morpurgo, S. Tarucha, Trilayer graphene is a semimetal with a gate-tunable band overlap. *Nat. Nanotech.* **4**, 383-388 (2009).

[106] G. H. Li, A. Luican, J. dos Santos, A. H. C. Neto, A. Reina, J. Kong, E. Y. Andrei,

Observation of Van Hove singularities in twisted graphene layers. *Nat. Phys.* **6**, 109-113 (2010).

[107] J. M. B. Lopes dos Santos, N. M. R. Peres, A. H. Castro, Graphene bilayer with a twist: Electronic structure. *Phys. Rev. Lett.* **99**, 256802 (2007).

[108] G. T. de Laissardiere, D. Mayou, L. Magaud, Localization of Dirac Electrons in Rotated Graphene Bilayers. *Nano Lett.* **10**, 804-808 (2010).

[109] P. E. Lammert, P. H. Zhang, V. H. Crespi, Gapping by squashing: Metal-insulator and insulator-metal transitions in collapsed carbon nanotubes. *Phys. Rev. Lett.* **84**, 2453-2456 (2000).

[110] J. Feng, L. Qi, J. Y. Huang, J. Li, Geometric and electronic structure of graphene bilayer edges. *Phys. Rev. B* **80**, 165407 (2009).

[111] Y. Takagi, S. Okada, Asymmetrical Electronic Structure of Folded Graphene. *J. Phys. Soc. Jpn.* **79**, 033702 (2010).

[112] M. L. Cohen, M. Schluter, J. R. Chelikowsky, S. G. Louie, Self-Consistent Pseudopotential Method for Localized Configurations - Molecules. *Phys. Rev. B* **12**, 5575-5579 (1975).

[113] N. G. Chopra, L. X. Benedict, V. H. Crespi, M. L. Cohen, S. G. Louie, A. Zettl, Fully Collapsed Carbon Nanotubes. *Nature* **377**, 135-138 (1995).

[114] A. T. N'Diaye, R. van Gastel, A. J. Martinez-Galera, J. Coraux, H. Hattab, D. Wall, F. J. M. zu Heringdorf, M. Horn-von Hoegen, J. M. Gomez-Rodriguez, B. Poelsema, C. Busse, T. Michely, In situ observation of stress relaxation in epitaxial graphene. *New J. Phys.* **11**, 113056 (2009).

[115] S. J. Chae, F. Gunes, K. K. Kim, E. S. Kim, G. H. Han, S. M. Kim, H. J. Shin, S. M. Yoon, J. Y. Choi, M. H. Park, C. W. Yang, D. Pribat, Y. H. Lee, Synthesis of Large-Area Graphene Layers on Poly-Nickel Substrate by Chemical Vapor Deposition: Wrinkle Formation. *Adv. Mater.* **21**, 2328-2333 (2009).

[116] V. Gupta, P. Scharff, K. Risch, H. Romanus, R. Muller, Synthesis of C-60 intercalated graphite. *Solid State Commun.* **131**, 153-155 (2004).

[117] M. Monthioux, Filling single-wall carbon nanotubes. *Carbon* **40**, 1809-1823 (2002).

[118] D. J. Hornbaker, S. J. Kahng, S. Misra, B. W. Smith, A. T. Johnson, E. J. Mele, D. E. Luzzi, A. Yazdani, Mapping the one-dimensional electronic states of nanotube peapod structures. *Science* **295**, 828-831 (2002).

[119] W. Mickelson, S. Aloni, W. Q. Han, J. Cumings, A. Zettl, Packing C-60 in boron nitride nanotubes. *Science* **300**, 467-469 (2003).

[120] J. Ihm, A. Zunger, M. L. Cohen, Momentum-Space Formalism for the Total Energy of Solids. *J. Phys. C* **12**, 4409-4422 (1979).

[121] P. Giannozzi, S. Baroni, N. Bonini, M. Calandra, R. Car, C. Cavazzoni, D. Ceresoli, G. L. Chiarotti, M. Cococcioni, I. Dabo, A. Dal Corso, S. de Gironcoli, S. Fabris, G. Fratesi, R. Gebauer, U. Gerstmann, C. Gougoussis, A. Kokalj, M. Lazzeri, L. Martin-Samos, N. Marzari, F. Mauri, R. Mazzarello, S. Paolini, A. Pasquarello, L. Paulatto, C. Sbraccia, S. Scandolo, G. Sclauzero, A. P. Seitsonen, A. Smogunov, P. Umari, R. M. Wentzcovitch, QUANTUM ESPRESSO: a modular and open-source software project for quantum simulations of materials. *J. Phys.: Condens. Matter* **21**, 395502 (2009).

[122] M. Aoki, H. Amawashi, Dependence of band structures on stacking and field in layered graphene. *Solid State Commun.* **142**, 123-127 (2007).

[123] Y. K. Kwon, D. Tomanek, Electronic and structural properties of multiwall carbon nanotubes. *Phys. Rev. B* **58**, 16001-16004 (1998).

[124] F. Liu, P. M. Ming, J. Li, Ab initio calculation of ideal strength and phonon instability of graphene under tension. *Phys. Rev. B* **76**, 064120 (2007).

[125] A. Omeltchenko, J. Yu, R. K. Kalia, P. Vashishta, Crack front propagation and fracture in a graphite sheet: A molecular-dynamics study on parallel computers. *Phys. Rev. Lett.* **78**, 2148-2151 (1997).

[126] H. Zhao, K. Min, N. R. Aluru, Size and Chirality Dependent Elastic Properties of Graphene Nanoribbons under Uniaxial Tension. *Nano Lett.* **9**, 3012-3015 (2009).

[127] Z. P. Xu, Graphene Nano-Ribbons Under Tension. *J. Comput. Theor. Nanosci.* **6**, 625-628 (2009).

[128] S. S. Terdalkar, S. Huang, H. Y. Yuan, J. J. Rencis, T. Zhu, S. L. Zhang, Nanoscale fracture in graphene. *Chem. Phys. Lett.* **494**, 218-222 (2010).

[129] C. S. Ruiz-Vargas, H. L. L. Zhuang, P. Y. Huang, A. M. van der Zande, S. Garg, P. L. McEuen, D. A. Muller, R. G. Hennig, J. Park, Softened Elastic Response and Unzipping in Chemical Vapor Deposition Graphene Membranes. *Nano Lett.* **11**, 2259-2263 (2011).

[130] D. Sen, K. S. Novoselov, P. M. Reis, M. J. Buehler, Tearing Graphene Sheets From Adhesive Substrates Produces Tapered Nanoribbons. *Small* **6**, 1108-1116 (2010).

[131] J. Kotakoski, A. V. Krasheninnikov, U. Kaiser, J. C. Meyer, From Point Defects in

Graphene to Two-Dimensional Amorphous Carbon. *Phys. Rev. Lett.* **106**, 105505 (2011).

[132] F. Banhart, Irradiation effects in carbon nanostructures. *Rep. Prog. Phys.* **62**, 1181-1221 (1999).

[133] R. F. Egerton, P. Li, M. Malac, Radiation damage in the TEM and SEM. *Micron* **35**, 399-409 (2004).

[134] B. W. Smith, D. E. Luzzi, Electron irradiation effects in single wall carbon nanotubes. *J. Appl. Phys.* **90**, 3509-3515 (2001).

[135] A. Zobelli, A. Gloter, C. P. Ewels, C. Colliex, Shaping single walled nanotubes with an electron beam. *Phys. Rev. B* **77**, 045410 (2008).

[136] P. Koskinen, S. Malola, H. Häkkinen, Self-Passivating Edge Reconstructions of Graphene. *Phys. Rev. Lett.* **101**, 115502 (2008).

[137] A. Chuvilin, J. C. Meyer, G. Algara-Siller, U. Kaiser, From graphene constrictions to single carbon chains. *New J. Phys.* **11**, 083019 (2009).

[138] A. A. Griffith, The phenomena of rupture and flow in solids. *Philos. Trans. R. Soc. London, Ser. A* **221**, 163-198 (1920).

[139] Y. Y. Liu, A. Dobrinsky, B. I. Yakobson, Graphene Edge from Armchair to Zigzag: The Origins of Nanotube Chirality? *Phys. Rev. Lett.* **105**, 235502 (2010).

[140] A. C. T. van Duin, S. Dasgupta, F. Lorant, W. A. Goddard, ReaxFF: A reactive force field for hydrocarbons. *J. Phys. Chem. A* **105**, 9396-9409 (2001).

[141] J. E. Mueller, A. C. T. van Duin, W. A. Goddard, Development and Validation of ReaxFF Reactive Force Field for Hydrocarbon Chemistry Catalyzed by Nickel. *J. Phys. Chem. C* **114**, 4939-4949 (2010).

[142] P. Y. Huang, C. S. Ruiz-Vargas, A. M. van der Zande, W. S. Whitney, M. P. Levendorf, J. W. Kevek, S. Garg, J. S. Alden, C. J. Hustedt, Y. Zhu, J. Park, P. L. McEuen, D. A. Muller, Grains and grain boundaries in single-layer graphene atomic patchwork quilts. *Nature* **469**, 389-392 (2011).

[143] T. Dumitrica, M. Hua, B. I. Yakobson, Symmetry-, time-, and temperature-dependent strength of carbon nanotubes. *Proc. Natl. Acad. Sci. U.S.A.* **103**, 6105-6109 (2006).

[144] B. I. Yakobson, F. Ding, Observational Geology of Graphene, at the Nanoscale. *ACS Nano* **5**, 1569-1574 (2011).

[145] K. A. Ritter, J. W. Lyding, The influence of edge structure on the electronic properties of graphene quantum dots and nanoribbons. *Nat. Mater.* **8**, 235-242 (2009).

[146] J. Abrahams, Graphite Sublimation Temperatures, Carbon Arcs and Crystalline Erosion. *Carbon* **12**, 111-118 (1974).

[147] G. E. Begtrup, K. G. Ray, B. M. Kessler, T. D. Yuzvinsky, H. Garcia, A. Zettl, Probing nanoscale solids at thermal extremes. *Phys. Rev. Lett.* **99**, 155901 (2007).

[148] J. Y. Huang, L. Qi, J. Li, In situ imaging of layer-by-layer sublimation of suspended graphene. *Nano Res.* **3**, 43-50 (2010).

[149] X. T. Jia, M. Hofmann, V. Meunier, B. G. Sumpter, J. Campos-Delgado, J. M. Romo-Herrera, H. B. Son, Y. P. Hsieh, A. Reina, J. Kong, M. Terrones, M. S. Dresselhaus, Controlled Formation of Sharp Zigzag and Armchair Edges in Graphitic Nanoribbons. *Science* **323**, 1701-1705 (2009).

[150] C. Jin, K. Suenaga, S. Iijima, Plumbing carbon nanotubes. *Nat. Nanotech.* **3**, 17-21 (2008).

[151] T. Kamino, H. Saka, A Newly Developed High-Resolution Hot Stage and Its Application to Materials Characterization. *Microsc. Microanal. Microstruct.* **4**, 127-135 (1993).

[152] S. Shallcross, S. Sharma, O. A. Pankratov, Quantum interference at the twist boundary in graphene. *Phys. Rev. Lett.* **101**, 056803 (2008).

[153] E. J. Mele, Commensuration and interlayer coherence in twisted bilayer graphene. *Phys. Rev. B* **81**, 161405 (2010).

[154] R. Bistritzer, A. H. MacDonald, Moire bands in twisted double-layer graphene. *Proc. Natl. Acad. Sci. U.S.A.* **108**, 12233-12237 (2011).

[155] H. Schmidt, T. Ludtke, P. Barthold, E. McCann, V. I. Fal'ko, R. J. Haug, Tunable graphene system with two decoupled monolayers. *Appl. Phys. Lett.* **93**, 172108 (2008).

[156] J. Hicks, M. Sprinkle, K. Shepperd, F. Wang, A. Tejeda, A. Taleb-Ibrahimi, F. Bertran, P. Le Fevre, W. A. de Heer, C. Berger, E. H. Conrad, Symmetry breaking in commensurate graphene rotational stacking: Comparison of theory and experiment. *Phys. Rev. B* **83**, 205403 (2011).

[157] A. Luican, G. H. Li, A. Reina, J. Kong, R. R. Nair, K. S. Novoselov, A. K. Geim, E. Y. Andrei, Single-Layer Behavior and Its Breakdown in Twisted Graphene Layers. *Phys. Rev. Lett.* **106**, 126802 (2011).

[158] J. Hass, F. Varchon, J. E. Millan-Otoya, M. Sprinkle, N. Sharma, W. A. De Heer, C. Berger, P. N. First, L. Magaud, E. H. Conrad, Why multilayer graphene on 4H-SiC(000(1)over-bar) behaves like a single sheet of graphene. *Phys. Rev. Lett.* **100**, 125504 (2008).

[159] Y. Y. Wang, Z. H. Ni, L. Liu, Y. H. Liu, C. X. Cong, T. Yu, X. J. Wang, D. Z. Shen, Z. X. Shen, Stacking-Dependent Optical Conductivity of Bilayer Graphene. *ACS Nano* **4**, 4074-4080 (2010).

[160] C. Berger, Z. M. Song, X. B. Li, X. S. Wu, N. Brown, C. Naud, D. Mayou, T. B. Li, J. Hass, A. N. Marchenkov, E. H. Conrad, P. N. First, W. A. de Heer, Electronic confinement and coherence in patterned epitaxial graphene. *Science* **312**, 1191-1196 (2006).

[161] A. Jorio, R. Saito, G. Dresselhaus, M. S. Dresselhaus, *Raman Spectroscopy in Graphene Related Systems*. (Wiley-VCH, Weinheim, 2011).

[162] M. S. Dresselhaus, A. Jorio, M. Hofmann, G. Dresselhaus, R. Saito, Perspectives on Carbon Nanotubes and Graphene Raman Spectroscopy. *Nano Lett.* **10**, 751-758 (2010).

[163] A. C. Ferrari, J. C. Meyer, V. Scardaci, C. Casiraghi, M. Lazzeri, F. Mauri, S. Piscanec, D. Jiang, K. S. Novoselov, S. Roth, A. K. Geim, Raman spectrum of graphene and graphene layers. *Phys. Rev. Lett.* **97**, 187401 (2006).

[164] A. Gupta, G. Chen, P. Joshi, S. Tadigadapa, P. C. Eklund, Raman scattering from high-frequency phonons in supported n-graphene layer films. *Nano Lett.* **6**, 2667-2673 (2006).

[165] Z. H. Ni, Y. Y. Wang, T. Yu, Y. M. You, Z. X. Shen, Reduction of Fermi velocity in folded graphene observed by resonance Raman spectroscopy. *Phys. Rev. B* **77**, 235403 (2008).

[166] P. Poncharal, A. Ayari, T. Michel, J. L. Sauvajol, Raman spectra of misoriented bilayer graphene. *Phys. Rev. B* **78**, 113407 (2008).

[167] Z. H. Ni, L. Liu, Y. Y. Wang, Z. Zheng, L. J. Li, T. Yu, Z. X. Shen, G-band Raman double resonance in twisted bilayer graphene: Evidence of band splitting and folding. *Phys. Rev. B* **80**, 125404 (2009).

[168] A. K. Gupta, Y. J. Tang, V. H. Crespi, P. C. Eklund, Nondispersive Raman D band activated by well-ordered interlayer interactions in rotationally stacked bilayer graphene. *Phys. Rev. B* **82**, 241406 (2010).

[169] V. Carozo, C. M. Almeida, E. H. M. Ferreira, L. G. Cancado, C. A. Achete, A. Jorio, Raman Signature of Graphene Superlattices. *Nano Lett.* **11**, 4527-4534 (2011).

[170] A. Righi, S. D. Costa, H. Chacham, C. Fantini, P. Venezuela, C. Magnuson, L. Colombo, W. S. Bacsa, R. S. Ruoff, M. A. Pimenta, Graphene Moire patterns observed by umklapp double-resonance Raman scattering. *Phys. Rev. B* **84**, 241409 (2011).

[171] A. Gruneis, C. Attaccalite, L. Wirtz, H. Shiozawa, R. Saito, T. Pichler, A. Rubio, Tight-binding description of the quasiparticle dispersion of graphite and few-layer graphene. *Phys. Rev. B* **78**, 205425 (2008).

[172] P. E. Trevisanutto, C. Giorgetti, L. Reining, M. Ladisa, V. Olevano, Ab Initio GW Many-Body Effects in Graphene. *Phys. Rev. Lett.* **101**, 226405 (2008).

[173] L. Yang, J. Deslippe, C. H. Park, M. L. Cohen, S. G. Louie, Excitonic Effects on the Optical Response of Graphene and Bilayer Graphene. *Phys. Rev. Lett.* **103**, 186802 (2009).

[174] M. Y. Han, B. Ozyilmaz, Y. B. Zhang, P. Kim, Energy band-gap engineering of graphene nanoribbons. *Phys. Rev. Lett.* **98**, 206805 (2007).

[175] Z. Chen, Y.-M. Lin, M. J. Rooks, P. Avouris, Graphene nano-ribbon electronics. *Physica E* **40**, 228-232 (2007).

[176] X. L. Li, X. R. Wang, L. Zhang, S. W. Lee, H. J. Dai, Chemically derived, ultrasmooth graphene nanoribbon semiconductors. *Science* **319**, 1229-1232 (2008).

[177] Y. W. Son, M. L. Cohen, S. G. Louie, Half-metallic graphene nanoribbons. *Nature* **444**, 347-349 (2006).

[178] Y. W. Son, M. L. Cohen, S. G. Louie, Energy gaps in graphene nanoribbons. *Phys. Rev. Lett.* **97**, 216803 (2006).

[179] D. V. Kosynkin, A. L. Higginbotham, A. Sinitskii, J. R. Lomeda, A. Dimiev, B. K. Price, J. M. Tour, Longitudinal unzipping of carbon nanotubes to form graphene nanoribbons. *Nature* **458**, 872-876 (2009).

[180] L. Y. Jiao, L. Zhang, X. R. Wang, G. Diankov, H. J. Dai, Narrow graphene nanoribbons from carbon nanotubes. *Nature* **458**, 877-880 (2009).

[181] Z. X. Zhang, Z. Z. Sun, J. Yao, D. V. Kosynkin, J. M. Tour, Transforming Carbon Nanotube Devices into Nanoribbon Devices. *J. Am. Chem. Soc.* **131**, 13460-13463 (2009).

[182] A. G. Cano-Marquez, F. J. Rodriguez-Macias, J. Campos-Delgado, C. G. Espinosa-Gonzalez, F. Tristan-Lopez, D. Ramirez-Gonzalez, D. A. Cullen, D. J. Smith, M. Terrones, Y. I. Vega-Cantu, Ex-MWNTs: Graphene Sheets and Ribbons Produced by Lithium Intercalation and Exfoliation of Carbon Nanotubes. *Nano Lett.* **9**, 1527-1533

(2009).

[183] A. L. Elias, A. R. Botello-Mendez, D. Meneses-Rodriguez, V. J. Gonzalez, D. Ramirez-Gonzalez, L. Ci, E. Munoz-Sandoval, P. M. Ajayan, H. Terrones, M. Terrones, Longitudinal Cutting of Pure and Doped Carbon Nanotubes to Form Graphitic Nanoribbons Using Metal Clusters as Nanoscalpels. *Nano Lett.* **10**, 366-372 (2010).

[184] A. Sinitskii, A. A. Fursina, D. V. Kosynkin, A. L. Higginbotham, D. Natelson, J. M. Tour, Electronic transport in monolayer graphene nanoribbons produced by chemical unzipping of carbon nanotubes. *Appl. Phys. Lett.* **95**, 253108 (2009).

[185] P. G. Collins, M. Hersam, M. Arnold, R. Martel, P. Avouris, Current saturation and electrical breakdown in multiwalled carbon nanotubes. *Phys. Rev. Lett.* **86**, 3128-3131 (2001).

[186] P. C. Collins, M. S. Arnold, P. Avouris, Engineering carbon nanotubes and nanotube circuits using electrical breakdown. *Science* **292**, 706-709 (2001).

[187] J. Y. Huang, S. Chen, Z. Q. Wang, K. Kempa, Y. M. Wang, S. H. Jo, G. Chen, M. S. Dresselhaus, Z. F. Ren, Superplastic carbon nanotubes - Conditions have been discovered that allow extensive deformation of rigid single-walled nanotubes. *Nature* **439**, 281-281 (2006).

[188] J. Y. Huang, S. Chen, Z. F. Ren, Z. Wang, K. Kempa, M. J. Naughton, G. Chen, M. S. Dresselhaus, Enhanced ductile behavior of tensile-elongated individual double-walled and triple-walled carbon nanotubes at high temperatures. *Phys. Rev. Lett.* **98**, 185501 (2007).

[189] J. Y. Huang, S. Chen, S. H. Jo, Z. Wang, D. X. Han, G. Chen, M. S. Dresselhaus, Z. F. Ren, Atomic-scale imaging of wall-by-wall breakdown and concurrent transport measurements in multiwall carbon nanotubes. *Phys. Rev. Lett.* **94**, 236802 (2005).

[190] T. D. Yuzvinsky, W. Mickelson, S. Aloni, S. L. Konsek, A. M. Fennimore, G. E. Begtrup, A. Kis, B. C. Regan, A. Zettl, Imaging the life story of nanotube devices. *Appl. Phys. Lett.* **87**, 083103 (2005).

[191] W. S. Kim, S. Y. Moon, S. Y. Bang, B. G. Choi, H. Ham, T. Sekino, K. B. Shim, Fabrication of graphene layers from multiwalled carbon nanotubes using high dc pulse. *Appl. Phys. Lett.* **95**, 083103 (2009).

[192] C. O. Girit, A. Zettl, Soldering to a single atomic layer. *Appl. Phys. Lett.* **91**, 193512 (2007).

[193] J. Moser, A. Barreiro, A. Bachtold, Current-induced cleaning of graphene. *Appl. Phys. Lett.* **91**, 163513 (2007).

[194] J. Campos-Delgado, J. M. Romo-Herrera, X. T. Jia, D. A. Cullen, H. Muramatsu, Y. A. Kim, T. Hayashi, Z. F. Ren, D. J. Smith, Y. Okuno, T. Ohba, H. Kanoh, K. Kaneko, M. Endo, H. Terrones, M. S. Dresselhaus, M. Terrones, Bulk production of a new form of sp^2 carbon: Crystalline graphene nanoribbons. *Nano Lett.* **8**, 2773-2778 (2008).

[195] T. D. Yuzvinsky, W. Mickelson, S. Aloni, G. E. Begtrup, A. Kis, A. Zettl, Shrinking a carbon nanotube. *Nano Lett.* **6**, 2718-2722 (2006).